Experimental determination of the transfer function of the zero-power reactor CROCUS with reactivity modulation

Yifeng Jiang

THÈSE

Pour obtenir le grade de

DOCTEUR DE L'UNIVERSITÉ GRENOBLE ALPES

École doctorale : I-MEP2 - Ingénierie - Matériaux, Mécanique, Environnement, Energétique, Procédés, Production
Spécialité : MEP : Mécanique des fluides Energétique, Procédés
Unité de recherche : CEA Cadarache

Détermination expérimentale de la fonction de transfert du réacteur à puissance nulle CROCUS par modulation de réactivité

Experimental determination of the transfer function of the zero-power reactor CROCUS with reactivity modulation

Présentée par :

Yifeng JIANG

Direction de thèse :

Pierre LECONTE Ingénieur HDR, Université Grenoble Alpes	Directeur de thèse
Benoit GESLOT Commissariat à lénergie atomique et aux énergies alternatives	Co-encadrant de thèse
Vincent LAMIRAND Institut Paul Scherrer	Co-encadrant de thèse

Rapporteurs :

Jean-Luc LECOUEY
MAITRE DE CONFERENCES HDR, ENSI Caen
Paolo VINAI
PROFESSEUR ASSOCIE, Chalmers University of Technology

Thèse soutenue publiquement le **21 octobre 2022**, devant le jury composé de :

Pierre LECONTE DIRECTEUR DE RECHERCHE, CEA centre de Cadarache	Directeur de thèse
Elsa MERLE PROFESSEUR DES UNIVERSITES, Grenoble INP	Présidente
Adrien BIDAUD PROFESSEUR DES UNIVERSITES, Grenoble INP	Examinateur
Jean-Luc LECOUEY MAITRE DE CONFERENCES HDR, ENSI Caen	Rapporteur
Paolo VINAI PROFESSEUR ASSOCIE, Chalmers University of Technology	Rapporteur
Gilles BAN PROFESSEUR DES UNIVERSITES, ENSI Caen	Examinateur

Invités :

Benoit Geslot
INGENIEUR DOCTEUR, CEA Cadarache
Vincent Lamirand
DOCTEUR EN SCIENCES, EPFL

Acknowledgments

> Physics isn't the most important thing. Love is.
>
> Richard Feynman

None of this work would be even made possible without the advice and encouragement of my colleagues, friends and family. I finally have the opportunity to properly acknowledge everyone who supported me during the last three and a half years.

I would like to thank the jury members, Ms. Elsa Merle, Mrs. Adrien Bidaud, Gilles Ban, Simon Ravaux, for their availability to review my thesis work. I am grateful to Mrs Jean-Luc Lecouey and Paolo Vinai for their thorough review of my manuscript and various advice. My acknowledgments also go to M. Alain Moreau and Prof. Andreas Pautz for their consents of conducting my research work in their services.

Je remercie sincèrement Mme. Christine Coquelet-Pascal, cheffe de laboratoire des Programmes Expérimentaux et d'Essais en sûreté (LP2E) pour la disponibilité et les soutiens qu'elle a accordés pour mener à bien cette thèse. Je remercie M. Jean-Pascal Hudelot, ancien chef du LP2E, sans lequel ce projet de thèse n'aurait pas vu le jour.

Benoit, Vincent et Pierre, je me trouve incapable d'exprimer ma gratitude pour tous vous conseils et aides. Benoit, merci pour ta relecture attentive de tous les documents techniques (et toutes les versions des chapitres de ce mémoire d'ailleurs !) à une vitesse incroyable, ainsi que les discussions à la volée. Vincent, merci pour tes nombreux encouragements au quotidiené, pour toutes les heures passées dans la préparation et la réalisation de la campagne expérimentale. Je remercie Pierre pour ses nombreux conseils sur la modélisation, les analyses de données et la structuration de cette thèse.

Mes remerciements vont également à M. Frédéric Rodiac et M. Axel Narbonne pour leurs aides précieuses sur la conception de PISTIL ainsi que leurs suivis attentifs de la prestation de sa fabrication.

Je n'oublie pas de remercier l'équipe d'exploitation de CROCUS: Dr. P. Frajtag, M. D. Godat et M. L. Braun pour le temps passé en zone contrôlée de préparation et vérification, et entre autre la recherche onéreuse du niveau critique en salle de commande.

A great thank to the colleagues awarded as PhDs (already!): Augusto Di Chicco, Kornilius Routsonis, Julia Bartos, Tristan Julien, Stefan Radman, Alessandro Scolaro, Oskari Pakari and Fanny Vitullo. My best wishes goes to those who are still discovering this journey: Hamza Ghninou, David Friant, Georges Gay, Tom Mager, Edoardo Brunetto and Thomas Ligonnet.

Un grand merci au CEP et à l'équipe du FEU d'Aix. Merci pour vos dédications à organiser les moments de discussion, les repas et les sorties conviviales. Merci à Ban, Lin, Timothée, Catrina, Josh, Sésé et Guillaume pour tous les échanges.

感谢祂。感谢你们。

Abstract

The kinetic parameters of nuclear reactors describe the kinetic behavior of prompt and delayed neutrons, within a simplified representation of the time-dependent reactor physics model known as point kinetics. The knowledge of these parameters is essential to the operation of reactors and safety analysis. The delayed neutrons emitted by different precursors are conventionally aggregated into a small number of groups. There are differences between the definition and data of evaluated libraries, which leads to discrepancies in the calculations. The experimental determination of the kinetic parameters contributes to improve the accuracy of simulation tools and evaluated nuclear data used for industrial applications.

This thesis focuses on the reactivity modulation experiments implemented in the zero power research reactor CROCUS at EPFL for the determination of the transfer function of the reactor. The so-called zero-power transfer function is an integral observable of the kinetic parameters. A new experimental device was designed and manufactured to probe the reactor transfer function by a modulation of the core reactivity. The modulation effect is generated by the variation of the capture reaction rate of cadmium foils. It was necessary to calibrate the reactivity worth of PISTIL, which allowed the determination of the modulation amplitude of 4.415 ± 0.003 pcm.

Modulation experiments were conducted within two configurations with a variable fundamental frequency between 1.64 mHz and 200 Hz. A total of 135 phase and 94 amplitudes results were produced. These measured values were compared to computations of ZPTF using JEFF-3.3 and ENDF/B-VII.1 libraries. The results show that JEFF-3.3 predicts the kinetics of the delayed neutron precursors more accurately, while ENDF/B-VII.1 is in better agreement with the experiments at higher frequencies.

Keywords: reactor kinetics, delayed neutron, reactivity modulation, reactor transfer function, signal processing

Résumé

Les paramètres cinétiques des réacteurs nucléaires décrivent le comportement cinétique des neutrons prompts et retardés dans un modèle physique simplifié. Ce modèle est connu comme cinétique ponctuelle. La connaissance des paramètres cinétiques est essentielle pour le fonctionnement des réacteurs et l'analyse de sûreté. Les neutrons retardés émis par différents précurseurs sont conventionnellement rassemblés en un petit nombre de groupes. Il existe des différences entre la définition et les données dans les bibliothèques évaluées, ce qui entraîne des écarts dans les calculs. La détermination expérimentale des paramètres cinétiques contribue à améliorer la précision des outils de simulation et des données nucléaires évaluées.

Cette thèse se focalise sur les expériences de modulation de réactivité réalisées dans le réacteur de recherche à puissance nulle CROCUS pour la détermination de sa fonction de transfert du réacteur. La fonction de transfert à puissance nulle est considérée comme une observable intégrale des paramètres cinétiques. Un nouveau dispositif expérimental a été conçu et fabriqué pour mesurer la fonction de transfert du réacteur par une modulation de la réactivité du cœur. L'effet de modulation est généré par la variation du taux de réaction de capture des feuilles de cadmium. Il a été nécessaire d'étalonner l'effet en réactivité de PISTIL, ce qui a permis de déterminer l'amplitude de modulation à une valeur de 4,415 $\pm$ 0,003 pcm.

Les expériences de modulation ont été réalisées dans deux configurations avec une fréquence fondamentale variable entre 1,64 mHz et 200 Hz. Un total de 135 valeurs de phase et 94 valeurs d'amplitude ont été produites. Les valeurs mesurées ont été comparées aux calculs effectués en utilisant les bibliothèques JEFF-3.3 et ENDF/B-VII.1. Les résultats montrent que JEFF-3.3 prédit plus précisément la cinétique des précurseurs de neutrons retardés, tandis que ENDF/B-VII.1 est en meilleur accord avec les expériences à des fréquences plus élevées.

Mots-clés: cinétique du réacteur, neutron retardé, modulation de réactivité, fonction de transfert du réacteur, traitement du signal

Résumé Étendu

Contexte

Les paramètres cinétiques des réacteurs nucléaires décrivent le comportement cinétique des neutrons prompts et retardés produits par la réaction en chaîne. Ils interviennent dans un modèle simplifié de l'équation de transport des neutrons, nommé la cinétique ponctuelle. Il s'agit du modèle le plus utilisé dans l'industrie nucléaire pour l'étude du fonctionnement des réacteurs et l'analyse de sûreté associée.

Les neutrons retardés sont émis par environ 300 isotopes instables appelés précurseurs. Ces derniers sont conventionnellement regroupés en un petit nombre de groupes : cette approche est considérée comme suffisamment représentative de la cinétique réelle des réacteurs industriels. Néanmoins, il existe des différences entre les définitions et les données associées à ces groupes dans les bibliothèques de données nucléaires évaluées comme JEFF ou ENDF. Le choix de bibliothèque pour réaliser un calcul entraîne ainsi des écarts dans les résultats du temps de doublement du cœur, du poids en réactivité des barres de contrôle, etc. Ces écarts affectent l'estimation de la variation de puissance du réacteur, et par conséquent la conduite en opération normale tout comme en situation incidentelle et accidentelle.

Dans ce travail de thèse, nous nous sommes focalisés sur une méthode expérimentale pour améliorer la connaissance des paramètres cinétiques et contribuer à pallier la problématique de calcul des transitoires à cause de l'impact de la sélection de bibliothèque de données nucléaires. Cette méthode consiste à mesurer la réponse neutronique d'un réacteur à une perturbation externe, ce qui permet utilise le modèle de la Fonction de Transfert du Réacteur (RTF). Cette dernière est une observable intégrale des paramètres cinétiques pour les expériences en cœur.

Revue de littérature

Les études expérimentales de la RTF ont été réalisées dès le début des études en physique des réacteurs. La RTF décrit le comportement d'un réacteur nucléaire lorsqu'une perturbation d'origine neutronique ou mécanique se produit. Il s'agit d'une fonction de la fréquence à valeur complexe. Une autre application de la mesure de la RTF est de mieux comprendre les caractéristiques du réacteur : lorsque les effets de température sont négligeables, elle est appelé Fonction de Transfert à Puissance nulle (ZPTF) et est uniquement décrite par les paramètres cinétiques des neutrons prompts et retardés.

La mesure de la ZPTF consiste à réaliser une série d'expériences dans lesquelles le réacteur est modulé à différentes fréquences. L'acquisition des signaux temporels de réactivité et des détecteurs de neutrons permet d'estimer l'amplitude et la phase de la ZPTF à plusieurs fréquences discrètes (harmoniques de la fréquence fondamentale de la modulation). Une amplitude de modulation suffisamment élevée permet de

s'affranchir des incertitudes induites par les sources de bruit expérimentales. Cela nécessite le développement d'un dispositif expérimental dédié, appelé un modulateur.

La modulation s'appuie sur une variation de taux de réaction nucléaire, ce qui fait réagir la population neutronique au sein d'un réacteur. Pour réaliser cette modulation, la maîtrise de la perturbation, comme un mouvement, une variation de température ou de pression est indispensable. Du fait de la stabilité et de la simplicité en implémentation, la modulation par un mouvement piloté par un moteur est prépondérante parmi les modulateurs utilisés historiquement. C'est également la raison pour laquelle nous avons choisi d'exploiter cette option dans le cadre de cette thèse.

La modulation par mouvement est réalisée à l'aide du déplacement d'une pièce composée de matériaux fissile, absorbant ou modérateur/réflecteur. Deux types de concepts existent pour l'implémentation en pratique: soit le déplacement provoque une asymétrie de la configuration du cœur au sens neutronique, soit le déplacement génère une variation locale de spectre neutronique par effet d'autoprotection. Ce dernier a été retenu pour l'étude de conception d'un nouveau dispositif expérimental pour sa compacité ainsi que son impact mécanique et vibratoire moindre sur les structures adjacentes.

Le dispositif PISTIL

La modélisation neutronique d'un dispositif de modulation, nommé PISTIL, a été réalisé par code déterministe (APOLLO3®) et Monte Carlo (TRIPOLI-4®). Cette modélisation a permis l'estimation de la dimension des éléments actifs du dispositif ainsi que les matériaux associés. Dans un souci de temps de convergence du calcul Monte Carlo, un réseau de barreaux de combustible a été utilisé comme représentation simplifiée d'un réacteur, et les matériaux de différentes géométries y ont été modélisés : l'effet de modulation était estimé par la réactivité différentielle entre deux calculs de géométries différentes. Les calculs statiques (en mode de criticité) ont été réalisés pour cette estimation. Les calculs dynamiques n'ont pas été réalisés dû au temps de calcul excessivement élevé pour atteindre une convergence suffisante, compte tenu de divers matériaux et géométries à tester.

PISTIL est un dispositif rotatif qui génère la modulation par effet d'autoprotection. Le schéma conceptuel du dispositif est présenté dans la figure 1. L'ensemble est localisé dans un tube étanche en aluminium. A l'intérieur de la gaine se trouve une partie statique (stator) et une partie rotative (rotor) entraînée par un moteur à courant continu. Des secteurs de cadmium ont été déposés sur le stator et le rotor. Le cadmium est un fort absorbant de neutrons thermiques, sa présence provoque ainsi une réduction locale du flux thermique.

Lorsque les secteurs de cadmium sont recouverts comme indiqués dans la figure 1, une grande partie des neutrons thermiques est absorbée par les éléments de cadmium du stator et peu de réactions d'absorption ont lieu au niveau du rotor. Ainsi, l'anti-réactivité globale du système est minimisée. En revanche, avec une rotation de 90° du rotor l'effet en réactivité devient maximal. La variation de réactivité entre ces deux positions extrémales est réalisée de façon progressive selon les positions relatives du rotor et du stator. Un élément en polyéthylène (PE) se situe au centre du rotor afin de thermaliser localement le spectre neutronique pour améliorer la modulation.

PISTIL est doté d'un moteur rotatif avec une gamme de fréquence de fonctionnement

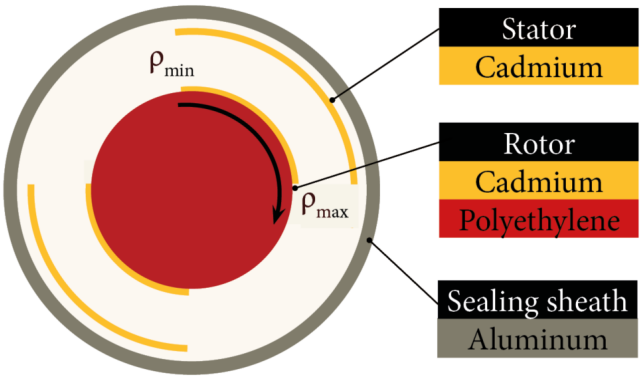

Figure 1: Schéma de principe de PISTIL

entre 1,64 mHz et 200 Hz. Le moteur est programmé pour réaliser deux types d'instruction de rotation : soit par une rotation à vitesse constante allant de $1°.s^{-1}$ à $36000°.s^{-1}$, soit par un mouvement pas-à-pas.

Pour le mouvement pas-à-pas, un profil de succession de mouvement a été défini. Il s'agit d'un profil basé sur une séquence pseudo-aléatoire binaire. Dans l'implémentation, PISTIL alterne entre deux positions angulaires qui correspondent à deux insertions de réactivités différentes. L'intérêt de l'utilisation des séquences pseudo-aléatoire est qu'elles permettent de générer une modulation avec un grand nombre d'harmoniques grâce à leurs propriétés mathématiques. Cela rend possible de mesurer la ZPTF de manière efficace, en particulier lorsque la fréquence fondamentale est faible.

Campagne expérimentale

Le dispositif PISTIL a été installé dans le réacteur CROCUS opéré par l'Ecole Polytechnique Fédérale de Lausanne.

CROCUS est un réacteur piscine avec deux types de barreaux de combustible d'uranium enrichis à 0,95 et 1,8%. Ces barreaux de 1 m en hauteur sont localisés dans une cuve cylindrique remplie d'eau, qui a pour rôle de modérateur et de réflecteur. Le réacteur est piloté par variation du niveau d'eau dans la cuve ou par l'insertion de deux barres de contrôle en B_4C. Le niveau d'eau maximal admissible est de 1000 mm.

La configuration expérimentale est celle de référence de CROCUS du benchmark [1], à la différence près qu'elle présente des grilles modifiées pour accueillir le dispositif d'oscillation du combustible COLIBRI. Les barreaux insérés dans COLIBRI sont en position nominales dans le réseau et les grilles supérieure et inférieure contiennent une couche de 1 mm de Cd au lieu de 0,5 mm de celles de référence. PISTIL est installé au centre du cœur. Quatre chambres à fission Photonis CFUL01 (1 g de dépôt en U235) en mode courant ont été utilisées pour la mesure du flux neutronique du réacteur. Les éléments de cadmium du stator et du rotor ont été centrés axialement à 550 mm de hauteur. Cette position axiale a été choisie car elle est la plus proche de la hauteur moyenne où le flux de neutrons atteint son maximum, de sorte que l'effet de modulation est maximisé.

L'étalonnage en réactivité a été réalisé avec trois méthodes différentes: par compen-

sation de la réactivité, période asymptotique et cinétique inverse. Les trois méthodes ont donné des résultats cohérents. Par la méthode de cinétique inverse, un profil d'effet en réactivité a été obtenu. On en déduit une amplitude maximale de modulation de 4,415 ± 0,003 pcm. La mesure par période asymptotique avait pour but de déterminer la différence de réactivité introduite lorsque PISTIL fonctionnait en mouvement pas-à-pas.

Un total de 42 expériences de modulation a été réalisé, appelées ci-après expériences continues et pas-à-pas.

Résultats de mesure

Les signaux de mouvement de PISTIL ont été mesurés. Ils ont étés convertis en signaux de réactivité en utilisant l'étalonnage réalisé avec la méthode de cinétique inverse. Les signaux des détecteurs de neutron ont été mesurés en parallèle. Leurs Densités Spectrales de Puissances (APSD) et Densités Spectrales de Puissances Croisées (CPSD) ont été calculés pour en déduire l'amplitude et la phase de la ZPTF. L'analyse a été réalisée sur la fondamentale de la modulation pour les expériences continues et sur les 50 premières harmoniques en pas-à-pas. Ce choix a été fait suivant le critère de rapport de signal-à-bruit (SNR): les harmoniques en expérience continue n'ont pas été analysées, car elles avaient un SNR inférieur à 1 % de celle de la fondamentale et les incertitudes de mesure étaient importantes.

Les puissances ont été calculées comme la moyenne des puissances des signaux des détecteurs de neutron pour chaque expérience. L'incertitude a été estimée comme la somme quadratique de la dispersion des données et de l'incertitude de chaque mesure pour tenir en compte des désaccords des résultats comparés à l'incertitude individuelle des détecteurs.

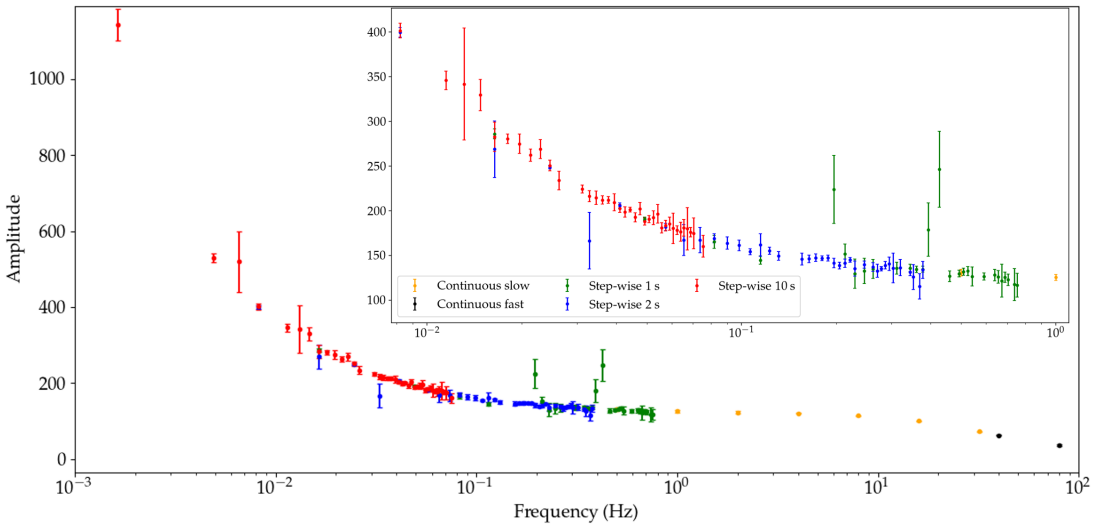

Figure 2: Mesure de l'amplitude du ZPTF de CROCUS

Les résultats de mesure de l'amplitude sont illustrés sur la figure 2. Les mesures montrent la cohérence entre les mesures en continu et les données pas-à-pas. A titre

d'illustration, la différence d'amplitude de l'harmonique à 0,508 Hz par rapport aux données continues à 0,5 Hz est de 6,16 ± 5,21, soit moins de 3 % en différence relative.

Les résultats de mesure de phase sont illustrés sur la figure 3. Les résultats en rotation continue ont été considérés invalides et seules les mesures en pas-à-pas ont été conservées. La justification du rejet des mesures en continu est le manque de répétabilité entre valeurs mesurées, ainsi qu'un défaut de synchronisation entre les systèmes de mesure qui introduit un biais systématique des mesures avec l'augmentation de la durée de mesure.

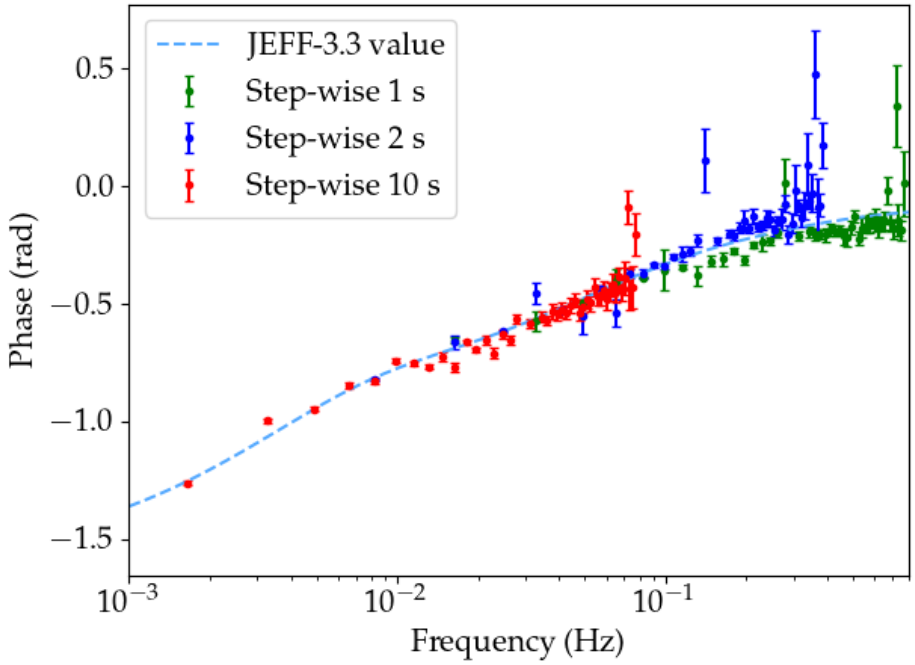

Figure 3: Phase mesurée du ZPTF de CROCUS

Comparaison avec le calcul

Les résultats expérimentaux sur l'amplitude et la phase sont comparés aux valeurs calculées en utilisant les paramètres cinétiques de CROCUS, estimés à partir de simulations TRIPOLI-4 avec JEFF-3.3 et ENDF/B-VII.1 comme bibliothèques de données nucléaires. Les racines de l'erreur quadratique moyenne (ci-après RMSE) entre calculs et mesures sont indiquées dans le tableau 1. Les RMSEs sont utilisés comme critère de comparaison. De manière globale, il y a un meilleur accord entre le modèle théorique et les mesures à basse fréquence ($< 0{,}1$ Hz) en utilisant JEFF-3.3 alors qu'à des fréquences plus élevées ENDF/B-VII.1 fournit des estimations de ZPTF qui se rapprochent plus des mesures. Cela suggère que JEFF-3.3 présente un formalisme plus adapté pour décrire le comportement des neutrons retardés et ENDF/B-VII.1 permet une meilleure représentation de la relation entre le temps de génération des neutrons prompts et la fraction des neutrons retardés.

Tableau 1: RMSE d'amplitude et de phase en utilisant des paramètres cinétiques calculés

		ENDF/B-VII.1	JEFF-3.3
Amplitude	Pas-à-pas	1,395 ± 0,010	1,042 ± 0,038
	Continues	1,077 ± 0,258	6,163 ± 0,118
Phase	Pas-à-pas	4,894 ± 0,055	-
	Continues	2,577 ± 0,053	-

A partir des données de mesure et le modèle de ZPTF, une estimation expérimentale de paramètres cinétiques (fraction des neutrons retardés, temps de génération) est proposée. Cette étude est limitée à une approche de fit en moindre carré pondéré. Selon les formalismes différents sur les paramètres cinétiques entre ENDF et JEFF, le nombre de paramètres à déterminer est respectivement 13 et 9. Il a été observé que la quantité de données obtenue dans le cadre de cette thèse est insuffisante pour estimer l'ensemble des paramètres avec une précision satisfaisante et une incertitude maitrisée. En revanche, l'analyse a permis d'obtenir la fraction totale des neutrons retardés et la demi-vie moyenne des précurseurs, comme montré dans le tableau 2.

Les écarts calcul-mesure illustrent que les calculs à base de JEFF-3.3 donnent une meilleure prédiction du comportement global de la cinétique des neutrons retardés.

Tableau 2: Valeurs calculées et mesurées d'observables intégraux en utilisant JEFF-3.3 et ENDF/B-VII.1

	ENDF/B-VII.1			JEFF-3.3		
	Calculé	Mesuré	C/E-1	Calculé	Mesuré	C/E-1
Λ (s)	47.502 ± 0.001	47.838 ± 0.280	-0.29 ± 0.58%	47.703 ± 0.001	50.037 ± 0.337	-4.75 ± 0.64%
β_{eff} (pcm)	737.2 ± 3.6	739.4 ± 4.2	-0.29 ± 0.75%	758.7 ± 3.7	796.5 ± 5.3	-4.75 ± 0.78%
$T_{1/2}$ (s)	7.31 ± 0.06	7.84 ± 0.14	-6.76 ± 1.84%	8.52 ± 0.05	8.45 ± 0.09	-0.81 ± 1.21%

Conclusion et perspectives

Ce travail de thèse a été consacré aux études expérimentales pour une meilleure caractérisation du comportement cinétique du réacteur. L'approche est basée sur le développement d'un dispositif expérimental pour moduler la réactivité dans le réacteur CROCUS. Une série d'expériences a été réalisée dans ce réacteur afin de mesurer sa ZPTF qui est considérée comme observable intégrale des paramètres cinétiques. L'amplitude et la phase de la ZPTF de CROCUS ont été mesurées sur une plage de fréquences entre 1,6 mHz et 200 Hz. Un total de 135 mesures de phase et de 94 mesures d'amplitude a été retenu comme données expérimentales valides pour mesurer de façon intégrale les paramètres cinétiques.

On souligne l'intérêt de réaliser des expériences continues et pas-à-pas comme deux approches complémentaires, avec une gamme de fréquence d'intérêt différente. Les mesures pas-à-pas sont à privilégier car elles présentent la particularité d'être indépendantes d'un étalonnage en réactivité pour l'analyse de phase, ainsi qu'un besoin moins exigeant sur la connaissance de la variation de réactivité. Une autre raison de privilégier l'utilisation d'expériences pas-à-pas pour la mesure de ZPTF est que, dans ce cas de figure il est possible d'optimiser l'expérience avec un profil de mouvement choisi au préalable.

Les mesures réalisées ont permis la comparaison des résultats expérimentaux aux calculs réalisés avec les données de bibliothèques JEFF-3.3 et ENDF/B-VII.1. Avec la méthodologie expérimentale implémentée dans cette thèse, la qualité des mesures, notamment à fréquence réduite, sont suffisamment faibles pour mettre en évidence les différences en termes d'écart calcul-mesure en fonction de la bibliothèque utilisée. L' amélioration et l'optimisation de l'approche expérimentale permettraient de produire des données d'incertitude plus réduite pour l'amélioration de connaissance en données nucléaires liées à la cinétique des réacteurs.

En perspective, il serait intéressant d'étudier la source de l'écart entre les calculs et les phases obtenues au-dessus de 1 Hz et notamment son lien avec le défaut de synchronisation et l'impact des effets de cinétique spatiale. Les amplitudes et phases mesurées sont compatibles avec les valeurs calculées avec JEFF-3.3 et ENDF/B-VII.1, mais le niveau de cohérence entre les calculs et les mesures en fonction de la fréquence de mesure. Cela reflète les zones d'intérêt pour les travaux futurs d'interprétation et d'assimilation qui permettraient d'évaluer l'impact des données expérimentales pour améliorer la précision des calculs en cinétique. La comparaison entre le modèle de calcul et les résultats expérimentaux permettrait également de déterminer les nouvelles expériences à réaliser en tant que complément de l'étude réalisée dans cette thèse, ainsi que les améliorations à apporter sur les mesures pour la vérification de répétabilité et la réduction d'incertitude.

Contents

List of Figures

List of Tables

Abbreviation

ADS Accelerator-Driven System

APHRODITE Amplitude and PHase Response of an Oscillating Device Investigated by Theory and Experiment

APSD Auto Power Spectral Density

CEA French Atomic and Alternative Energy Commission

CPSD Cross Power Spectral Density

EPFL Ecole Polytechnique Fédérale de Lausanne

FC Fission Chamber

FFT Fast Fourier Transform

FPGA Field Programmable Gate Arrays

FWMH Full Width at Half Maximum

GUI Graphical User Interface

IFP Iterated Fission Probability

LTI Linear Time Invariant

MLS Maximum Length Sequence

NC Numerical Control

PISTIL Periodic reactivity Injection System Transient Induced Locally

PK Point Kinetics

PRBS Pseudo-Random Binary Sequence

PSD Power Spectral Density

QOI Quantity of Interest

RMSE Root-Mean-Square Error

rpm Revolutions Per Minute

RR Reaction Rate

RT Real-Time

RTF Reactor Transfer Function

SNR Signal-to Noise Ratio

UDP User Datagram Protocole

UQ Uncertainty Quantification

ZPR Zero-power Reactor

ZPTF Zero-Power reactor Transfer Function

Chapter 1

Introduction

1.1 Context

In 1942, a team of scientists led by Enrico Fermi built the first nuclear reactor [2], four years after the discovery of nuclear fission. The fission of heavy nuclides such as ^{235}U, ^{238}U and ^{239}Pu emits on average 2-3 neutrons to maintain the fission chain reaction. It was also discovered that some neutrons are emitted with a significant delay with respect to the fission process [3]. These delayed neutrons originate from successive β^- decays of various fission products, referred to as precursors. They represent less than 1% of the neutrons produced promptly (in less than 1×10^{-14} s) after the fission of ^{235}U (*Cf.* chapter 1 of [4]). However, their delayed nature is of fundamental importance to control the fission rate, which made it possible to use nuclear energy for sustainable production of electricity.

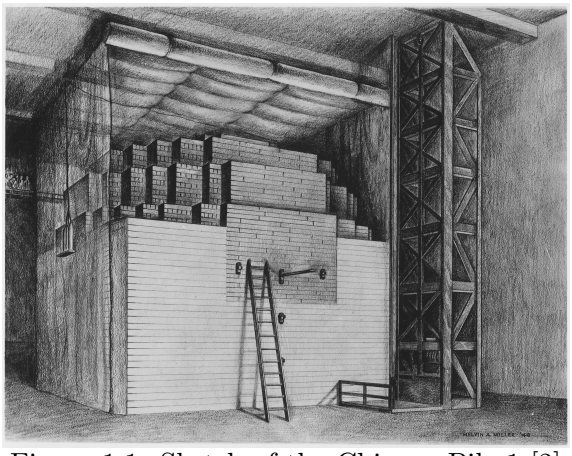

Figure 1.1: Sketch of the Chicago Pile-1 [2]

Following the successful approach to criticality of the Chicago Pile-1 (CP-1), several research reactors were built [5]. The nuclear power industry then saw a rapid growth around the globe in the 1960s as an economical option to meet the energy needs [6] in multiple countries.

In the CP-2 reactor, which was the successor of CP-1, researchers focused on the measurement of a new quantity predicted by physical models called the Reactor Transfer

Function (RTF). The RTF describes the behavior of a nuclear reactor when a perturbation occurs at a certain position and time. The notion of transfer function exists in a large number of engineering applications. It considers a physical system as a Linear Time Invariant (LTI) system [7] that reacts to an external perturbation. A LTI system's response to the perturbation is invariant in time. For a perturbation combined of two components different in the temporal evolution, the response is a sum of the responses to the individual component.

The measurement of the RTF allowed the investigation of the stability of the reactor in various situations, which was of importance in the early years of the operation of the reactors. The first RTF measurement was performed in 1952 [8]. Measurements were also conducted in other research and industrial reactors [9].

The kinetic parameters are involved in the model of RTF, which make another application of the RTF measurement to be the characterization of the kinetics of prompt and delayed neutrons in the core.

1.2 Motivations

As for the operation of nuclear reactors, it is essential to have an accurate prediction of the power variation for the needs to balance between the fluctuating demands and the electricity production. The reactor kinetics offer models to fulfill this need. The term "reactivity" was introduced to describe the kinetic state of the core. Additional requirements of precision are for the prediction of the core reactivity in maintenance, core configuration change and design of new reactors. Thus, calculation tools were developed to simulate the nuclear reactions that take place in reactors for the inference of the core reactivity in various reactor configurations. The simulations are dependent primarily on the so-called evaluated nuclear data, that are provided on the basis of theoretical models and experimental data.

For the simulation of the fission process, the principal parameters of interest are prompt neutron multiplicity, energy spectrum, relative fractions and decay constants of delayed neutrons produced by various isotopes and cross sections of fission, capture, diffusion reactions. International effort is made to provide evaluated data collected in libraries. We can cite for instance the Evaluated Nuclear Data File Library ENDF [10], the Joint Evaluated Fission and Fusion data library JEFF [11] and the Japanese Evaluated Nuclear Data Library JENDL [12]. Reviewing the quality of the evaluated data is a challenging task, as there might be biases or errors introduced in each step of the experiments and evaluation process [13]. The origin of the biases and errors may be undocumented or complicated to retrace due to the large time span and the number of evaluators. For this reason, these data are constantly being updated in the libraries accompanying new experimental evidences and refinement of theoretical models. The attempt to increase the accuracy at both research and industrial level is also a drive behind.

With the exponential growth of computing power, the simulation tools are considered primarily as a more efficient solution to provide estimations in the field of reactor physics as compared to experiments. There is a challenge in the current context of reactor physics research, which is to propose solutions to reduce discrepancies between model predictions and experimental observations.

One of the experimental way is to update evaluated libraries through reactor experiments by considering the reactor as a source of particles. The measurements are referred to as in-core integral experiment. A large number of kinetic parameter measurements were conducted and documented in the literature, most of them focused on the measurement of delayed neutron related data.

To date, about 300 delayed neutron precursors have been identified (*cf.* Ch.2 of [4]). The pioneer experimental work of G. R. Keepin in 1957 [14] suggested that a few equivalent groups can describe sufficiently well the overall delayed neutron kinetics. By setting both the abundances and half-lives of precursor groups as variables, he applied non-linear least-square fit methods to the experimental decay data and recommended a 6-group model, which led to 12 evaluated quantities that are isotope and energy dependent. Recent studies argued that an 8-group model with a fixed value of half-lives, based on the identification of the predominant precursors would provide a better physical representation of the delayed neutron emission [15], with 8 evaluations of abundances. Additionally, in this 8-group model, the same decay constants are attributed for isotopes of the same element.

In the current state, there were reported discrepancies up to 16 % between the calculated mean precursor half-life of ^{235}U systems using the kinetic parameters evaluated in JEFF [11](8-group) and ENDF [10] (6-group) nuclear data libraries.

In recent years, it has been made possible to evaluate the prompt and delayed neutron kinetic parameters in deterministic reactor physics codes [16]–[18] and recent developments in Monte Carlo codes (e.g. MCNP6 [19], Serpent2 [20], TRIPOLI-4® [21], etc.). However, the reactivity and kinetic parameter estimations are susceptible to biases in the choice of model and nuclear data evaluations [22], [23]. Further, a lack of documentation of the Uncertainty Quantification (UQ) in the evaluations was identified [15]. Inconsistencies as compared to experimental kinetic parameter measurements were reported as well [24], [25]. To overcome these problems, new experimental data of delayed and prompt neutron data are required.

Measurement of the kinetic parameters are conducted through three complementary experimental approaches [26].

First, the microscopic approach focuses on the measurement and evaluation of the individual precursor half-life, the delayed neutron emission probability and the energy spectrum. The measurements consist in irradiating a sample material by a particle beam and measure the neutron, β or γ emitted by the specific isotope in order to single out its contribution among the fission products. Microscopic experiments contribute to improve the knowledge of fundamental physical properties of various isotopes of interest.

Second, the macroscopic approach concerns the irradiation of a fissile material sample in order to observe the radioactive decay of all the produced precursors and the consequent delayed neutron emission. The neutron source can be for instance nuclear reactor flux or reactions of accelerator-based neutron production. The precursors having various time scales in half-life are sorted into groups that are distinguished through the temporal evolution of post-irradiation neutron emission. As in the work of Keepin [14], from this kind of experiment are inferred the delayed neutron yield, the relative abundances a_i and the decay constants λ_i of the considered delayed neutron groups. The data are then interpreted and assimilated into nuclear data libraries as evaluations.

Third, the integral approach is the direct measurement of the kinetic parameters of

nuclear systems. Different measurement types employed are the following:

- Dynamical methods deal with time dependent transients of the reactor behavior by introducing a step-wise reactivity or source strength change, such as asymptotic period, rod drop and source jerk methods [27]–[29].

- Branching noise, also referred to as pile noise methods treat the statistic fluctuation of reactor power at steady state due to the branching process, such as Rossi-α, Feynman-α and power spectral density methods [30], [31]. The kinetic information contained in the fluctuation is extracted from the analysis of correlations between neutron detection events.

- Pile oscillator or modulation method [32] consists in the introduction of a perturbation in the reactor core and the observation of the response of the neutron population. The relationship between the perturbation and the power variation can be described by transfer function models that are frequency dependent. This method allows the investigation of the RTF in the frequency domain.

1.3 Objectives and structure

The present Ph.D work was carried out within the framework of a collaboration between the French Atomic and Alternative Energy Commission (CEA) and Ecole Polytechnique Fédérale de Lausanne (EPFL).

At CEA, extensive research has been performed for the experimental determination of kinetic parameters and the assimilation of associated nuclear data. The delayed neutron parameters were re-evaluated by the combination of the summation calculation of the individual contribution of each precursor [33], [34] and the assimilation of experimental data from the works of [35]–[37]. The ultimate goal is to integrate these results of kinetic parameters in future version of JEFF library. At EPFL, experimental studies were conducted in the research reactor CROCUS of EPFL for the determination of the reactor kinetic parameters using branching noise measurements [38], [39]. Modulation studies are also performed for a different prospect, namely the study of the impact of mechanical perturbations. [40].

We investigate in this thesis the extension of these previous efforts to novel prospects of in-core experiments, in order to answer the challenges of neutron kinetics concerning the measurements of kinetic parameters. We focus on the experimental studies of the RTF as integral observable with modulation experiments. For a low power reactor like CROCUS, the temperature feedback effects are neglected, and the RTF is referred to as the Zero-Power Transfer Function (ZPTF) which is described by kinetic parameters.

It is well-known that the branching noise and the modulation experiments can be used for the measurement of the ZPTF. Although noise measurements are no-intrusive in nature and easier to implement than modulation experiments, it is limited in low frequency measurements due to important acquisition time required to reduce the uncertainties. Furthermore, the phase information lost in the analysis of the noise can be measured by modulation, which provides two observables in one experiment. This motivated the studies on the reactivity modulation of this work.

The thesis is structured as following:

The theoretical elements regarding the physics of nuclear reactor kinetics are presented in chapter 2. We also review the model of ZPTFs and the ZPTF measurements carried out in the past.

Then, chapter 3 concerns the development of an experimental device for the realization of modulation experiments to probe the reactor's ZPTF obtained from analyzing the signals of neutron detectors. The experiments involved modulations of the reactivity. A reactivity modulation device was developed in this framework and tested in CROCUS.

The chapter 4 presents the design of the first experimental campaign and the analysis methods involved for the acquired data.

The analysis of experimental data and the results are discussed in chapter 5. The ZPTF of the CROCUS reactor is shown and compared to the values predicted by the calculations. Several considerations regarding the experimental campaign are listed for future works.

Chapter 2

Reactivity Modulation in Zero-Power Reactors

This chapter summarizes the theoretical background of the reactor kinetics concerning the reactor transfer function model. We present the so-called zero-power transfer function from the point kinetic approximation. The experimental studies for the measurement of the reactor transfer function is also discussed.

2.1 Fundamentals of nuclear reactor kinetics

2.1.1 The Boltzmann equation

The time dependency of the nuclear reactor power variation is described by models of reactor physics, in which there are differences in time scales between the production of prompt and delayed neutrons. The time constants associated with the precursors' decay are of several orders of magnitude larger than that of the prompt neutrons. As an illustration, the average half-life of delay neutron precursors in a ^{235}U fueled system is approximately 9 s [41]. Another difference between prompt and delayed neutrons is that the latter is emitted at lower energy than the former, which induces differences in reaction rates, fission neutron yield and leakage for maintaining the fission chains.

The in-core neutron flux distribution $\bar{\phi}$ is governed by prompt and delayed neutron dynamics with respect to time t, position $\vec{x}$, direction $\vec{\Omega}$ and energy E. It is described by

the time-dependent Boltzmann neutron transport equation as:

$$\begin{aligned}
&\frac{1}{v}\frac{\partial}{\partial t}\bar{\phi}(\vec{x},\vec{\Omega},E,t) = (\chi_p(E)(\mathbf{1}-\bar{\beta})\mathbf{F}-\mathbf{M})\bar{\phi}(\vec{x},\vec{\Omega},E,t) + \sum_{i=1}^{N}\lambda_i\chi_{d,i}(E)\bar{C}_i(\vec{x},t) + Q_{ext}(\vec{x},t)\\
&\frac{\partial \bar{C}_i(\vec{x},t)}{\partial t} = -\lambda_i\bar{C}_i(\vec{x},t) + \bar{\beta}_\mathbf{i}\mathbf{F}\bar{\phi}(\vec{x},t)
\end{aligned} \tag{2.1}$$

where:

- $\mathbf{F}$ is the fission operator
- $\mathbf{M}$ is the migration and loss operator
- $(1-\bar{\beta})\mathbf{F}$ and $\bar{\beta}_i\mathbf{F}$ are respectively the production operator of prompt neutrons and delayed neutrons emitted by the precursor i. $\bar{\beta}_i$ are referred to as the delayed neutron fraction of the precursor i while $\bar{\beta} = \sum_i \bar{\beta}_i$ is the total fraction of delayed neutrons.
- $\chi_p(E)$ and $\chi_{d,i}(E)$ are respectively the emission energy spectrum of prompt neutrons and delayed neutrons of precursor i.
- λ_i and $\bar{c}_i(\vec{x},t)$ are respectively the decay constant and concentration of precursor i.
- $Q_{ext}(\vec{x},t)$ is the external neutron source in addition to neutrons produced by the in-core fission.

For a stationary reactor, the solution of the Boltzmann equation gives the flux $\bar{\phi_0}(\vec{x},\Omega,E)$ that corresponds to a balance between neutron production, migration and loss:

$$\mathbf{F}_0\bar{\phi_0}(\vec{x},\vec{\Omega},E) = \mathbf{M}_0\bar{\phi_0}(\vec{x},\vec{\Omega},E) \tag{2.2}$$

where the prompt and delayed neutron contributions to fission is [42]:

$$\begin{aligned}
\mathbf{F}_0\bar{\phi_0}(\vec{x},\vec{\Omega},E) = &\underbrace{\int_0^\infty dE\int_0^{4\pi}d\vec{\Omega}\int_\mathbf{V}dx\chi_p(E)(1-\bar{\beta})\Sigma_f(\vec{x},\vec{\Omega},E)\bar{\phi_0}(\vec{x},\Omega,E)}_{\text{Prompt neutron production}}\\
&+\underbrace{\sum_{i=1}^{N}\int_0^\infty dE\int_0^{4\pi}d\vec{\Omega}\int_\mathbf{V}d\vec{x}\chi_{d,i}(E)\bar{\beta}_i\Sigma_f(\vec{x},\vec{\Omega},E)\bar{\phi_0}(\vec{x},\vec{\Omega},E)}_{\text{Total delayed neutron production}}
\end{aligned} \tag{2.3}$$

2.1.2 The point kinetics equation and kinetic parameters

The resolution of the time-dependent Boltzmann equation is time-consuming and computationally intensive, which is unfeasible for the estimation of power transients in industrial nuclear reactors. A reactor close to its steady state is well described [42] by a factorization of the time evolution from other variables:

$$\bar{\phi}(\vec{x},\vec{\Omega},E,t) = n(t)\bar{\phi}(\vec{x},\vec{\Omega},E) \tag{2.4}$$

In this formulation, $\bar{\phi}(\vec{x}, \vec{\Omega}, E)$ represents a time-invariant neutron flux shape function, and $n(t)$ is the amplitude of the power variation as a function of time.

Physically, a transient between two reactor states generates the variation of the flux shape. Correction has to be applied in order to account for the flux shape difference as compared to $\bar{\phi}_0(\vec{x}, \vec{\Omega}, E)$. A weighted multiplication of the transport equation by $\phi_0^\dagger(\vec{x}, \vec{\Omega}, E)$ is applied for this purpose. For a reactor near criticality, the applied weight represents the importance of the neutrons in maintaining the in-core neutron population with respect to the position, direction and energy [42].

In the case of a initially stable reactor, the solution of the adjoint-weighted transport equation in the initial stationary state $\phi_0^\dagger(\vec{x}, \vec{\Omega}, E)$ is commonly used:

$$\mathbf{F}_0^\dagger \phi^\dagger(\vec{x}, \vec{\Omega}, E) = \frac{1}{k} \mathbf{M}_0^\dagger \phi^\dagger(\vec{x}, \vec{\Omega}, E) \tag{2.5}$$

where $\mathbf{F}_0^\dagger$ and $\mathbf{M}_0^\dagger$ are respectively the adjoint of fission and migration operators of a steady state reactor and k is the multiplication factor.

For a reactor at criticality, the factor $1/k$ can be omitted as $k = 1$.

In this manner, the Point Kinetics (PK) equations is formulated as a spatially and energetically integrated representation of the reactor behavior as [42]:

$$\begin{cases} \frac{dN(t)}{dt} & = \frac{\rho(t) - \beta_{\text{eff}}}{\Lambda} N(t) + \sum_{i=1}^{G} \lambda_i C_i(t) + Q(t) \\ \frac{\mathrm{d}C_i(t)}{\mathrm{d}t} & = \frac{a_i \beta_{\text{eff}}}{\Lambda} N(t) - \lambda_i C_i(t) \end{cases} \tag{2.6}$$

A detailed and rigorous derivation of the PK equation and the involved terms can be found in [43, Ch. 8]. A brief summary of the definition of the so-called neutron kinetic parameters are as following:

- Λ, the prompt neutron generation time (s)

$$\Lambda = \frac{(\phi_0^\dagger, \frac{1}{v}\phi)}{(\phi_0^\dagger, \mathbf{F}_0 \phi)} \tag{2.7}$$

- $a_i \beta_{\text{eff}} = \beta_{\text{eff,i}}$, the effective delayed neutron fraction of the precursor i in a G-group formulation

$$\beta_{\text{eff,i}} = \frac{(\phi_0^\dagger, \bar{\beta}_i \mathbf{F} \phi)}{(\phi_0^\dagger, \bar{\beta} i \mathbf{F}_0 \phi)} \tag{2.8}$$

- $C_i(t)$, the concentration of the precursor group i in a G-group formulation

$$C_i(t) = \frac{(\phi_0^\dagger, \chi_i \bar{C}_i(t))}{\Lambda(\phi_0^\dagger, \mathbf{F}_0 \phi)} \tag{2.9}$$

- ρ, the reactivity

$$\rho = \frac{(\phi_0^\dagger, (\mathbf{F} - \mathbf{M})\phi)}{(\phi_0^\dagger, \mathbf{F}_0 \phi)} \tag{2.10}$$

The term "effective" distinguishes the $\beta_{\text{eff,i}}$ from the absolute delayed neutron fraction that are related to the proportion and the yield of the precursor groups. It takes into account the importance of the delayed neutrons of different groups in the maintaining the fission chains.

2.2 Reactor kinetics in the frequency domain

2.2.1 Derivation of the zero-power reactor transfer function

The introduction of transfer function models in the nuclear field was inspired by the analogy in automatic control [44], [45], as they give an insight on the reactor stability with concerning an external perturbation. A schematic of the LTI representation of nuclear reactors is shown in figure 2.1. The reactor is described by the kinetic parameters and its reactivity at steady state. Following the variation of a nuclear reaction rate, the core reactivity varies and result in a change in the in-core neutron population. This may induce temperature related feedback effects to compensate the impact of the reactivity variation. The measurement of the reactor transfer function can be achieved by perturbing periodically the reactivity of the core, referred to as reactivity modulation in the rest of this document.

A reactor is at zero-power when it operates at low power (< 1000 W). In a Zero-power Reactor (ZPR), the temperature-related effect can be neglected. As a consequence, feedback effects are neglected. In this case, the reactor transfer function is referred to as the Zero-Power reactor Transfer Function (ZPTF). It consists in a model to characterize the kinetics of the reactor that are described by the effective kinetic parameters.

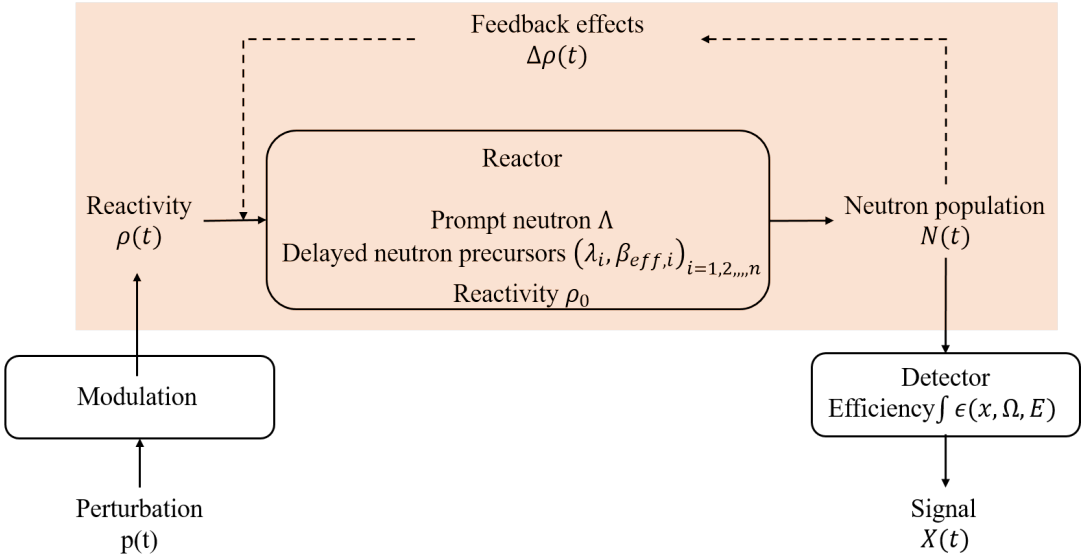

Figure 2.1: Representation of a nuclear reactor as an LTI system

The ZPTF can be derived from the PK equations. For a reactor at steady state at time t_0, $Q(t=0) = Q_0$. The reactor parameters (N_0, C_{i0}, ρ_0) are defined as:

$$\begin{cases} N_0 = -\dfrac{\Lambda}{\rho_0} Q_0 \\ C_{i0} = \dfrac{\beta_{\text{eff,i}}}{\lambda_i \Lambda} N_0 \quad \text{for } i = 1, 2, ..., n \end{cases} \tag{2.11}$$

When it undergoes a transient due to a reactivity modulation, the reactor can be

modeled as a sum of the steady state and a time-dependent state:

$$\begin{cases} \rho(t) = \rho_0 + \delta\rho(t) \\ N(t) = N_0 + \delta N(t) \\ C_i(t) = C_{i0} + \delta C_i(t) \end{cases} \tag{2.12}$$

The condition $\lim_{t\to 0^+} \delta n(t) = \lim_{t\to 0^+} \delta\rho(t) = 0$ is admitted as the reactor is initially at steady state.

By substituting equation (2.6) with equation (2.12) and equation (2.11):

$$\begin{cases} \frac{d\delta N(t)}{dt} & = \frac{\rho_0 - \beta_{\text{eff}}}{\Lambda}\delta N(t) + \sum_{i=1}^{G} \lambda_i \delta C_i(t) + \frac{N_0}{\Lambda}\delta\rho(t) + \frac{1}{\Lambda}\delta\rho(t)\delta N(t) \\ \frac{d\delta C_i(t)}{dt} & = \frac{a_i \beta_{\text{eff}}}{\Lambda}\delta N(t) - \lambda_i \delta C_i(t). \end{cases} \tag{2.13}$$

The source term is not present in equation (2.13) as it is considered constant ($Q(t) = Q(t=0) = Q_0$). The second order variation $\delta N(t)\delta\rho(t)$ is considered negligible, and the non-linearity in the equation vanishes. This is often referred to as the small fluctuation approximation [7]. For a large and localized reactivity variation, it is possible that the non-linear effects in equation (2.13) make the ZPTF model lose its validity. It was suggested in the literature to limit the reactivity worth to less than 1% of the β_{eff} (i.e. $\sim$1¢) [46] to preserve the validity of the ZPTF with respect to experimental data.

Applying the Laplace transform [47] to equation (2.13) , the zero-power transfer function is obtained:

$$\bar{G(s)} = \frac{\delta N(s)}{\delta\rho(s)} = \frac{N_0}{\Lambda s + \sum_i^n \frac{\beta_{\text{eff,i}} s}{s+\lambda_i} - \rho_0} = \frac{N_0}{\Lambda(s + \sum_i^n \frac{\beta_{\text{eff,i}}/\Lambda}{s+\lambda_i} s - \rho_0/\Lambda)} \tag{2.14}$$

In many studies, the steady state is assumed to be critical without external neutron source. Therefore, by setting $Q = 0$, $\rho_0 = 0$, the transfer function is defined by the neutron generation time Λ and delayed neutron parameters ($\beta_{\text{eff},i}$, λ_i).

Alternatively, the reactor frequency response to an oscillating neutron source can be modeled in a similar manner as the ZPTF:

$$\bar{G_q(s)} = \frac{\delta N(s)}{\delta Q(s)} = N_0 \frac{\Lambda}{\Lambda s + \sum_i^n \frac{\beta_i s}{s+\lambda_i} - \rho_0} = \frac{N_0}{s + \sum_i^n \frac{\beta_i/\Lambda}{s+\lambda_i} s - \rho_0/\Lambda} \tag{2.15}$$

Equation (2.15) is sometimes called the source transfer function in the literature [48]. It is evident that equation (2.14) and equation (2.15) are only different by a normalizing constant of N_0/Λ. By contrast, the source transfer function is not restricted to small perturbations, as the source strength is independent from the in-core neutron flux [7]. A strong source strength variation, however, would induces spatial effects that makes the PK approximation invalid and consequently the transfer function model [49].

2.2.2 Physical interpretation of the ZPTF

When the aforementioned perturbation is periodic, it is common to substitute the complex variable s in $\bar{G(s)}$ by $j\omega$. ω corresponds to the angular frequency (rad.s^{-1}), and j is the

unit imaginary number. This can be understood as a decomposition of a modulation into a sum of sinusoidal harmonics $\sum_n A_n e^{nj\omega t}$ using the Fourier analysis.

The ZPTF is a frequency domain model that describes the variation of the in-core neutron population of a point reactor with respect to a reactivity variation, which is equivalent to the reactor behavior described by PK equations in the time domain.

Using the definition in equation (2.14), $G(j\omega)$ is expressed as:

$$G(\bar{j}\omega) = \frac{N_0}{a(\omega) + jb(\omega)} \tag{2.16}$$

where

$$a(\omega) = -\rho_0 + \sum_i^n \frac{\beta_{\text{eff},i}\omega^2}{\lambda_i^2 + \omega^2} \tag{2.17}$$

$$b(\omega) = (\Lambda + \sum_i^n \frac{\beta_{\text{eff},i}\lambda_i}{\lambda_i^2 + \omega^2})\omega \tag{2.18}$$

The information of transfer function is characterized by a frequency dependent amplitude $||\ G(j\omega)\ ||$ and a phase $arg[G(j\omega)]$, defined as:

$$||\ G(j\omega)\ ||= \frac{1}{N_0}\ ||\ G(\bar{j}\omega)\ ||= \frac{||\ \delta N(j\omega)\ ||}{||\ \delta\rho(j\omega)\ ||} = \frac{1}{\sqrt{a^2(\omega) + b^2(\omega)}} \tag{2.19}$$

$$arg[G(j\omega)] = arg[\delta N(j\omega)] - arg[\frac{\delta\rho(j\omega)}{||\ \delta\rho(j\omega)\ ||}] = -arctan[\frac{b(\omega)}{a(\omega)}] \tag{2.20}$$

It should be noted in equation (2.19), the amplitude is normalized to the mean reactor power N_0 around which the reactor is perturbed.

As shown in equation (2.19) and equation (2.20), the reactivity, the prompt and the delayed neutron parameters describes these two terms. The time constants associated to the production of prompt and delayed neutrons cause them to be sensitive to different domains of frequency in the Fourier analysis. Several time constants of some typical perturbation sources within LWRs is shown in table 2.1. These constants of different orders of magnitude give rise to differed reactor response as a function of frequency. The amplitude of the ZPTF represents the amplitude of the reactor response with respect to that of the perturbation caused by neutron interactions. The phase indicates the lag between the reactor response and the perturbation.

Table 2.1: Time constants of perturbation phenomena in light water reactors (after [50])

Phenomena	s^{-1}
Delayed neutron effect	10^{-3} - 1
Thermohydraulic effect	0.1 - 10
Prompt neutron effect	1 - 100
Subcooled boiling effect	10 - 3000
Space-dependent effect	1000 - 10^6

Examples of analytical ZPTFs of the CROCUS reactor, which is a ^{235}U fueled and light water moderated reactor, are shown in figure 2.2. The kinetic parameters are taken

from calculated values using respectively the JEFF-3.3 and ENDF/B-VII.1 libraries. The total delayed neutron fraction are respectively 758 pcm and 737 pcm. As illustrated in figure 2.2, the ZPTFs show a distinct behavior of nuclear reactors with different kinetic parameter sets.

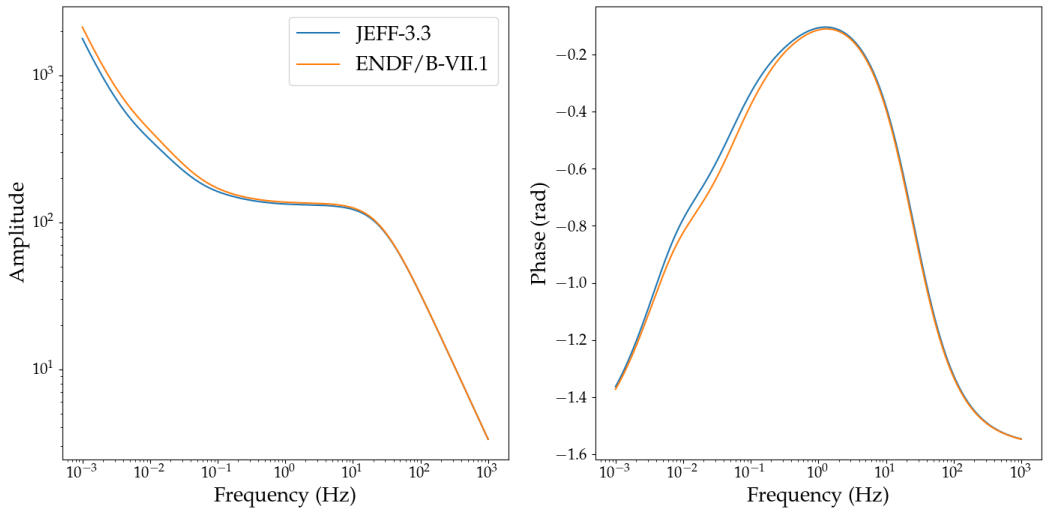

Figure 2.2: Illustration of the amplitude and the phase of the ZPTF of the CROCUS reactor using kinetic parameter values of JEFF-3.3 and ENDF/B-VII.1 libraries

Three frequency ranges could be identified in this frequency response.

- The low frequency range ($\omega \ll \lambda_i$) where the reactor response to perturbation is governed by the kinetics of delayed neutrons (< 0.1 Hz).
- The intermediate frequency range ($\lambda_i \ll \omega \ll \beta_{\text{eff}}/\Lambda$) with a moderate decrease of the amplitude curve. Within this range, the value of $b(\omega)$ is much lower than $a(\omega)$. We have:

$$a(\omega) = -\rho_0 + \sum_i^n \frac{\beta_{\text{eff},i}}{(\lambda_i/\omega)^2 + 1} \approx -\rho_0 + \sum_i^n \beta_{\text{eff},i} \approx \beta_{\text{eff}} - \rho_0 \tag{2.21}$$

$$b(\omega) = \Lambda\omega(1 + \sum_i^n \frac{\beta_{\text{eff},i}/\Lambda}{\lambda_i + \omega^2/\lambda_i}) \approx \Lambda\omega \tag{2.22}$$

  The actual value of Λ, as compared to β is of two orders of magnitude lower. Therefore, the amplitude can be considered to be approximately equal to $1/(\beta_{\text{eff}} - \rho)$.

- The high frequency range ($\omega > \beta_{\text{eff}}/\Lambda$) where the the reactor behavior is essentially governed by the kinetics of prompt neutrons. The approximations equation (2.21) and equation (2.22) remain valid while the contribution of both terms have to be considered, which leads to :

$$|| \, G(j\omega) \, || \approx \frac{1}{\sqrt{(-\rho_0 + \beta_{\text{eff}})^2 + \Lambda^2\omega^2}} \tag{2.23}$$

Equation (2.23) results in an asymptotic decrease of -20 dB per decade of the amplitude response and a phase response approaching $-\frac{\pi}{2}$ rad. The cutoff angular frequency of the amplitude (frequency above which the amplitude is -3 dB lower than the value in the intermediate range) corresponds to $\frac{\rho-\beta_{\text{eff}}}{\Lambda}$, which is referred to as the prompt neutron decay constant α [30].

The phase lag reaching $-\frac{\pi}{2}$ rad with the frequency decrease can be interpreted as the delaying effect of reactor kinetics, as a result of the decay time of the precursors. In the high frequency range, a similar behavior is shown. The delayed neutron precursors are too slow to contribute to the reactor response as compared to prompt neutrons that causes a deficit of the prompt neutron generation by delayed fission [51]. While approaching the intermediate frequency range, an equilibrium between these two phenomena is established, which leads to the phase to approach a maximum towards 0 radian.

2.2.3 Measurement methods of the ZPTF

The measurement of the ZPTF resorts to the study of the relationship between a modulation and the resulting reactor response. In this aspect, it can be measured by branching noise or modulation methods.

The branching process is inherent to the randomness of nuclear reactions. It leads to random fluctuation of the in-core neutron population, and can be considered as a perturbation over the whole frequency range [30]. By contrast, in the modulation method, the neutron flux variation would be induced externally.

The noise method is simple in its implementation as only the instrumentation of neutron detectors is necessary. However, the noise approach becomes extremely time-consuming and complicated when applied to the measurement of low frequency phenomena, which is of greatest interest for the determination of delayed neutron kinetic parameters. The interpretation of noise measurements at frequencies lower than 1 Hz could also be interfered by external noise sources, such as electronic devices, network, vibration etc..

The modulation method, on the contrary, presents higher complexity in the implementation, as it requires adequate instrumentation to generate a perturbation induced modulation. Nevertheless, it is robust to external noise at low frequency, which allows the determination of the ZPTF within hours of experiment.

The experimental procedure of the modulation experiment is different from that of noise analysis methodology [52]. The measurement itself consists in realizing a series of experiments in which the core is modulated periodically at various frequencies. Each experiment allows to determinate the ZPTF at several discrete frequencies (harmonics of the fundamental frequency of the modulation). A sufficiently high modulation amplitude allows to reduce the uncertainties induced by experimental noise sources, including the pile noise. The kinetic parameters are then determined by a non-linear least square fit of the measured ZPTF amplitude and phase.

2.2.4 Determination of the ZPTF by modulation

In a ZPTF measurement by modulation, the raw experimental data consist in a series of detector signal which translates the reactor response that is superimposed to statistical fluctuations due to mechanical or neutron noise.

The introduction of a sine shape reactivity excitation as a function of time is the conventional manner of the ZPTF measurement at a specific frequency. The realization of a sine shape modulation relies on a design of the form of neutronically active materials [46], [53], [54] or a specific motion pattern [55]. Sine shape modulation results in a series of measurements. The number of experiments and duration increase with the experimental data desired. Another type of modulation profile largely studied was the distribution of square-like functions. The modulation consists in the alternation between two reactivity worth of the core. Figure 2.3 shows an example case study conducted using a point kinetic model, with ZPTF estimation by a square-like reactivity modulation. As is observed in the ZPTF amplitude, the square function is composed of a series of odd harmonics, and the even ones are suppressed.

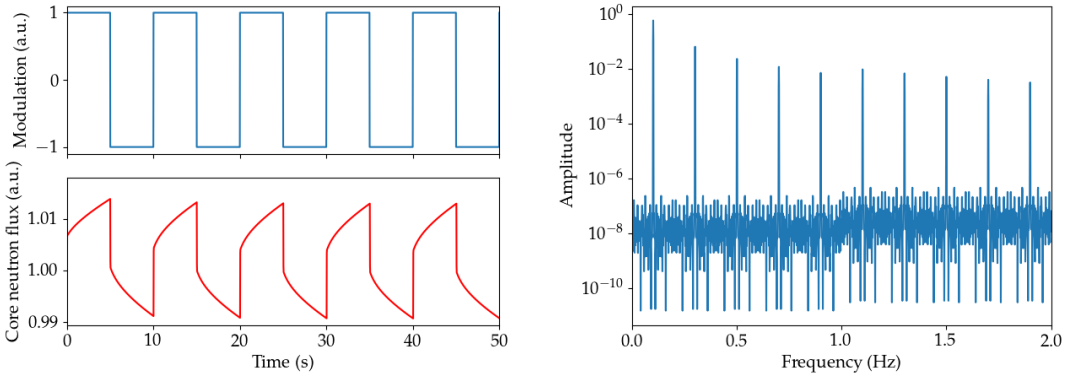

Figure 2.3: Test case of a square shape reactivity modulation (left) and amplitude spectrum (right)

The pseudorandom binary function is a variant of the square function. They consist in a periodic two-level function with length 2^n-1 where n is an integer referred to as "bit". The repeated sequential pattern are generated using deterministic algorithms and the harmonics have distinct phases. This makes the amplitude of the harmonics to not decay rapidly as the case of square function (linear decrease of the amplitude with respect to the order of the harmonic). The frequency domain spectrum of a 5 bit Maximum Length Sequence (MLS) is shown in figure 4.5. The harmonics present a lobe-like structure with a power annihilation at the multiple of $(2^n\text{-}1)^{\text{th}}$. This class of function as modulation signal excites simultaneously the reactor response composed of a large number of harmonics. They therefore appeared to be a pragmatic choice for the implementation of the modulation [56]–[60].

2.3 State-of-the-art of modulation experiments

2.3.1 Overview

Extensive studies of the modulation measurements first appeared in the early years of reactor physics research in the 1950s. The studies were mainly conducted in industrial and high-power research reactors in a low power configuration. They focused on relatively low frequencies between 0.01 Hz and 5 Hz [54], [61], [62] to characterize the reactor stability.

It was possible to use directly the reactivity control system, for instance control rods for modulation studies [8]. However, these systems were not designed for accurate position control. They induced additionally the local flux depletion due to the important capture reaction rate and required to apply spatial effect correction in the PK approximation. In order to relieve these issues, modulators dedicated to modulation experiments were designed to be installed in or close to the reactor core [9], [63]. These systems can be divided into two mechanisms [32]:

- The modulation of the neutron source is produced by the variation of the pulse frequency of source neutron [64], or in some configurations by the variation of source position or intensity [65].
- The reactivity modulation relies on a device having a variable reactivity worth through the change in nuclear reaction rate by motion or material density variation (e.g. heating or compression).

Source modulation experiments were primarily conducted in subcritical systems such as Accelerator-Driven System (ADS), while reactivity modulation were conducted in critical reactor cores. In this study, we limit the discussion to the reactivity modulation systems and its in-core application.

In the 1960s, reactivity modulators with much larger frequencies (up to 260 Hz) as compared to the first prototypes were developed. Some authors [46], [61], [66]–[69] investigated ZPTF measurements for kinetic studies. Their motivation was to determine kinetic parameters of research reactors or to compare the experimental data to an evaluated parameter set. Due to limited calculation resources, the amplitude and phase were often determined with analog electronic systems. The phase uncertainties were typically more than 0.2 rad at frequencies lower than 1 Hz [66], [70]. Limits in acquisition system, electronic equipment and experimental constraints were considered in the uncertainty quantification. [61] reported a consistent 7% discrepancy between measured and predicted ZPTF amplitude below 0.01 Hz. The lack of precise knowledge of $\beta_{\text{eff}}/\Lambda$ also contributed to discrepancies between the experimental results and the analytic ZPTF using previously evaluated kinetic parameter sets.

The aforementioned work were conducted with neutron detectors located out of the core, or sufficiently far from the source of the modulation to maintain the validity of the PK approximation. Another field of study of modulation experiments was the space-dependence of ZPTF and its deviation from the PK behavior [71]–[74]. In this case, multiple detectors were located asymmetrically in the core. Discrepancies were observed between detectors' responses in the measured amplitude and phase. These discrepancies were observed at angular frequencies higher than the prompt decay constant α. Its typical numerical value is approximately 30 rad.s^{-1} for heavy-water or graphite moderated systems and greater than 150 rad.s^{-1} for light water moderated systems [75]. To the author's knowledge, the space-dependent behavior of the ZPTF was only measured within heavy-water moderated systems due to the appearance of spatial effects at comparatively low frequencies than light water moderated system.

During the period between 1980 and 2000, very few modulation studies were found in the literature. It then regained more attention in the 21^{st} century, with several new

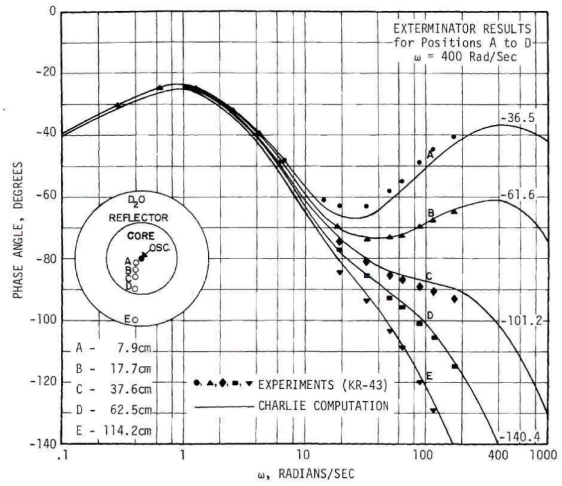

Figure 2.4: Space-dependent Zero-Power Transfer Function phase measured in the NORA reactor [72]

modulation experiments in ZPRs conducted for the determination of kinetic parameters [37], [76]–[79]. The motivation of these studies were the measurement of delayed neutron parameters for comparison with library-dependent calculations. As a consequence, the frequency range of the modulation were reduced to as low as 0.002 Hz. Technological developments also allowed the construction of novel modulation systems [77], [80], [81] for studies that focused on spatial effects and noise propagation.

2.3.2 Reactivity modulator concepts

Most of the developed modulation mechanisms were motion-based, due to their relatively simple manufacturing. The modulation was produced by a geometrical or compositional asymmetry of the modulator during the motion with respect to the reactor core configuration, as in the case of an axially moving control rod in reactors with using rod-formed fuels. The azimuthal asymmetry was also used for rotary modulator design. Several examples of existing rotary modulator geometries are shown in figure 2.5.

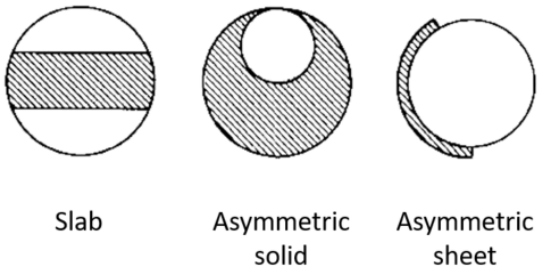

Figure 2.5: Geometry examples of rotary modulators

Another concept of modulation did not rely on the asymmetry, but rather on a coupling of two neutron absorber layers (a static and a moving one) with a variable absorption reaction rate induced by the motion [53]. While the two layers are close to each other,

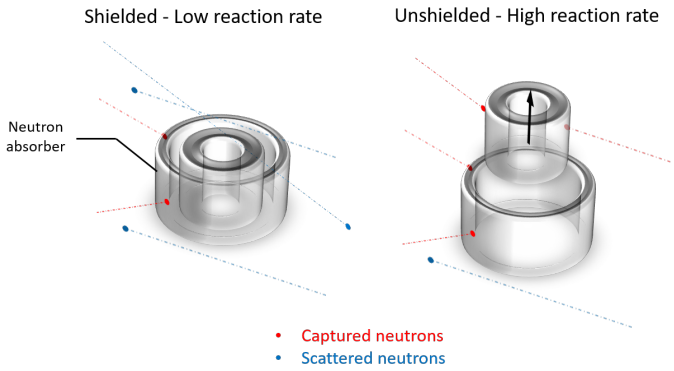

Figure 2.6: Comparison of capture reaction rate in shielded and unshielded configurations

the anti-reactivity is minimized due to the local flux depletion while the anti-reactivity increases progressively during the separation of the two layers. Compared to the asymmetrical design, the self-shielded design offers more flexibility in the system scaling and the motion control [46], as an asymmetrical system requires larger motion range or system size to reach the same modulation amplitude as in the self-shielded case.

Characteristics of some rotary modulators which were instrumented in research reactors are summarized in table 2.2. It can be seen that the self-shielded design was commonly adopted in light water research reactors. For the effective generation of the modulation in fast reactors, it is common practice to use a moderator material to first thermalize the fast neutrons and absorb neutrons using a poison. The use of fissile material would also be an option within the limit of availability. For a thermal reactor, the coupling of a moderator and poison material is a much more available and technologically viable choice.

Alternative modulator concepts to motion-based systems, such as temperature or pressure dependent systems were also addressed in the literature. Some of them relied on the specific features of the reactor involved in experimental studies. For pool-type reactors, systems varying the in-core water content were conceived [82], [83]. The induced reactivity variation was related to the moderation and reflection reaction rates. In [84], a boiling water loop with variable flow rate and void fraction was built, and tested out-of-pile. It was suggested by [85]–[87] that magnetic fields and laser lights that could act on the absorption cross section of ^{3}He atoms by spin polarization. However, no applied experimental studies were found in the field of reactor physics.

Table 2.2: Summary of the characteristics of rotary rod modulators in past experimental studies

Material	Geometry	Reactor	Reactor type	Power	Frequency range (Hz)
B_4C + Na	Asymmetric	Enrico Fermi [61]	SFR[1]	∼0 W	0.001-10
Boral poision	Self-shielded	SRE [88]	SFR	∼0 W	0.05-20
Cd+H_2O	Self-shielded	KEWB [66]	U235 solution fuel	∼0 W	1-260
Enriched and natural Uranium	Asymmetric	Zephyr [62]	Fast zero power	∼0 W	0.002-3
Cd+H2O/Cd+U	Self-shielded	SPERT-I-B [46]	LWR[4]	1 kW	0.002-18.4
Cd	Self-shielded	LPTR [70]	Thermal LWR	Subcritical[2]	0.005-150
		GTRR [72]	HWR	∼0 W	0.1-40
Cd+PE[3]	Asymmetric	OSURR [69]	MTR[5]	1 kW	0.013-60

2.4 Chapter summary

This chapter introduced basic notions and parameters of the reactor kinetics within the point kinetic approximation, and the zero-power reactor transfer function which is also formulated within this approximation. The theoretical model of the ZPTF is defined as a function of the effective prompt and delayed neutron kinetics parameters (Λ,$\beta_{\text{eff,i}}$,λ_i) and the static reactivity ρ. Therefore, the ZPTF is considered as an integral observable of the kinetic parameters. In the literature, modulation experiments were conducted for the measurements of the ZPTF with the development of modulation devices. The survey in the literature gives some insights of the possible options in the design of the modulator for the current work.

[1]Sodium Fast Reactor
[2]Critical with photoneutron source
[3]Polyethylene
[4]Light Water Reactor
[5]Material Testing Reactor

Chapter 3

Development of a Reactivity Modulator

This chapter synthesizes the design and development of a reactivity modulator that was tested in the zero-power research reactor CROCUS, which is a reactor with well-known characteristics and easy access. We first outline the design considerations of the developed reactivity modulator. The input parameters for the design of the modulator are then introduced. The result of the design studies allowed the manufacturing of the so-called PISTIL device. The technical details of the device is also presented.

3.1 Zero-power research reactor CROCUS

3.1.1 Reference reactor configuration

The CROCUS reactor is a zero-power research reactor operated by the Laboratory of reactor physics and system behavior at EPFL. It is a pool-type zero-power research reactor

moderated by light water (H_2O) regulated at 20.00 ± 0.01 °C by a controlled water loop. Detailed descriptions regarding the geometry and material composition of the reactor elements are documented in the CROCUS kinetic benchmark [1]. The reactor is in a concrete shielded cavity. The core is located in an aluminum vessel of 1.3 m in diameter and 1.45 m in height. A PuBe neutron source is located under the vessel for the reactor start-up. The fuel area of the reactor has approximately a cylindrical form with a diameter of 60 cm and 1 m in height. It consists of an inner zone with 336 UO_2 fuel rods of 1.806 wt.% enrichment, and an outer zone of 176 U_{met} fuel rods of 0.947 wt.% enrichment. These two zones are separated by a water gap, and have respectively a square lattice pitch of 1.837 cm and 2.917 cm. The fuel rods are maintained vertical by the upper and lower grid plates, and are in contact with the base plate of the reactor at the lower end. The axial dimensions of the fuel rods and the plates are indicated in figure 3.1.

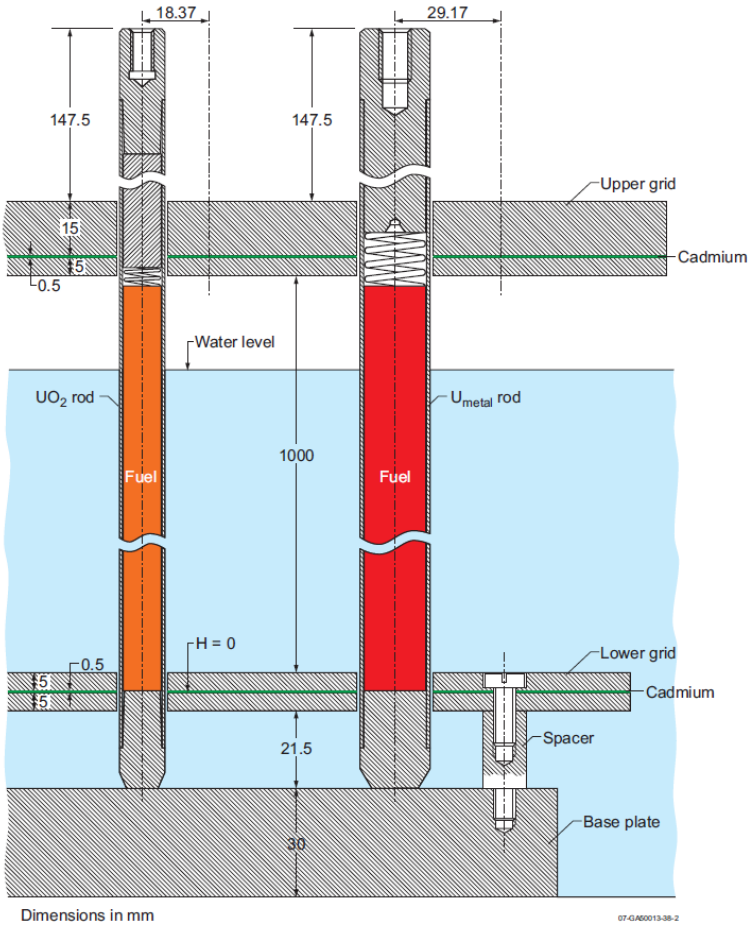

Figure 3.1: Axial configuration of the fuel rods and the grid plates [1]

Figure 3.2 shows a cross sectional view of the reactor core and associated structure in its reference configuration. In the conducted experiments, the COLIBRI configuration was used: the COLIBRI fuel rods oscillator allows the displacement and oscillation of 18 Umet rods. For the considered experiments, the COLIBRI rods were set in their nominal position within the U_{met} lattice, i.e. equivalent to the reference configuration. The main

difference lies in the upper and lower grids which contains a cadmium layer of 1 mm thickness instead of 0.5 mm.

As compared to the reference benchmark configuration [1], CROCUS was set in the COLIBRI oscillator configuration [81] in this work. The oscillator rods were maintained at their nominal positions within the regular U_{met} fuel lattice.

3.1.2 Reactor operation and monitoring

The reactor is operated by either varying the core water level with a spillway (accuracy of $\pm$ 0.1 mm) or by moving two B_4C control rods (accuracy of $\pm$ 0.5 mm). The maximum authorized thermal power of the reactor is 100 W. Six independent safety systems, including two cruciform cadmium blades and four expansion tanks, are activated when the core doubling time becomes lower than 9 s or when the signals from safety monitors are lost.

CROCUS is instrumented with two compensated ionization chambers as neutron flux monitors during operation in the north and the south of the core. Two additional Photonis CFUM21 Fission Chamber (FC) were used as calibrated reactor power monitors. The location of these detectors are illustrated in figure 3.2.

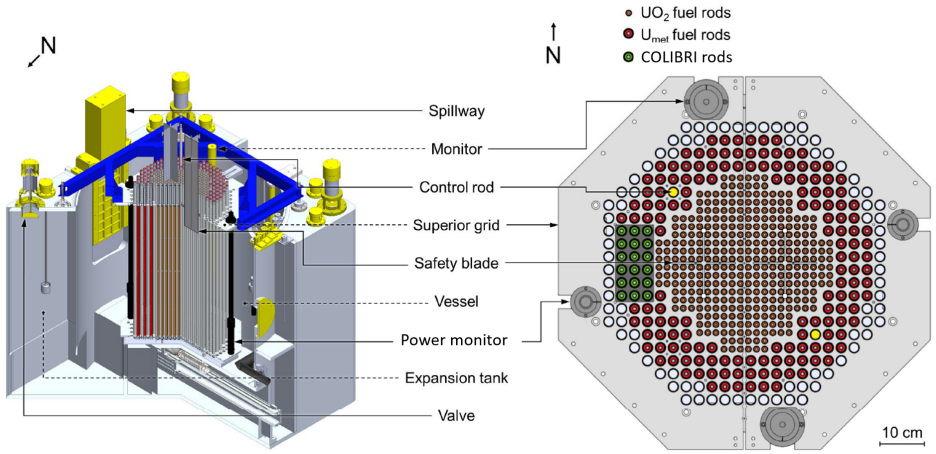

Figure 3.2: Cross sectional view of the CROCUS core and reactor structure in the COLIBRI configuration (after [31])

3.2 Design of the reactivity modulator

The design of the reactivity modulator relies on the knowledge of geometrical and material of the reactor components. This helps the identification of the design inputs: constraints related to the reactor operation, performance requirements and concerns regarding the material.

3.2.1 Experimental constraints

The installation of a reactivity modulator necessarily impacts the core configuration with respect to the reference one from neutronic and mechanical point of view. Therefore, the

licensing of a modulator in CROCUS is subject to the authorization of the Swiss nuclear regulatory body: the Swiss Federal Nuclear Safety Inspectorate (ENSI/IFSN). Several criteria have to be satisfied, which influenced the modulator design to a great extent. The major criteria are briefly summarized here:

- The chemical interaction between an experimental device and the demineralized water filled in the reactor vessel is prohibited. For safety concerns, the mechanical integrity of the experimental systems has also to be qualified through ex-core and in-core tests.

- The compactness of the CROCUS fuel zone and the presence of the grid plates limits the dimension of experimental devices and detectors to be introduced. An accessible position of 10 mm diameter is located in the core center, as well as one empty guide tube in the U_{met} lattice of 19.3 mm diameter (shown in figure 3.14) that can be used or removed for experimental purposes. Additionally, a series of extra holes of 19.3 mm diameter in the grid in the core periphery allow the positioning of experimental channels.

- During the operation of the reactor, the heat generation, pressure variation and motion induced vibration should be contained within the device and have limited impact on the reactor operation. Any transmission of these physical impact towards the fuel elements is prohibited.

- In the current configuration of CROCUS, the reference critical water level is about 950 mm. The maximum water level is 990 mm instead of 1000 mm to avoid the flooding of detector electronics. In CROCUS, an increase of 1 mm in the water level corresponds to a reactivity insertion of 4 pcm, which indicates a maximum available reactivity reserve of 160 pcm. This value is also the limit for the total reactivity worth of in-core experimental devices and detectors.

3.2.2 Performance requirements

In addition to the criteria mentioned in section 3.2.1, several performance specifications of the modulator were identified as well.

The modulation frequency, as closely related to the kinetics of prompt and delayed neutrons, should cover the range of their characteristic time constants. The longest half-life of precursor groups in the calculated kinetic parameters in CROCUS [89] is 55.6 s (corresponding to ^{87}Br according to JEFF-3.3 [11]). In order to obtain useful information of the kinetics of this group, the modulation frequency should be much lower (at least 10 times) than 0.01247 Hz (the frequency corresponding to its decay constant value). Calculated and previously measured prompt decay constant values were approximately 150 rad.s^{-1} [39], [89], [90], which corresponds to a frequency of 23.9 Hz. For the determination of the decay constant and the generation time, it is required to measure the ZPTF from frequencies lower than this value till an order higher of it. An extension of the measurable

frequency range is advantageous. To broaden the frequency range of modulation, the literature suggested the introduction of a geometrical symmetry with respect to the motion, known as sectorization. In such a manner, the modulation frequency becomes a multiple of the motion frequency to overcome the mechanical limits of the motor.

The aimed modulation amplitude is in the range of 5 to 10 pcm (about 1 ¢) to maintain the validity of the small perturbation approximation. The studies related to the estimation of this amplitude value is discussed in section 4.1. The numerical value is in accordance with previous modulation experiments [37], [76], [91] for ZPTF measurement in the derivation of the ZPTF model ($\sim$ 0.5 ¢) .

Multiple types of modulation options were identified in the literature, such as sine, triangular, square shape-like reactivity variation. It was preferred that the modulator has the capacity to generate multiple modulation shape function. This allows the intercomparison of measurements obtained using different modulation as a means of consistency verification.

The details of the implemented design is discussed in chapter 4.

3.2.3 Material selection and mechanical factors

Fissile material, moderator, reflector and absorber were all studied options to induce the reactivity modulation. The fissile materials were not considered in the present study due to difficulty in its manufacturing, storage and transport. As for the others, common dosimetry materials (In, Au, Ag, H_2O...) with well-known nuclear data were privileged. A substantial concern was whether the material can be conveniently machined.

Apart from the neutronically active elements, the modulator requires a number of structural components for the assembling and manufacturing. Aluminum and stainless steel (SS) appeared to be the most prominent candidate material for their good mechanical properties and high precision industrial processing methods available. A watertight cylindrical tube of 10 mm diameter and 100 mm in height was modeled to evaluate the overall reactivity effect of the modulator installed in the core center of CROCUS, compared to the aluminum tube, stainless steel structure induces an additional reactivity worth of -50 pcm as estimated by Monte Carlo calculation (the modeling will be discussed in section 3.2.5). In addition, isotopes present in SS have significantly higher neutron activation than aluminum which is nearly transparent to neutrons. Therefore, aluminum was privileged as the structural material.

3.2.4 Design studies

Mechanical vibrations induced by the motion transmission mechanism were of primary concern throughout the studies of the mechanical design of the modulator.

Linear motors offer precise positioning in a forward-backward motion, are indeed compatible with the aforementioned performance requirement. However, their risks of malfunction and accident are much higher as compared to rotary motors. as the available space in CROCUS has negligible radial dimension ($<$ 20 mm) with respect to the axial dimension (1000 mm). The generation of high speed stroke of a long shaft has higher mechanical impact in comparison to the rotation of an axis with a small diameter. The

concept to be studied was determined as the self-shielded rotary modulator. The concept is the most consistent one with respect to the experimental constraints of geometry.

The studies in the literature also led to favor the self-shielded modulator concept discussed in section 2.3.2. Facility and experimental constraints in CROCUS identified in section 3.2.1 and the required modulator performance criteria were consistent with this concept as well.

The design consists in two aspects: a neutronic modeling allows to establish a conceptual design of the modulator and a mechanical one that define the actual dimensions and material of the device to be manufactured. We briefly discuss the design process of the newly developed experimental device Periodic reactivity Injection System Transient Induced Locally (PISTIL).

3.2.5 Neutronic modeling methodology of PISTIL

For the design of PISTIL, the parameters of concern were the overall reactivity worth of the device, the profile of the reactivity modulation (i.e. differential reactivity) with respect to the angular position and the amplitude. The modulation equivalent to the perturbation which is the variation of the angular position for a rotary system. The aim of the design study was to examine the potential of the material combination to achieve an optimal length and weight. It was desired to limit the weight of the device to reduce the mechanical torque required.

The reactivity estimation of the time-dependent neutron transport problem was recently implemented in the Monte Carlo code TRIPOLI-4® [92] and deterministic code APOLLO3® [93]. Nevertheless, these methods were not compatible with the requirement of the design with respect to the accuracy of the reactivity calculation. The kinetic module of TRIPOLI-4, at its current stage of development, needs a significant time in computation (more than 1000 CPU hours) for a convergence of ± 8 pcm on simple models [92]. On the other hand, the kinetic APOLLO3 calculation can only give a estimation of the reactivity worth and amplitude on a relative reactivity scale.

Materials of various geometries were considered in the design studies, and their neutronic effects such as the modulation amplitude and the reactivity worth were estimated by virtue of a series of static neutronic simulations with TRIPOLI-4® (in criticality mode) and APOLLO3® codes. In these simulations, the configuration of the reactor remains the same, and the only variability is the angular position of the rotor of PISTIL with respect to the core.

The differential reactivity is defined as the reactivity difference between two states of the motion (e.g. angular position in rotation). At two states 1 and 2, the differential reactivity in simulation $\delta\rho_{1,2}$ is equal to:

$$\delta\rho_{1,2} = \frac{1}{k_{\text{eff},2}} - \frac{1}{k_{\text{eff},1}} \tag{3.1}$$

where $k_{\text{eff},1}$ and $k_{\text{eff},2}$ are respectively the k_{eff} tally in the static simulation with the modeling of state 1 and 2.

A case study of the combination of materials as well as the corresponding geometries requires at least two simulations of the modulator in a (theoretical) maximum and minimum reactivity states using equation (3.1) to estimate the modulation amplitude.

In order to efficiently perform the design study, a combined approach of Monte Carlo and deterministic calculations, using respectively TRIPOLI-4® and APOLLO3®. As an indication, one simulation of the full core of CROCUS (modulator included) with 10^9 neutron histories requires approximately 15000 CPU hours to reach an uncertainty of $\pm$ 3 pcm, which is excessive when various materials have to be tested. Three types of simulations were conducted to select the modulator design and characterize its reactivity profile.

A simplified model in TRIPOLI-4 calculation, which is a 8 x 8 square fuel lattice geometry is shown in figure 3.3. The rods are loaded with the central UO_2 fuel rods of CROCUS. The geometry is considered representative of the neutron spectrum in the core center. The modulation device was modeled at the center of the fuel lattice.

For simplification, the geometry was considered as an infinite medium, because the neutron spectrum at the boundary was not affected by the increase of the lattice size or the geometry variation of the modulator. The axial dimension of the modulator was set to 50 cm (half of the height of the fissile material) and at mid-height of the core to evaluate the effectiveness of reactivity modulation of different material composition. The calculated reactivity worth was amplified by the size of the moderator and the diminution of the reactor dimension for faster convergence.

In order to convert the reactivity worth of the modulator of 50 cm length to the one in the full core of CROCUS a multiplication factor was applied. It consisted in the ratio of the integral capture Reaction Rate (RR) between two reference calculations of the device in the simplified model and the full-core model.

$$\delta\rho^{*}_{1,2} = \delta\rho^{'}_{1,2} \cdot \frac{RR^{*}_{\text{capture}}}{RR^{'}_{\text{capture}}} \tag{3.2}$$

where * is the full core configuration and $^{'}$ is the reduced-scale configuration.

The simulation approach described above gave an estimation of the geometry of the device, and the selection of the materials.

It was also essential to estimate the reactivity variation with respect to the angular position of the device. An *a priori* knowledge of the relationship between the reactivity and the position allow to design the experiments in accordance with the harmonic components of the modulation in the frequency domain. TRIPOLI-4 calculations were not used to obtain the reactivity profile, because excessive computation time is required to reach a sufficiently low uncertainty in the results. Complementary 3D deterministic calculations using APOLLO3 were performed, which consisted in calculating the differential reactivity with a fine angular discretization (about 1° in rotation). The method of characteristic solver (3D TDT-MOC) [94] with a 281-group energy discretization is used for this calculation.

The determined design is described in section 3.2.6 . For the determination of the actual geometry of the device, the modeling of the modulator within the full core model of CROCUS was conducted using TRIPOLI-4 calculation. This gave a precise estimation of the total reactivity worth as well as the maximum differential reactivity of the device.

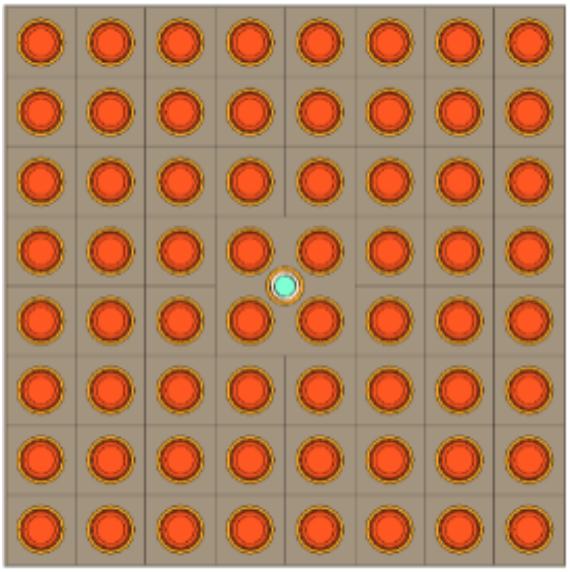

Figure 3.3: Geometry of the simplified model of CROCUS with the modulator modeled in the center of the 8 x 8 lattice

3.2.6 Selection of materials

The reactivity effect of self-shielded modulator design relies on the high capture reaction rate of an outer absorber material that screens out the thermal neutrons interacting with an inner layer, when the two of them are nested.

A large number of material combinations were tested. One key parameter was the static reactivity worth of the material. For the divergence of the reactor, the maximum reactivity worth of the modulator should not exceed -160 pcm. It was favored that the maximum differential reactivity to be as high as possible as compared to the static worth, so that the 5-10 pcm modulation can be achieved.

A summary of the order of magnitude of the modulation effect of some well-known materials is shown in table 3.1. It was observed that the static reactivity worth of the materials was significant as compared to the maximum differential reactivity. The coupling of gadolinium and gold as a two layer structure modeled on the stator and the rotor was motivated by the fact that the most prominent resonances in their respective capture reactions are located at different energies, consequently it was considered possible that they have efficient screen effect and the modulation amplitude. This was however not the case from the simulation results. Furthermore, the coupling cause an increase of the static reactivity worth, which is undesired. This can be understood from the order of magnitude of the cross section of (n,γ) reaction shown in figure 3.4. The capture reaction rate of gadolinium below 0.1 eV is so important so that the modulation effect within the energy range of the resonances is limited.

Figure 3.5 illustrates the distribution of the calculated capture reaction rates and neutron spectrum within a cadmium rotor element covered and uncovered by the stator of identical composition. It can be understood that the contribution of resonances in the

[6]Two sub-layers of gadolinium and gold of 0.25 mm thickness

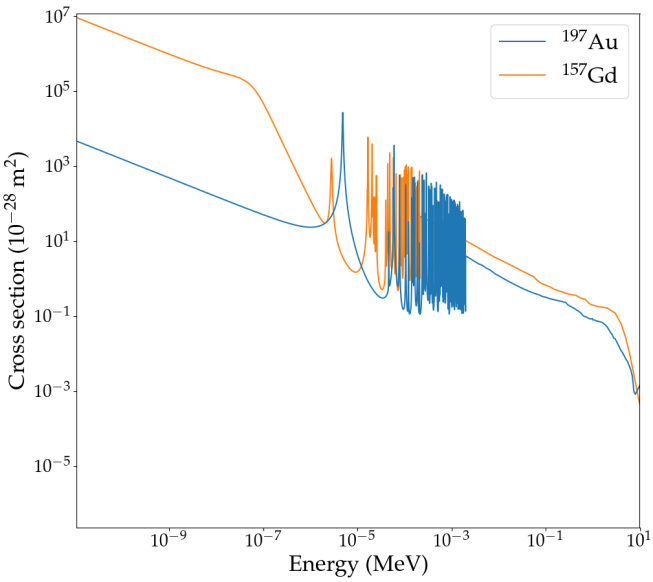

Figure 3.4: Microscopic cross sections of (n,γ) reaction for ^{197}Au and ^{157}Gd isotopes

Table 3.1: Estimated reactivity effects of modulators of 50 cm length in the full core of CROCUS using TRIPOLI-4 calculations

Material	Thickness (mm)	Outer/Inner diameter (mm)	Static worth (pcm)	Maximum differential reactivity (pcm)	Relative amplitude (%)
Cd	0.5	5/4	518.8 ± 2.1	24.5 ± 1.9	4.7
Gd			586.2 ± 2.5	26.2 ± 2.0	4.5
Au			483.3 ± 1.2	19.6 ± 1.8	4.1
Ag			276.1 ± 0.6	9.5 ± 0.9	3.1
B_4C			581.9 ± 0.8	47.5 ± 1.2	8.2
Gd+Au[6]			648.7 ± 3.0	17.8 ± 1.1	2.7

epithermal energy range is limited as compared to the total capture reaction rate. The majority of the captured neutrons are thermal. For this reason effective enhancement of the modulation amplitude was not reached by a coupling of two absorbers such as the Gd/Au combination in table 3.1.

The amplitude enhancement was the key factor in the design. The much higher reactivity modulation performance of B_4C gave an insight on the interest in coupling a neutron absorber (^{10}B) and a moderator material (^{12}C) that increases the ^{10}B (n,α) ^{7}Li reaction rate by a local moderation of neutrons. However, the machining of B_4C to a desired shape is too complicated to be considered for the miniaturization of the device. Therefore, it is not investigated in the studies detailed hereafter.

Various other coupling principles between absorber (Cd, Gd, In, Au, Ag), moderator and reflector (H_2O, CH_4,Be) were tested. General conclusions drawn from these tests are shown in table 3.2, the relative amplitudes were compared to values in table 3.1 when the rotor and stator were made of the same absorber material involved.

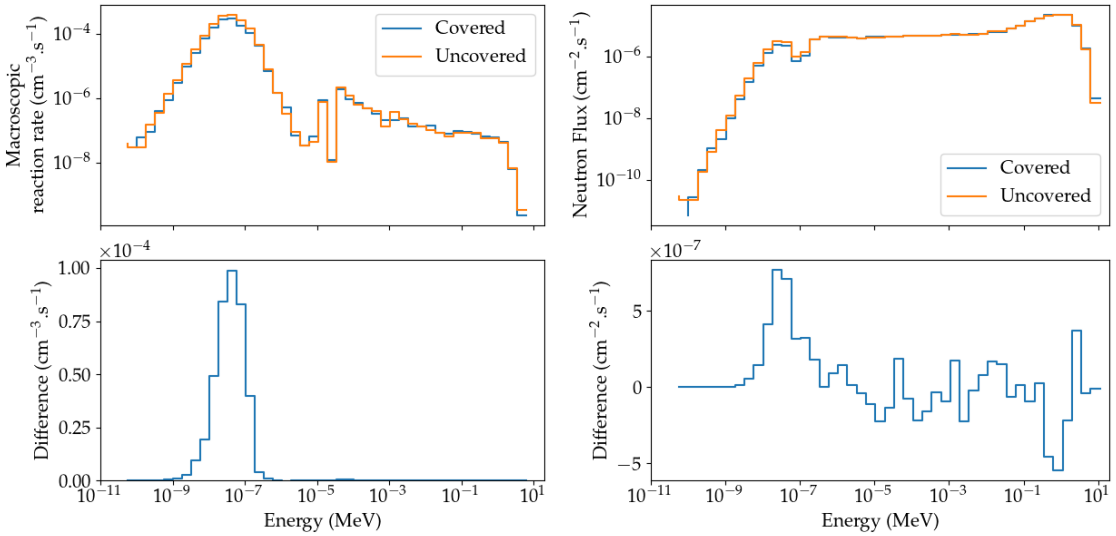

Figure 3.5: Calculated (n,γ) reaction rates (left) and neutron spectrum (right) in a cadmium rotor element in covered and uncovered configurations, values normalized to the fission rate

Table 3.2: Summary of reactivity modulation effects by the combination of multiple materials

Case	Position	Concept	Typical Material	Relative amplitude
1	Stator Rotor	absorbers absorbers	Cd/Au	-43.1%
2	Stator Rotor	absorber/moderator absorber/moderator	Cd+PE Cd	+6.5%
3	Stator Rotor	absorber absorber/reflector	Cd Cd/Plexiglas	+7.1%
4	Stator Rotor Center	absorber absorber Moderator	Cd Cd PE	+15.4%

The geometrical symmetry by sectorization, as illustrated in figure 3.6, allows to increase the frequency of reactivity modulation with respect to the rotation. This feature allows to reduce the maximum speed of the rotation required for the experiments to reduce the mechanical risks.

Table 3.3 shows the reactivity worth of the same mass of cadmium on rotor, but with different sectorization. The static reactivity worth of the modulator increases with the number of sectors, due to the decrease of shielding effect. Additionally, in practice a high level sectorization leads to complication in the accurate machining and assembling, which lessen its attractiveness. It was also observed in table 3.3 that sectorizing the modulator with an octant symmetry results in a drop of the modulation amplitude, possibly due to a decrease of the effectiveness of screening of the stator on the rotor as the dimensions

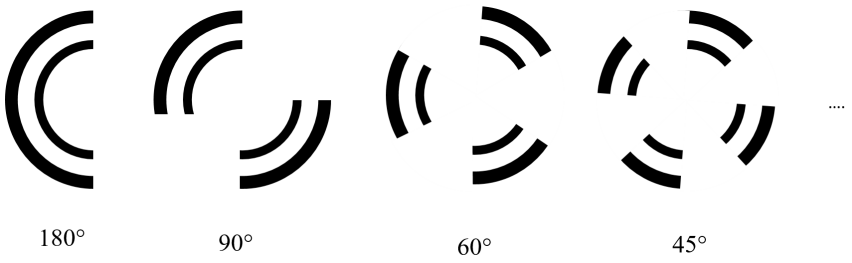

Figure 3.6: Sectorized rotor-stator geometries

of the sectors are limited. The quadrant geometry (90° sectors) appeared to be a trade-off between the antagonistic needs in reactivity effects and mechanical aspects of the realization.

Table 3.3: Reactivity impact of a sectorized cadmium modulator design

Sectorization	Static worth (pcm)	Modulation difference (pcm)	Relative amplitude (%)
180°	518.8 ± 1.7	24.5 ± 2.1	4.7
90°	540.5 ± 1.8	30.0 ± 1.9	5.5
60°	544.1 ± 1.8	26.5 ± 1.7	4.9
45°	550.6 ± 1.6	23.9 ± 1.3	4.3

3.2.7 Main design conclusion

Considering different elements of the aforementioned design studies, the conceptual model of PISTIL developed is shown in figure 3.7. Cadmium and gadolinium were identified as the better candidate for the rotor and the stator material. Cadmium was selected for its better mechanical characteristics in manufacturing. An additional polyethylene (PE) element was included in the center of the rotor (case 4 in table 3.2). The presence of PE strengthens the modulation effect of about 15% of the reactivity worth thanks to the local moderation of the neutrons. In addition, a two-fold rotary symmetry (i.e. sectors of 90° segments) was adopted. In order to limit the overall reactivity worth of the modulator, the axial length of the neutronically active elements was reduced to 10 cm compared to the simplified simulation models. The rotor-stator assembly was located in a watertight tube in aluminum. When the cadmium strips are covered as shown in figure 3.7, the overall reactivity effect is minimized. In contrast, a 90° rotation brings the device to its maximum reactivity effect.

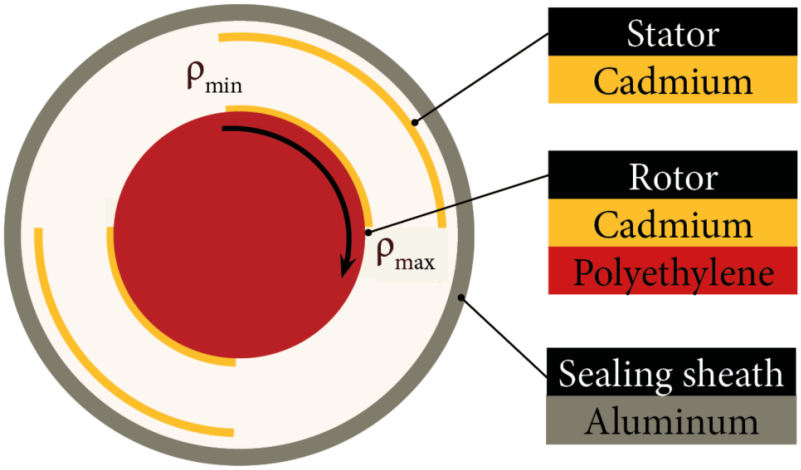

Figure 3.7: Neutronic design of PISTIL

3.3 The PISTIL Device

The manufacturing of PISTIL and the electronics associated to the motion control were completed in the framework of a subcontract. In this section we give a description of the technical details of the components of the device, its mechanical design, the motion control mechanism and the data communication scheme.

3.3.1 Main components of PISTIL

The mechanical assembly of PISTIL consists of five sub-assemblies: the clad, the stator, the guide tube, the rotor and the support structure. Figure 3.8a is a general plan of the components. Their dimensional and material information are summarized in table 3.4. The clad is made of an aluminum-alloy (96.8-99% Al). It has an outer diameter (OD) of 10 mm and a thickness of 0.45 mm. The outer surface was anodized to reduce possible friction at the contact interface of the device with the two grid plates of CROCUS. Its lower end is screwed to a HDPE 500 (High Density PolyEthylene) end-piece (shown in the lower part of figure 3.8a), whose geometry was adapted to fit in the hole of 10 mm diameter in the lower grid plats in the geometry of the COLIBRI configuration of CROCUS [81], [95]. The cap can be replaced for other grid plate openings.

Table 3.4: Dimensional and material details of the principal components of PISTIL

Component	Material	Weight (g)	OD (mm)	ID(mm)	Length (mm)
Clad	Alu 3003 H14	40.74	$10.00\ ^{+0.02}_{-0.02}$	$9.05\ ^{+0.02}_{-0.02}$ 0.02	1000.0 ± 0.1
Stator tube	Alu 2017	4	$8.7^{+0.02}_{-0.02}$	$7.8^{+0.02}_{-0.02}$	104.0 ± 0.1
Stator axis	Alu 2017	20.8	$5.98^{+0.02}_{-0.02}$	$5.1^{+0.02}_{-0.02}$	871.0 ± 0.1
Guide tube	Alu 2017	3.5	$7.60\ ^{+0.02}_{-0.02}$	$6.60\ ^{+0.02}_{-0.02}$	112.0 ± 0.1
Guide axis	Alu 2017	13.7	$3.98\ ^{+0.02}_{-0.02}$	$3.10^{+0.02}_{-0.02}$	1000.0 ± 0.1
Rotor tube	Alu 2017	2.24	$6.40^{+0.02}_{-0.02}$	$5.4^{+0.02}_{-0.02}$	100.0 ± 0.1
Rotor axis	INOX 304	15.05	$1.50^{0.00}_{-0.01}$	-	1055.0 ± 0.5
HDPE	HDPE 500	2.24 ± 0.01	$5.40^{0.00}_{-0.02}$	-	100.0 ± 0.1
Stator strip 1	Cd	0.686 ± 0.001	-	8.40 ± 0.02	100.0 ± 0.1
Stator strip 2	Cd	0.680 ± 0.001	-		100.0 ± 0.1
Rotor strip 1	Cd	0.455 ± 0.001	5.70 ± 0.02	-	100.0 ± 0.1
Rotor strip 2	Cd	0.455 ± 0.001		-	100.0 ± 0.1

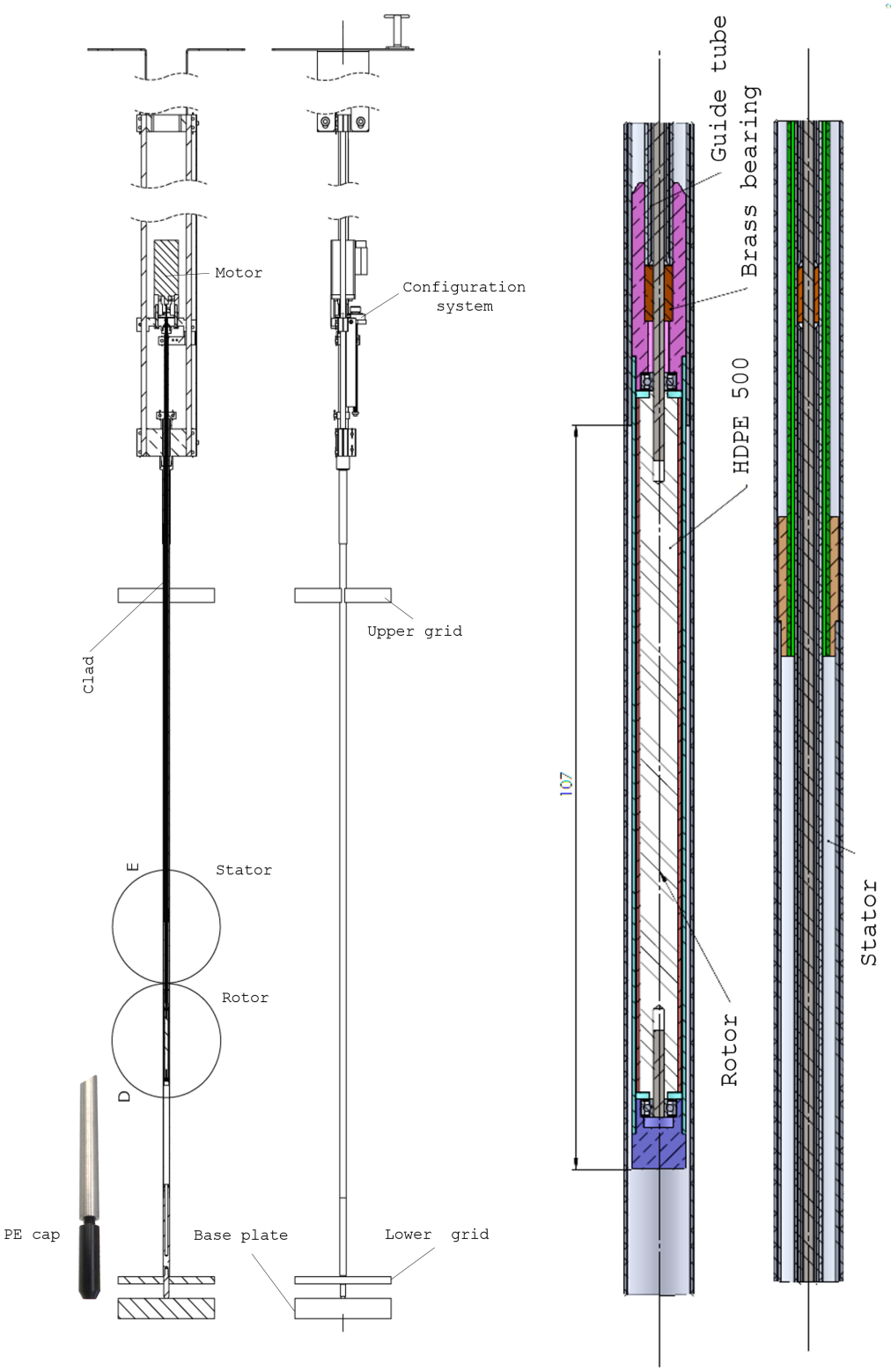

(a) General plan (b) Plan of the rotor and stator

Figure 3.8: Plans of the mechanical design of PISTIL

The stator, guide tube and rotor are nested inside the clad. A detailed plan of the positioning of the tubes is given in figure 3.8b. As shown in figure 3.9, which is a photo of the tubes after disassembling, they are all composed of a long axis of reduced diameter and an enlarged section to hold the cadmium strips and the HDPE cylinder of 10 cm length or to ensure the stability of the rotation. The stator and the guide tube are entirely made of aluminum-alloy (91.65-95.15% Al). On the lower end, their diameter are enlarged to hold two cadmium 90° strips and the rotation bearing respectively. The rotor is a stainless steel shaft soldered to an aluminum-alloy element holding other two cadmium 90° strips. The stainless steel shaft ensures the mechanical resistance at high rotation frequency. The gap between the guide tube and the rotor are reduced to 0.1 mm thanks to miniature rotation bearings. Drawings of the rotor and stator assemblies can be found in Appendix chapter G.

Two recesses of 0.30 ± 0.02 mm and 100.0 ± 0.1 mm length were machined on the outer surface of the stator tube and the inner surface of the rotor tube. The shaped cadmium strips were mounted inside the recesses. The HDPE cylinder (0.96 g.cm^{-3}) was inserted inside the rotor. The dimensions and weights of these items are shown in the lower part table 3.4. As indicated in the table, the OD and ID of the cadmium elements after the mounting were not directly measured: one of them was determined by the dimension of the contact surface of the recesses and the other one was estimated from the weight measurement of 0.001 g precision.

When PISTIL is held vertically, the support structure extends upward to bear a motor, a configuration system of the axial position and angle brackets as indicated in figure 3.9, which allows to attach the device to the structure of CROCUS.

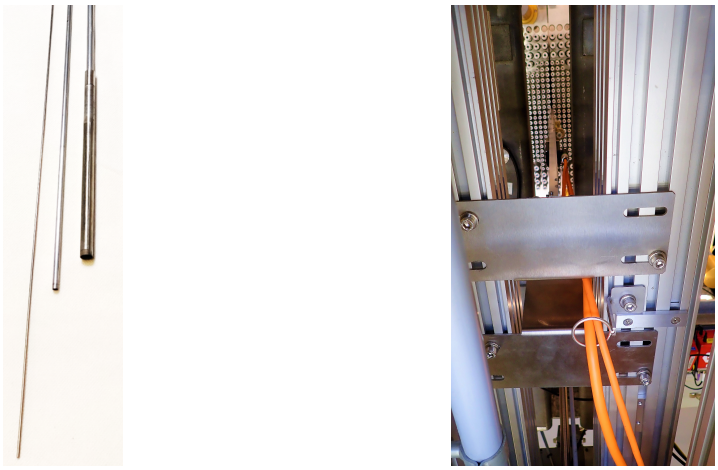

Figure 3.9: Components of PISTIL after disassemblement and angular brackets on top of PISTIL fixed to structural beams of CROCUS and the power cable of the brushless motor (right)

3.3.2 Motion control

The motion of PISTIL's rotor is driven by a TGS1 brushless motor with a nominal speed of 6000 Revolutions Per Minute (rpm). The motion is regulated by a 230 V AC INFRANOR

XtrapulsePac motion controller. The motion commands can be customized using the *TRIO Basic* language: the written programs are communicated from a host computer to the controller by a Numerical Control (NC) TrioMotion Flex-6-Nano P600. The NC executes in parallel 6 processes in loop structure to respond to user commands either from a User Interface (UI) or command line codes. Listing 3.1 shows an example of an infinite loop executing an iteration each 5 ms (`WA(5)`) to initiate the clockwise rotation (`FORWARD`), stop the motion (`CANCEL`) or update motion parameters by the sub-process (`speed_accel`). The accessible commands of the NC are documented in [96].

Listing 3.1: Sample loop structure in TRIO Basic for constant speed rotation commands

```
WHILE(TRUE)
    WA(5)
    '================================================
    'Continuous rotation"
    '================================================
    IF VR(mode) = 1 AND IN(b_marche)=ON THEN
        IF IN(bp_dcy)=ON AND VR(duree_tempo_cont)= 0 THEN 'If total time
            not set

            OP(bp_dcy,OFF)
            GOSUB speed_accel
            FORWARD AXIS(axe) : PRINT #pv5, "Launch continuous rotation (
                indefinite time)"
            WHILE IN(bp_stop)=0 AND IN(b_marche)=ON
                WA(100)'P_GAIN AXIS(axe)=2
            WEND
            CANCEL(2) AXIS(axe)
            OP(bp_stop,OFF)
            PRINT #pv5, ">>> Motion ended"

speed_accel:
SPEED AXIS(axe) = VR(vitesse_axe)
ACCEL AXIS(axe) = VR(accel_axe)
DECEL AXIS(axe) = ACCEL AXIS(axe)
WA(5)

RETURN
```

Two types of two motion instructions are currently programmed for PISTIL.

1. Continuous rotation: The rotor is animated by a constant speed motion ranging from $1°.s^{-1}$ to $36000°.s^{-1}$, which is the nominal speed of PISTIL's motor.

2. Step-wise motion: The rotor follows a predefined sequence of angular position with respect to time. The current implementation allows PISTIL to read tabulated values as the definition of the sequence. The acceleration rate of PISTIL is set to its maximum value of $36000°\ s^{-2}$ to approximate as much as possible the desired step profile.

With respect to the surveillance of the motor, we differentiated five operation states:

1. The shutdown state in which the motor is not powered.

2. The idle state in which the rotor axis is maintained at a certain position, and its displacement by external force (e.g., manually effort) is impossible.
3. The "in motion" state reacting to a user motion command. The motion can have a specified duration, or an undefined duration that requires the user to eventually end the motion.
4. The "ending motion" state answering to a user command to end the current motion and return to the idle state.
5. The "Error" state if any hardware error or programmed error occurred, the on-going motion is halted immediately and the motion controller becomes inactive. A manual hardware reset is required to restart the controller.

3.3.3 Axial position configuration

The axial position of the rotor and the stator are maintained stable as they are respectively clamped to the motor and the structure of PISTIL in the states 2, 3, 4 and 5 of the motor operation.

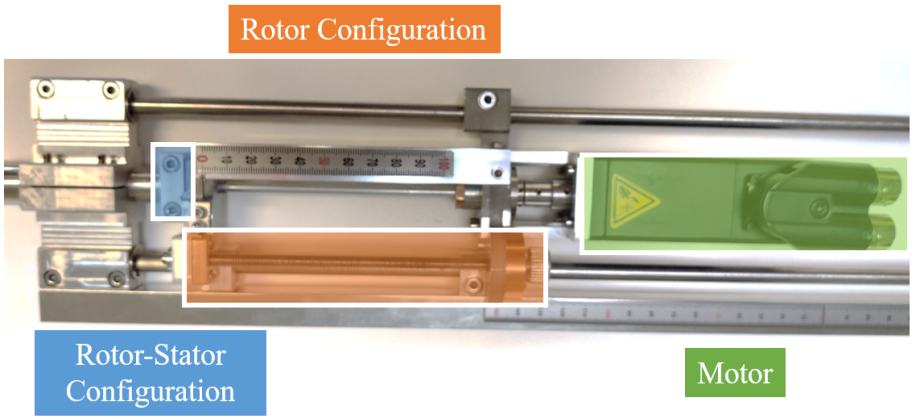

Figure 3.10: Motor and axial position configuration systems of PISTIL

In the shutdown state, there is the possibility to modify either the axial position H_1 of the rotor-stator as an ensemble, or to vary the relative position H_2 of the stator with respect to the rotor. As a convention in the following of this document, the mid-height position of the rotor and stator cadmium elements will be used as the parameters to indicate the axial position configuration setting, as indicated in figure 3.11. H_1 can be set between 350 mm and 850 mm of the water level. H_2 can vary between 0 and 100 mm, such that the cadmium strips move from fully covered to uncovered axially.

Table 3.5: Axial position configurations

Item	Minimum (mm)	Maximum (mm)	Reference (mm)	Background (mm)
Rotor-Stator assembly H_1	350	850	550	750
Stator position H_2	0	10	0	10

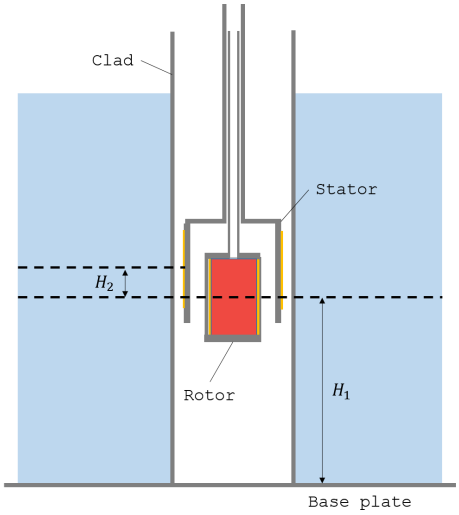

Figure 3.11: Axial position convention for configuration changes

3.3.4 Data acquisition system

The resolver (transducer) integrated in the motor of PISTIL allowed to measure an angular position with a precision of 0.001° at a frequency of 1 kHz. Due to limited disk space of the NC, it was not possible to store the entire sequence of position data for a duration longer than 10 minutes. Therefore, an Ethernet connection based data transmission scheme was implemented for transmitting position data storage on a PC as shown in figure 3.12.

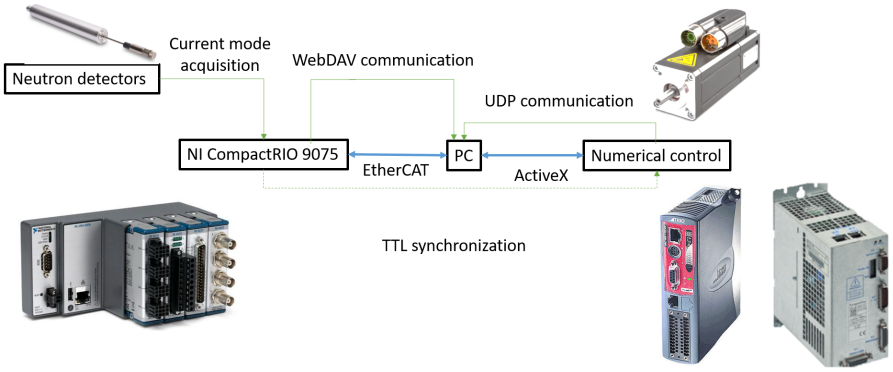

Figure 3.12: Communication scheme between different components

For the measurement of the ZPTF phase by modulation, the synchronization between the position signal and the neutron detector signals measuring the reactor flux variation is crucial. It was also desired to have a single Graphical User Interface (GUI) integrating the data acquisition and motion control functionality. Consequently, we developed a software based on LabView programming to accommodate these functions.

3.3.4.1 LabView based software development

A real time system guarantees a response time within the specified time constraints. It ensures a constant interval between time-stamps of two successive series of measured data, which offers more reliability to the data acquisition scheme. PISTIL was coupled to a National Instrument CompactRIO-9075 controller (referred to hereafter as CRIO). We programmed the CRIO to operate in Real-Time (RT) with a graphical user interface using LabView and its Field Programmable Gate Arrays (FPGA) module. The synchronization between the NC and the CRIO acquisition was accomplished by a 5 V transistor-transistor logic signal sent from the CRIO to the NC. The TTL signal triggers the beginning of the NC acquisition. It is worth mentioning that the NC acquisition is independent of the reference clock of CRIO and the real-time feature is not guaranteed.

The software accomplishes the acquisition of neutron detector signals in the form of a voltage at 1 kHz. It also offered wrapper functionality to configure and control the PISTIL motion through ActiveX programming and additional emergency stop control by a manual switch panel. The software emergency stop was programmed to avoid additional commands sent to PISTIL after that of the NC of PISTIL.

3.3.4.2 CRIO modules

For the implementation of the above described functionalities, the CRIO was equipped with three acquisition and control modules:

- A NI 9223 analog voltage input module with 4 channels and a sampling rate up to 1 MHz, in order to measure neutron detector signals;
- A NI 9401 digital 5V/TTL I/O module sends the synchronization trigger with a maximum latency of 100 ns;
- A NI 9344 user interface module was used for the manual emergency stop of PISTIL.

3.3.5 Experimental configuration

The PISTIL device was designed to be installed in CROCUS in the core center. Figure 3.13 shows the device loaded in the core. As a reference configuration, the stator and rotor cadmium elements were positioned axially at 550 mm height and fully covered axially. This axial position was chosen as it was the closest position to the mid height where the neutron flux reaches its maximum so that the modulation effect is maximized. The actual mid-height was not accessible as part of the motor of PISTIL was too massive and block the extraction of the safety blades before reactor start-up.

The experimental setup is shown in figure 3.14. Four Photonis CFUL01 FCs (1 g ^{235}U deposit) were positioned at the core periphery, in the four cardinal positions with respect to the device, as shown in figure 3.14. These detectors operate in current mode. They were developed and tested in previous branching noise studies [31]. It should be noted that the current implementation of the amplifiers of the FCs is not compatible with the neutron flux measurement above a reactor power of 2 W. At higher power, the electronic components of the amplifiers are saturated. Furthermore, the FCs also exhibit increasing

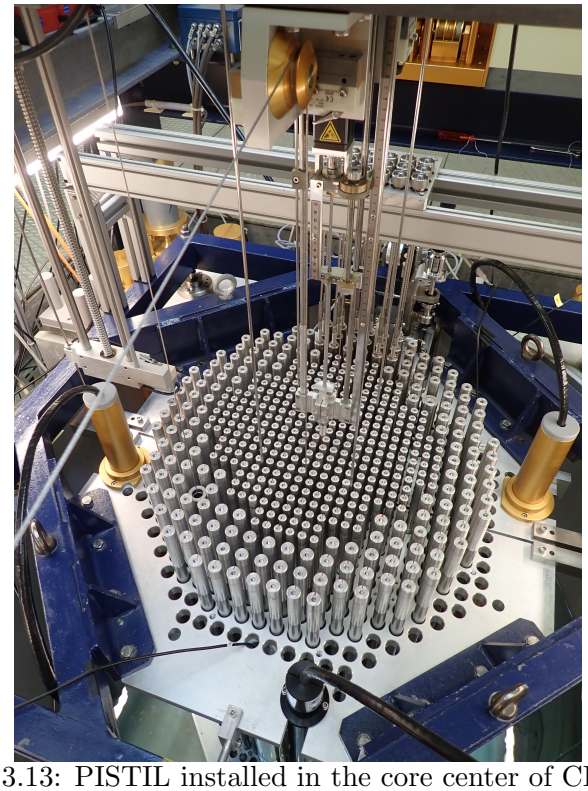

Figure 3.13: PISTIL installed in the core center of CROCUS

dead time with the power increase. The optimal power range of their operation is between 0.1 and 1.2 W.

The detectors were referenced as Det 1, 2, 3 and 4 from the one in the north in clockwise order. They were located in air-channels in the water reflector, as close as possible to the fuel rods in the outer layer of the active core. It is worth mentioning that the detectors were not exactly at equivalent distances of the core center due to difficulty to install them within the fuel zone. The cRIO was connected to the voltage output of the FCs for the acquisition. For the modulation experiments, the B_4C control rod was systematically extracted from the core, which led to the presence of two empty guide tube filled with air in symmetrical positions.

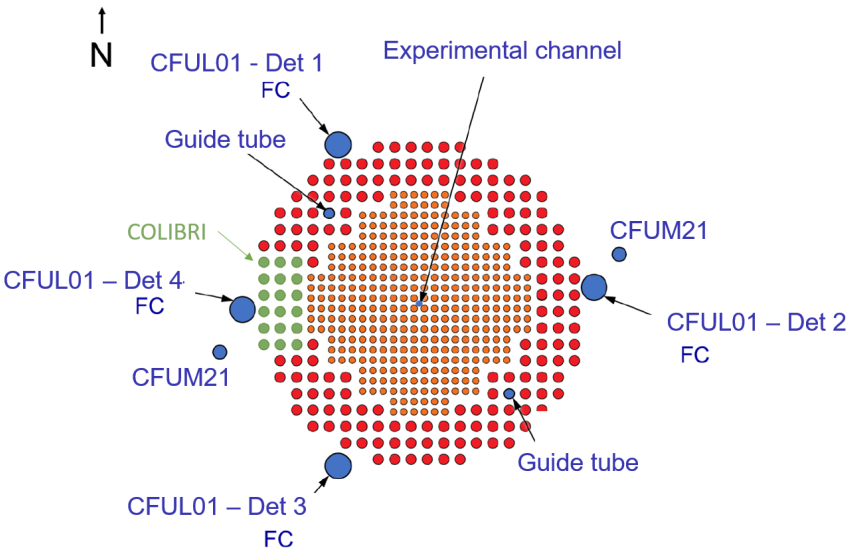

Figure 3.14: Schematics of reactor instrumentation of CROCUS and PISTIL

3.4 Chapter summary

We reviewed the design studies of the PISTIL modulator. The design adopted a coupled analysis of the neutronic, mechanical and electronic aspects.

We showed that with the increasing computing power available and the development of Monte Carlo neutron transport code, it is possible to have an accurate prediction of the reactivity worth of a transient by discretizing the time dependence into multiple static model. A multi-approach modeling was applied using these models to accelerate the iterations of the modulator design. PISTIL was equipped with a numerical motion control to realize the rotation. It was installed in the center of CROCUS for modulation experiments.

PISTIL was manufactured with the expected performance. A software with UI, integrating the acquisition of PISTIL and neutron detectors, as well as the motion control of PISTIL.

Chapter 4

Design of the Modulation Experiments

This chapter gives an overview of the experimental design for the determination of the campaign program of PISTIL, in the framework of the Amplitude and PHase Response of an Oscillating Device Investigated by Theory and Experiment (APHRODITE) project. A series of modulation experiments were conceived for the measurement of the ZPTF at different frequencies. A brief description of the numerical tool developed for the simulation of the modulation experiment is first given. Then, we outline the applied methodology for the analysis of experiments. Finally, we present the technical details of the experimental configuration and the procedure.

4.1 Neutronic model of a modulator

The design of modulation experiments requires the determination of a combination of design parameters: the reactor power, the positioning of neutron detectors, the duration of the measurement, and the shape of the reactivity signal which affects the harmonic components of the modulation in the frequency domain. It is also important to take into account the impact of the detection process on the quality of the experimental data. The presence of the branching noise also contributes to the overall uncertainties in ZPTF measurements. The design of the experimental program relies on a modeling tool that allows the estimation of the transient induced by a reactivity modulation in the core. The

measurement of neutron detector signals is also modeled. The objective is to determine the compatibility of measurements at different frequencies, the measurement duration and the reactivity modulations generated by PISTIL.

The neutronic behavior of CROCUS is simulated by a PK model. The reference configuration of CROCUS [1] is used in the model. The adjoint-weighted kinetic parameters are estimated using TRIPOLI-4 simulations by the Iterated Fission Probability (IFP) method [97] with the JEFF-3.3 library, documented in table B.1.

In the model, the initial state of the core is delayed critical without an external neutron source. Periodic reactivity modulations $\rho(t)$ induced by the motion described in section 3.3.2 are introduced. The variation of the neutron and precursor population is determined by numerically integrating the PK equation, using the Adams method or BDF method with automatic stiffness detection and switching for convergence acceleration. This allows to avoid numerical oscillations in the algorithm of iterative resolution described in [98].

The model converts the time series of neutron population into a neutron detector signal. The efficiency of the detector was set to 1×10^{-4} counts per unit fission based on a calibration in a previous branching noise study [31] of large fission chambers instrumented in CROCUS. The noise measured by the detectors is simulated by a model in the branching noise theory [48]:

$$S_{n,n}(\omega) = \epsilon F + \frac{\epsilon^2 F D_\nu}{(\rho - \beta_{\text{eff}})^2} \frac{1}{1 + \omega^2/\alpha^2} \tag{4.1}$$

where $S_{n,n}$ is the distribution of the signal power in the frequency domain, ω is the angular frequency (rad.s^{-1}), ϵ is the detector efficiency, F is the integral in-core fission rate (fissions.s^{-1}). The fission rate is estimated to 3.12×10^{10} fissions.W^{-1}.s^{-1} considering on average a 200 MeV energy released per fission [75]. D_ν is known as the Diven factor [99] considered known. Its value is 0.8 as the thermal fissions of ^{235}U is predominant in the neutron emission [100].

The noise in the detection signals is sampled in the frequency domain using equation (4.1). The noise in the phase space is considered to be uniformly distributed in [-π,+π] and random with respect to the frequency. Figure 4.1 shows a case study of the simulated acquisition signal.

The detector signal without noise is simulated as a sine function of time. The noise is added to this ideal signal using the aforementioned steps. The different steps and components of the model process are outlined in figure 4.2.

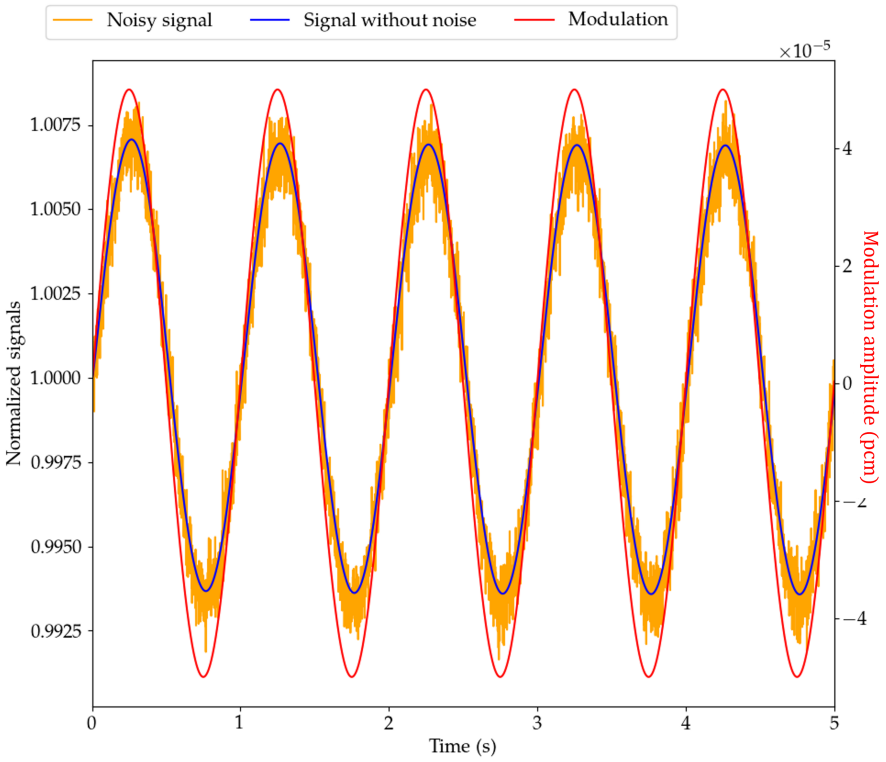

Figure 4.1: Simulated detector signals in the case of a 1 Hz reactivity modulation experiment

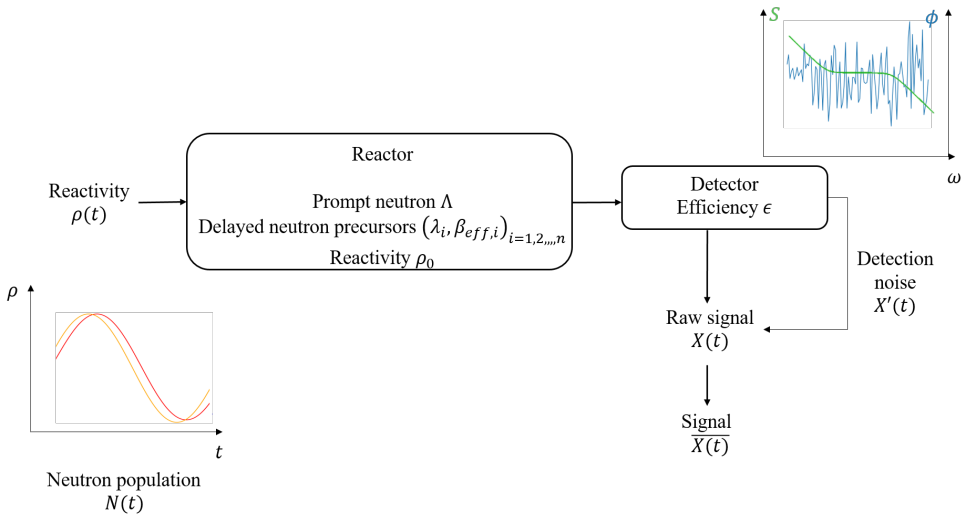

Figure 4.2: Block diagram of the numerical simulation of modulation experiments

4.2 Signal processing

The determination of the ZPTF relies on the analysis of acquired detector signals of a modulation experiment by applying signal processing methods. There are choices to be

made on the analysis parameters. This section illustrates the principal procedure of the processing applied to signals acquired in modulation experiments.

4.2.1 Periodogram estimates of power spectral densities

The acquired signals in experiments are discrete and finite by nature, as opposed to the signals in analytical Fourier analysis. The method allowing to compute their frequency domain spectra is referred to as Discrete Fourier Transform (DFT). The Fast Fourier Transform (FFT) algorithm [101] is widely used for the spectral analysis of discrete signals. It converts the time domain signal to a frequency domain representation. It allows the fast computing of the DFT that generates the Power Spectral Density (PSD) of the signal.

The PSD of two sequences of signal (x_i) and (x_j) is determined as:

$$S_{i,j}(\omega_k) = \frac{f_s}{N} FFT[x_i]_k \times \widetilde{FFT[x_j]}_k \; k = 1, 2..., 2N \tag{4.2}$$

where $S_{i,j}$ is the Auto Power Spectral Density (APSD) if (x_i) and (x_j) are the same sequence or the Cross Power Spectral Density (CPSD) when the two sequences are not identical. $\sim$ is the complex conjugate operator. f_s is the sampling rate (s^{-1} or Hz) and N corresponds to the minimum of the length of two sequences.

The obtained spectrum is referred to as the periodogram estimate. ω_k are the discretized frequency bins defined as :

$$\omega_k = \frac{f_s}{N} k \tag{4.3}$$

The power $P_{i,j}$ is estimated from the obtained spectrum by taking its modulus:

$$P_{i,j}(\omega_k) = 2 \parallel S_{i,j}(\omega_k) \parallel \; k = 1, 2..., N \tag{4.4}$$

The obtained power is reduced to a periodogram of length N due to its symmetry with respect to the null frequency.

The periodogram estimate involves the windowing of the signal. The fact that the signal has a finite length is equivalent to window an infinite length signal by a rectangular function. A consequence of the windowing is that the peaks that appear at the harmonic frequencies of the signal spectrum are broadened and the power is distributed in the main lobe and several side-lobes. This is known as the spectral leakage. In practical applications, adapted window functions such as the Hanning, Hamming and Blackman windows allow limiting the leakage by partial cancellation of side-lobes in the spectra [102]. The different windows are trade-offs between two competing objectives, which are to obtain a narrow main lobe and to attenuate the side-lobes. For instance, the width of the main lobe of the Blackman window is larger than that of the Hamming or the Hanning window, while it attenuates the side-lobes better. The window choice is therefore dependent on the application. The Hamming window is chosen in the present study. The reason is that it allows reducing effectively the first side lobe of the power leakage with a narrow main lobe, which facilitates the peak localization. An Hamming window of size M is defined as:

$$w(k) = 0.54 - 0.46\cos(\frac{2\pi k}{N-1}) \tag{4.5}$$

where k is the index within the sequence of size N.

Bartlett's method [103] is a variation of the periodogram estimate, which allows reducing the variance of the PSD estimation. In this method, the original signal of length L is split into m segments of window size N where $L = m \cdot N$. A PSD calculation is applied to each segment individually. The m spectra are averaged to produce a final PSD estimate. The relative uncertainty of $P_{i,j}$ of the estimate is evaluated to be proportional to $1/\sqrt{m}$ [104].

The uncertainty is estimated as:

$$\sigma^{exp}(f) = 1/\sqrt{m-1} \cdot \sum_{i=1}^{i=m} \sqrt{\frac{1}{m}(PSD_{average}(f) - PSD_i(f))^2} \tag{4.6}$$

where f is the frequency, PSD_i are the periodograms of each segment, $PSD_{average}$ is the PSD estimate of the Bartlett method.

The Welch's method [105], in a similar windowing manner of the Bartlett's method, averages the periodograms of windows that are overlapped. This approach allows to increase the number of windows for variance reduction. However, the average of overlapped windows implies correlations that are difficult to quantify. Consequently, the overlapped windowing is not considered in this work, and the Bartlett's method is used for the spectral analysis.

In order to measure the amplitude of the ZPTF $|| G(j\omega_k) ||$, the Quantity of Interest (QOI) for the analysis is the power of the APSDs at characteristic harmonic frequencies of the reactivity signal $P_{\rho,\rho}$ and that of the neutron detector signal $P_{X,X}$. The peaks are centered at ω_n and have a Full Width at Half Maximum (FWMH) of $\delta\omega$.

The peak power is determined by summing the power of the peak bins. $|| G(j\omega_n) ||$ is calculated as:

$$|| G(j\omega_n) ||= (\int_{\omega_n-\delta\omega}^{\omega_n+\delta\omega} P_{X,X}(\omega)d\omega / \int_{\omega_n-\delta\omega}^{\omega_n+\delta\omega} P_{\rho,\rho}(\omega)d\omega)^{0.5} \tag{4.7}$$

The phase difference information $\Theta_{\rho,X} = \arg[G(j\omega_k)]$ is calculated using the CPSD between the reactivity and neutron detector signals:

$$\Theta_{\rho,X}(\omega_n) = \arg[P_{\rho,X}(\omega_n)] \tag{4.8}$$

Note that ω_n are also the frequencies at which the modulus of the CPSD reaches its local maximums.

4.2.2 Processing of realistic detector signals in modulation experiments

The acquired signals are synchronized, they consist of channels of neutron detector signals $X(t_k)$, and in the case of PISTIL the perturbation signal $\gamma(t_k)$ (angular position). The modulation frequency is estimated by identifying the average length of the cycles of PISTIL motion.

The neutron detector signals are normalized by the moving average value:

$$X^{'}(t_k) = \frac{X(t_k)}{(X * h)(t_k)} - 1 \tag{4.9}$$

$$h(\tau) = \frac{1}{M} \sum_{k=1}^{M} \delta(\tau - t_k) \tag{4.10}$$

where $*$ is the convolution operator and h is the Gaussian kernel of size M. This operation allows to obtain a quasi-stationary signal on which the FFT algorithms are applied.

This step allows one to correct for the long term power drift of the core and local adjustment of the core reactivity by the operator, which introduce bias to the ZPTF measurement. As an example, a fraction of typical averaged neutron detector signals without the intervention of the operator in the experiments is shown in figure 4.3. The evolution of the averaged signal illustrates that the reactor is supercritical.

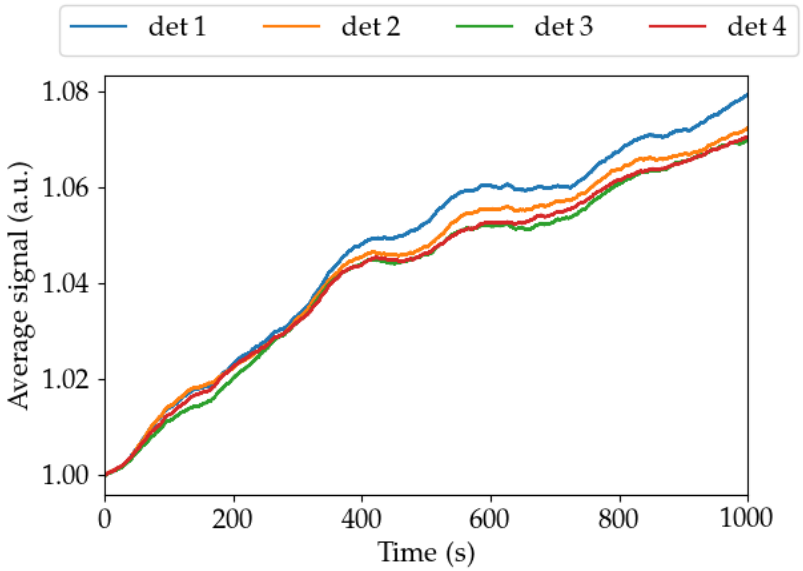

Figure 4.3: Drift of neutron detector signals after moving average calculation

As shown in equation (4.7), the absolute measurement of the ZPTF amplitude requires the reactivity signal. However, the reactivity can not be measured directly. The accessible experimental observable related to the modulation is the angular position of PISTIL. It was therefore necessary to derive a "reactivity signal" from the measured angular position signal for absolute ZPTF amplitude measurement.

The reactivity signal $\rho(t)$ is estimated as:

$$\rho(t) = f[\gamma(t)] \tag{4.11}$$

where $\gamma(t)$ is the angular position.

The function f is obtained from the reactivity calibration presented in section 5.1.3.

As stated in sec:periodo, the APSD and the CPSD between processed signals $X'(t)$ and $\rho(t)$ are estimated using Bartlett's method and the Hamming window. The reason for selecting Bartlett's method is that the windows are not overlapped so that there is no correlation introduced in averaging the periodograms.

Since the modulation of PISTIL in CROCUS is configured by the user, the frequency ranges (bins) involved in the ZPTF measurement is a known input *a priori*. For the estimation of the peak power and the phase, it is optimal to have the frequency bins of the PSD to be exactly at the input modulation frequencies. Therefore, the window size is adjusted to be an integer number of the period of the modulation.

4.3 Design studies

4.3.1 Criteria

Previous modulation studies in CROCUS were realized in the framework of the European project CORTEX [40]. They consist in the generation of the oscillation of fuel rods in the core periphery. These studies aim at improving the detection capability of localized in-core events for reactor monitoring. The goal of APHRODITE, by contrast, is to provide measurement of a global behavior through ZPTF, which is considered as an integral observable for kinetic parameter estimation and nuclear data oriented applications. Despite the difference in objectives, the experiments have similar experimental requirements and data acquisition scheme. This offered some insights for the experimental design of the current work.

A feedback from the previous studies in CROCUS is that modulation measurements of several hours can be conducted at a stable reactor power and with a limited number intervention of the operator (e.g., 2-3 adjustment to be taken into account for correction). In the reference setup, the control rod is entirely extracted from the core. The reactor is operated by modifying the water level with an accuracy of 0.1 mm (approximately $\pm$ 0.4 pcm reactivity worth around criticality). For the determination of the critical water level, the operator adjusts progressively the water level till the reactor power remains stable for at least 5-10 minutes using reactor's safety monitors (acquisition rate of 1 Hz) and the operation doubling time display. A long duration of observation (generally between 20-30 minutes) is necessary for reactor start up and stabilization of one run of modulation experiment.

The Signal-to Noise Ratio (SNR) is used as a criterion for the determination of the modulation frequencies and the duration of the measurements. In the context of the current work, it is defined as the metrics of the quality of the useful signal with respect to noise signal:

$$\mathbf{SNR} = \frac{\int_{\omega_1}^{\omega_2} P_{i,i}^{signal}(\omega_k)d\omega_k - \int_{\omega_1}^{\omega_2} P_{i,i}^{noise}(\omega_k)d\omega_k}{\int_{\omega_1}^{\omega_2} P_{i,i}^{noise}(\omega_k)d\omega_k} \tag{4.12}$$

The SNR concerns various sources of noise (the detection noise, the branching noise, experimental anomalies, etc). It can be improved by increasing the in-core neutron flux. With the aforementioned limitations in section 3.3.5 of the detector development, the optimal reactor power is about 1 W, which corresponds to a neutron flux of 2.7×10^7 cm.$^{-2}$.s^{-1} in the core center.

4.3.2 Modulation profiles

As observed in the literature, a continuous rotation of rotor's absorber elements that induces a sine (or pseudo-sine) shape modulation is an efficient manner in investigating the ZPTF. An illustration of the modulation profile and simulated neutron detector signal is given in figure 4.4

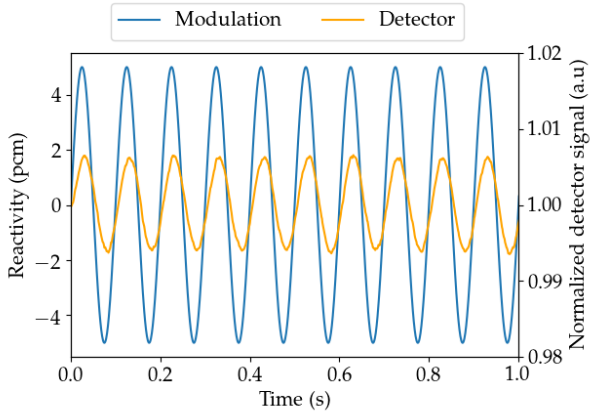

Figure 4.4: Illustration of the sine-shaped continuous modulation and sampled neutron detector signal at 1 kHz

The spectrum of pseudo-sine signal has its power at several specific harmonic frequencies, which makes complicated the peak identification from the background noise. Furthermore, as compared to other option of the modulation, a sine-shaped reactivity modulation is the most prominent manner for uncertainty reduction when the same quantity of data are acquired. This led to choose in the case of APHRODITE, a continuous rotation mode (constant frequency) down to a frequency of 0.25 Hz to approximate a sine-like reactivity variation. The upper limit of the rotation is defined by the maximum speed of the motor at 100 Hz.

For the ZPTF measurement at low frequencies (< 1 Hz), the sine-shaped modulation remains time consuming. Despite the accuracy of the measurement, each experiment consists of the production of approximately 2-4 experimental data for further interpretation. The Pseudo-Random Binary Sequence (PRBS) is an alternative profile to sine-shape for reactivity modulation to measure a number of harmonics (> 10) in one experiment with acceptable duration. The step-wise motion of PISTIL allows it to follow a predefined position profile. When the profile consists in the alternation of two values, the motivation for adopting PRBS-like modulation is to optimize the measurement time and the quantity of experimental data as integral ZPTF measurements. The PRBS modulation is not compatible with high frequency experiments (in the order of 0.1 Hz) due to the difficulty to realize the step-wise motion fast enough.

The Maximum Length Sequence (MLS) [106] or n-sequence is selected as the motion profile in order to probe the ZPTF of the reactor simultaneously for a large number of frequencies of the harmonics. The number of harmonics is defined by the parameter bit, with the increase of which the total number of harmonics increases. An example of the

frequency domain spectrum of a n-sequence is shown in figure 4.5.

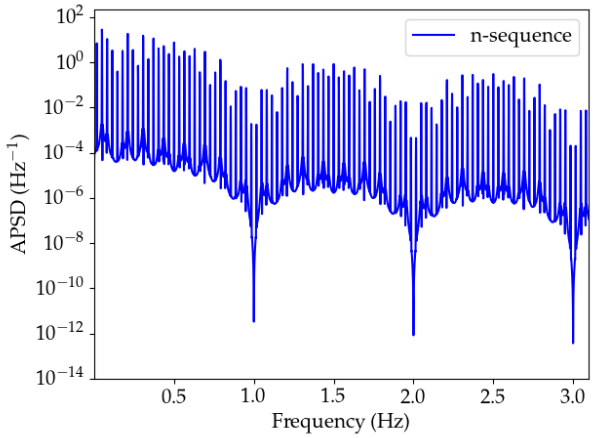

Figure 4.5: Power spectral density of a 5-bit n-sequence signal with a fundamental frequency of 0.016 Hz

However, it should be noted that the complexity of the implementation of a n-sequence like step-wise motion rises with the bit order. The size of the sequence increases as a power of 2 of the bit value $(2^{n+1} - 2)$, and consequently lengthen the measurement time. A n-sequence of 5 bits (62 steps) was considered as a trade-off between the complexity of the sequence and the number of harmonics to exploit. The 5 bit n-sequence is generated as the basis of the motion profile. The fundamental frequency of the step-wise modulation was adjusted by varying the unit time interval between two consecutive steps of the sequence.

An example of a 1 s time interval step-wise modulation and the corresponding neutron detector signal is shown in figure 4.6. In this work, by choosing a time step up to $t = 10$ s, the lowest measurable frequency of the ZPTF is $\frac{1}{10 \cdot (2^{n+1}-2)} = 1.6$ mHz.

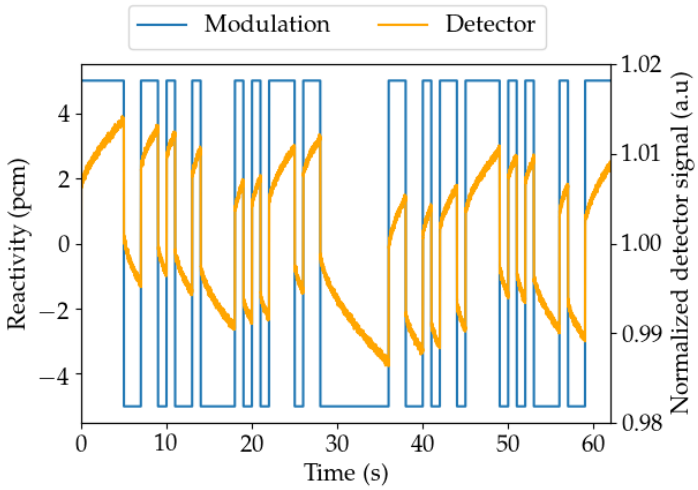

Figure 4.6: A 1 s step-wise modulation and sampled neutron detector signal at 1 kHz

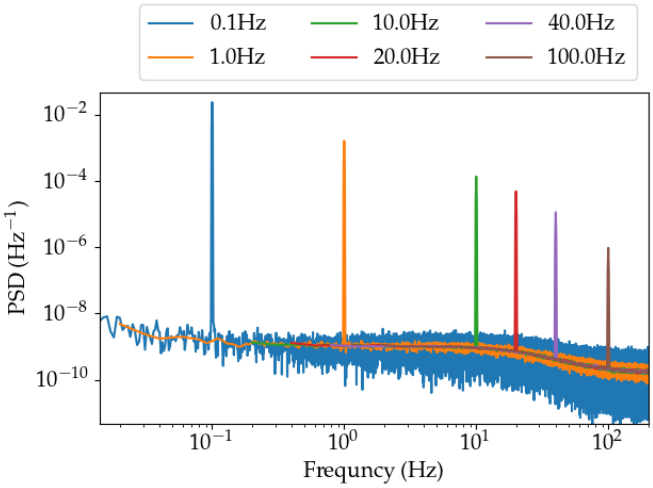

Figure 4.7: APSD spectrum of the simulated detector signal subject to a 5 pcm monochromatic modulation at 0.1, 1, 10, 20, 40 and 100 Hz

The determination of the measurement time was based on the analysis of the numerical simulation of the modulation as discussed in section 4.1. Figure 4.7 shows a case study of the power spectrum obtained from the simulation of reactivity modulation at various frequencies.The modulations are all simulated as a time-varying sine function of 5 pcm in amplitude. The simulated detector signals were sampled at 1 kHz, and were analyzed using Bartlett's method with a window size of 100 modulation periods.

The peaks in figure 4.7 show high amplitude peaks as compared to the background, but their SNRs have different order of magnitudes, as shown in figure 4.8. In the range of frequencies relatively low (about 1 Hz), the SNR of the order of 2000, while at higher frequencies the SNR decreases significantly. This can be seen as the consequence of competing effects between frequency domain resolution and noise reduction using Bartlett's method.

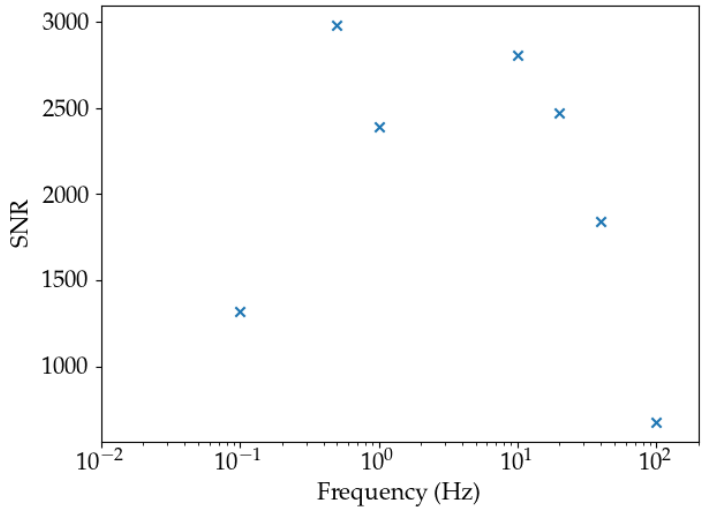

Figure 4.8: Estimated SNR of the simulated 30 minutes detector signal

Equation (4.1) shows that the noise measured by the detection has one part proportional to the amplitude of the ZPTF, and another one independent of the frequency corresponding to a white noise source. It should be noted that the amplitude of the neutron detector signals is also proportional to the amplitude of the ZPTF, while the amplitude of the white noise is constant. This causes the signal amplitude to decrease with the frequency. In consequence, we limited the upper threshold of the frequency of the measurements to 200 Hz, for which the SNR is reduced to 4 with the increase of the frequency.

It is observed that for a simulated measurement time of above 25-30 minutes, there is an improvement of the SNR with respect to time. A minimum acquisition time of 30 minutes is determined for the continuous rotation experiments.

A summary of the modulation type and estimation of the duration of the experiments with the aforementioned considerations is given in table 4.1. In addition to them, reactivity calibrations were realized through multiple measurements that is discussed in section 5.1.

Table 4.1: Typical ranges of modulation frequency and measurement time

Type	Fundamental frequency (Hz)	Typical measurement time (min)
Continuous	0.5-16	30
Continuous	20-100	30
Step-wise	0.005-0.01	60
Step-wise	0.001	120

In table 4.1, both the continuous and step-wise motions were distinguished into two categories for the experimental implementation.

- In the continuous case below 20 Hz, the frequencies were chosen to be 2^n (n={-1,0,...4}). As will be discussed in section 5.1 the reactivity calibration of PISTIL shows that its reactivity profile relating to the angular position is not monochromatic, multiple harmonics can be measured in one experiment. Therefore, such a choice of frequency set would allow to obtain multiple measurements at the same frequency in experiments at different rotation frequencies to check the consistency of the obtained data.

- The frequencies above 20 Hz were treated separately due to the appearance of the mechanical noise, as mentioned in appendix A.2. The mechanical vibrations in this frequency range would induce additional neutronic effects than the modulation itself. Although no clear impact can be observed in the spectra, single out these frequencies reduced the risk of hazards and aberrations in the experimental data.

- The step-wise modulation bridged the gap between the intermediary low frequencies and the continuous ones by setting the unit time step of the n-sequence to 1 s and 2 s. This helped to verify the continuity of the data and consistency between the two methodologies.

- The extremely low frequency measurements with a unit time step of 10 s, were distinguished from the precedent case. They required some special attentions as one single cycle of acquisition takes more than 10 minutes for the measurement of the

ZPTF at the fundamental frequency of 1.6 mHz. This led to asymptotic increase or decrease of the reactor power, since one step of reactivity insertion lasted up to 80 s. Care was taken on the average reactor power so that the power did not fall below 0.8 W or above 1.2 W for the performance of the CFUL01s. The operator adjusted the position of the spillway, which required calculation correction of the measured data to take into account the additional reactivity variation.

For the absolute measurement of the amplitude of the ZPTF, a normalization by the amplitude distribution of the reactivity for each of the harmonics of the modulation is required. Therefore, a reactivity calibration of PISTIL was conducted with multiple experiments. They concern either the differential reactivity between several angular positions, or the reactivity profile as a function of the position. The calibration with respect to these two types of measurements was conducted by three different techniques: reactivity compensation, asymptotic period and inverse kinetics [107]. In this manner, a cross-verification of the measured reactivity worth was conducted.

4.4 Methods of reactivity calibration of PISTIL

For the absolute measurement of the amplitude of the ZPTF, it is necessary to measure the reactivity signal. However, the reactivity cannot be directly measured. As PISTIL has access to its angular position, the reactivity signal can be inferred from the motion signal. This requires a reactivity calibration of PISTIL.

4.4.1 Reactivity compensation

The reactivity compensation method applied to the reactivity calibration of PISTIL consists in the determination of the critical water level for different angular positions of PISTIL. The values of water level were compared to that of a reference angular position, which is the configured 0°. The differential reactivities were estimated using the knowledge of reactivity worth of approximately 4 pcm per mm of water level near criticality.

$$\rho(\gamma_2) - \rho(\gamma_1) = 4(H_c(\gamma_1) - H_c(\gamma_2)) \tag{4.13}$$

where γ is the angular position of PISTIL and H_c is the critical water level in mm.

As the value of 4 pcm per mm is an approximation from previous calibrations near critical water level [1] with a precision of $\pm$ 0.4 pcm, the measured differential reactivities were considered qualitative and required to be complemented by the results from the two other types of experiment.

4.4.2 Asymptotic period

The use of asymptotic period method aimed at measuring the differential reactivity between two angular positions $\gamma_1 \rightarrow \gamma_2$ for an initially critical core. The shift of either the water level or the angular position of PISTIL induces a step change of the core reactivity that drives the core neutron flux to increase or decrease. The core power variation can be

described by a sum of exponentials:

$$N(t) = N_0 \sum_{i=0}^{n} e^{\omega_i} t \tag{4.14}$$

where the n+1 ω_i values are solutions of the inhour equation [75]:

$$\Delta\rho(\gamma_1 \rightarrow \gamma_2) = \Lambda\omega + \sum_{i=1}^{n} \frac{\omega}{\omega + \lambda_i} a_i \beta_{\text{eff}} \tag{4.15}$$

4.4.3 Inverse point kinetics

The third approach, the inverse point kinetics method consists of the measurement of a dynamic reactivity variation $\rho(t)$ produced by a time varying modulation $\gamma(t)$. The reactivity is estimated by the inversion of the PK equation [42]:

$$\rho(t) = \frac{1}{N(t)} \sum_{i=1}^{n} \lambda_i \beta_{eff,i} \int_{-\infty}^{t} [N(t) - N(\tau)] e^{-\lambda_i (t-\tau)} d\tau + \Lambda \frac{\frac{\partial N(t)}{\partial t}}{N(t)} \tag{4.16}$$

Before the calibrations, the cadmium elements on rotor and stator were both settled to be centered at the reference axial position of 550 mm. As discussed in section 3.3.5, this value corresponds to the reference experimental configuration of the campaign. The estimated reactivity of this configuration was between -118.1 ± 4.7 ∼ -111.7 ± 4.8 pcm (-0.156 ∼ -0.145 $) with TRIPOLI-4 calculation using JEFF-3.3 library.

4.5 Experimental procedure

A standard procedure is applied to the experiments:

- Before the reactor start-up the angular position is set mechanically at the reference 0°. It is maintained at this position by the servo-motor.
- The reactor is brought to criticality when the B_4C rods are fully extracted. The reactivity control is achieved by the increase of the water level (variation of the position of the spillway) with the insertion of the PuBe neutron source. Once the criticality reached, the neutron source is removed.
- After the confirmation of a steady state by the operator, motion command are sent to the NC of PISTIL.
- In the case where the reactor power exhibited slow drifts during the motion, the operator would not correct the drifts as long as the reactor power remained within 0.8 and 1.2 W, which is the optimal functioning condition of the electronics of the FCs.
- Between multiple experimental runs, PISTIL is again maintained at 0°, the operator maintained the reactor critical.
- After the completion of the scheduled experiments, the reactor is shut down and PISTIL reaches 0° before its switch off.

4.6 Chapter Summary

The experimental design of the APHRODITE campaign relied on the development of a simulation tool of reactivity modulation, predicted with a point kinetic model of CROCUS. The experimental program consists of different sets of measurement of the ZPTF with a frequency range between 1 mHz and 200 Hz. The essential element of the design is to characterize the low frequencies and the high frequencies with two different strategies. At low frequencies, the goal was to measure multiple harmonics in the same experiment. In contrast, limited number of harmonics were probed in every single experiment at high frequencies. These two strategies were chosen for the optimization of the duration of the experiments and quantity of measurements.

Chapter 5

Experimental Determination of the Zero-Power Transfer Function of CROCUS

Modulation experiments were conducted in CROCUS for the measurement of its ZPTF. This chapter presents the experimental results of the reactivity calibration of PISTIL, the experimental value of the ZPTF and the comparison with theoretical predictions computed with JEFF-3.3 and ENDF/B-VII.1 libraries.

5.1 Calibration of the modulation reactivity worth

Reactivity calibrations are necessary for the normalization of the APSD of neutron detector signal. For the modulation studies of PISTIL, the calibration concerns the knowledge of differential reactivity between angular positions. Three different techniques are used for the reactivity calibration, which is driven by the different needs in the characterization of the device. They provide experimental data that are required for the analysis of ZPTF measurements of continuous and step-wise experiments presented in section 4.3.2. The three types of measurements are analyzed independently and offers a redundancy for cross-verification of the determined reactivities.

5.1.1 Reactivity compensation

Through a series of static measurements by the reactivity compensation method described in section 4.4.1, critical water levels with PISTIL at several angular positions are obtained. The comparison between overall differential reactivity worth and dynamic measurements will be shown in figure 5.3.

The angular positions of maximum and minimum reactivity worth are determined approximately at 80° and 350 °. Higher resolution of the angular position is complicated to obtain due to difficulties in the determination of the core reactivity lower than 0.4 pcm (0.1 mm water level).

It is verified that the two-fold symmetry of the rotor-stator system gives a reactivity worth profile that is approximately symmetrical with respect to the 180° position. Due to the angular precision of the mounting of cadmium foils and the slight difference of their mass on the rotor (respectively 0.680 and 0.686 g), an exact symmetry is not obtained.

5.1.2 Reference positions in step-wise motion

A step-wise motion control is implemented in the NC of PISTIL for the modulation experiments. It consists in the alternation between two angular positions that are approximately at the positions of the maximum and minimum reactivity worth, determined by differential reactivity measurements. For the determination of the exact difference of reactivity worth between these two positions, asymptotic period measurements are performed for the determined positions of 80° (γ_1) and 350° (γ_2) .

Prior to these measurements, the critical level with either the spillway or the control rod is determined for both positions (h_1 and h_2). The water level is then maintained at h_2 (i.e. critical water level at γ_2). Step reactivity insertion is generated in two manners: 1) shift the angular position of PISTIL or 2) shift the core reactivity control to the critical level of the another angular position (i.e. $(h_1, \gamma_2$ and $h_2, \gamma_1)$. The induced reactivity variation causes the reactor power to vary in an exponential manner. Figure 5.1 gives an illustration of the reactor power variation during one experiment of this kind. The count rates are recorded by the two safety monitors of CROCUS (Photonis CFUM21), which are proportional to the reactor power. The CFUL01 detectors were not used for the measurements, because in the calibration experiments the power reached higher levels than the threshold of saturation of these detectors at about 2 W.

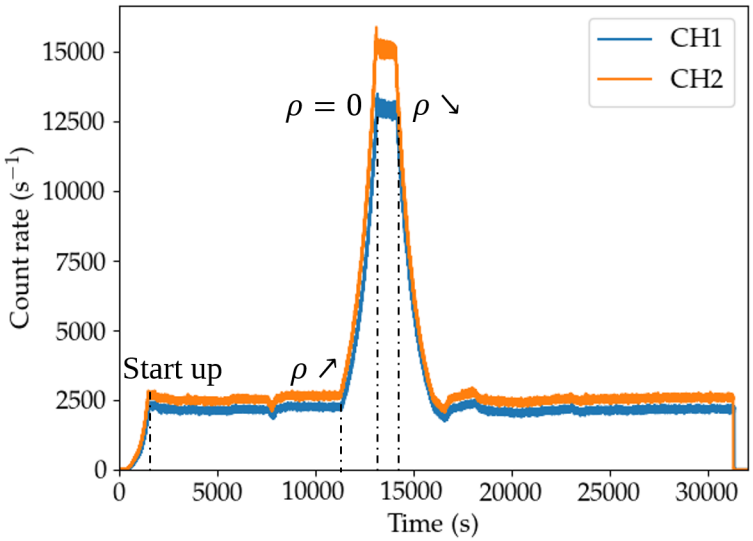

Figure 5.1: Neutron flux of CROCUS in the asymptotic period experiments monitored by the CFUM21 detectors CH1 and CH2

Estimations of reactivity worth from multiple asymptotic period measurements are analyzed with the asymptotic period model described in section 4.4 and are least-square fitted. The reactivity values presented in table 5.1 correspond to the estimation based on the period and the inhour equation (JEFF-3.3 data). The uncertainties are propagated using the covariance matrices of the fit parameters documented in appendix D.1. The overall differential reactivity between the two reference positions agrees with the results that are obtained with the reactivity compensation method and the inverse kinetics method presented in figure 5.2. The measurements of the same type (water level variation and rod position variation) shows consistent reactivity values. The difference between the measured values when the reactor is operated with the spillway or the water level could be caused by the slight difference in the determined critical water and rod height.

Table 5.1: Configuration of asymptotic period measurement and measured periods

Core water level (mm)	B_4C rod position (mm)	PISTIL position (°)	Period (s)	Reactivity (pcm)
h_2=984.0 ± 0.1 h_1=981.9 ± 0.1	1000.0 ± 1.0 1000.0 ± 1.0	γ_1=350 γ_2=80	1030.5 ± 7.4 -1097.0 ± 11.1	8.66 ± 0.06 -8.69 ± 0.09
990.0 ± 0.1 990.0 ± 0.1	h_2=715.0 ± 1.0 h_1=678.0 ± 1.0	γ_1=350 γ_2=80	1053.2 ± 5.1 -1126.7 ± 21.0	8.54 ± 0.04 -8.48 ± 0.17

5.1.3 Reactivity worth profile

In order to establish a model of the relationship between the reactivity worth and the angular position, another type of dynamic kinetic experiment is conducted. The experiments consist in rotating the rotor axis at a constant speed of 4° s^{-1} from an initial critical

state at about 1 W power. The speed allows the determination of a reactivity profile with an angular resolution of 1°. The CFUL01 detector signals were recorded and analyzed separately via the inverse kinetics method [107]. The reactivity profile is calculated using a non-linear least square fit algorithm [108], by a reactivity-angle function using Fourier decomposition:

$$\rho(\gamma(t)) = C_0 + \sum_{i=1}^{n} [A_i \sin(\frac{2\pi}{360} i\gamma(t)) + B_i \cos(\frac{2\pi}{360} i\gamma(t))] \tag{5.1}$$

where γ is the angular position in degree, A_i, B_i and C_0 are the fitted coefficients.

The 2π coefficient is used to ensure that the function has the same value at 0° and 360°. The coefficients A_i and B_i represent the phase of the harmonics. A direct fit of amplitude and phases of the harmonics are not conducted due to numerical issues in the convergence of the algorithm. The number and the orders of the harmonics in the fit are chosen based on the harmonics in the APSD of measured neutron detector signals. The time variation is proportional to the angular position as the speed is constant. The spectral harmonics of the detector signals correspond to the frequencies of the harmonics of the reactor response to the reactivity modulation. In the obtained APSDs (shown in figure 5.5 on the left), it is observed that only the first 5 harmonics emerged from the background noise. Therefore, the sum of these 5 harmonics is considered to be sufficiently representative of the overall reactivity modulation in regard to the angular position.

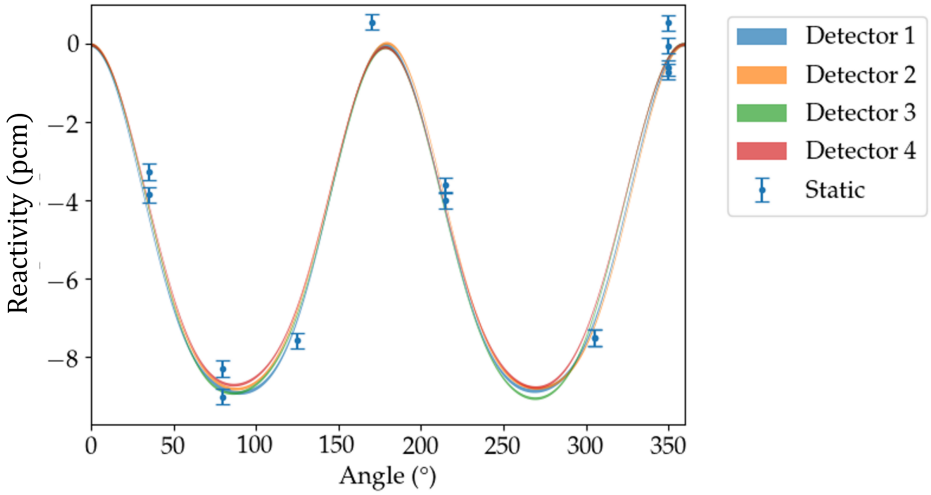

Figure 5.2: Calibrated reactivity profile and comparison with static measurement

For verification, the measured reactivity profile is compared to static measurements by compensation, as shown in figure 5.2. The static reactivities are in agreement with the values estimated using inverse kinetic method within 3σ uncertainty range. In figure 5.3 is also shown the APSD of the reactivity calculated with an ideal motion at 1 Hz. As expected, only the first five harmonics corresponding to the fit are identified.

The numerical values of the maximum difference in reactivity over 0° and 360° range is given in table 5.2. The fits give consistent estimation between detector responses,

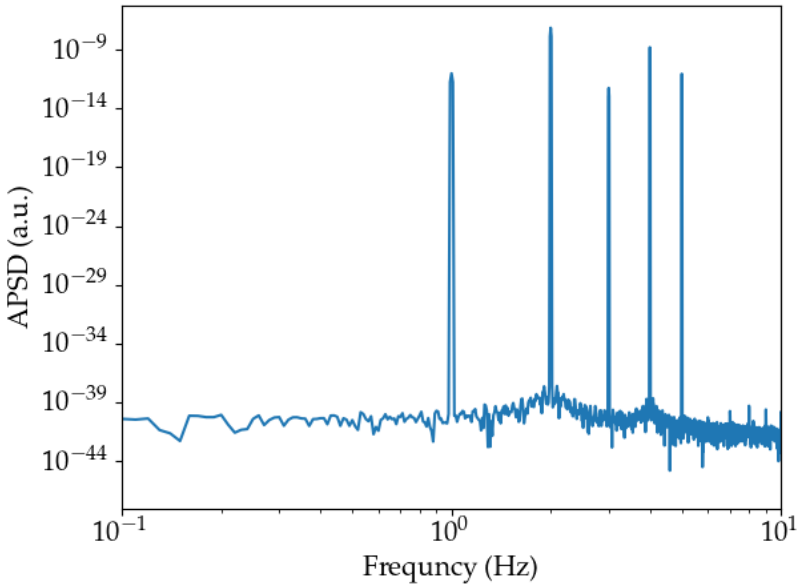

Figure 5.3: APSD of the reactivity for an ideal rotation at 1 Hz sampled at 1kHz with a window size of 1×10^5

covered by 1σ propagated uncertainty estimated with the covariance matrix of the fit. The values also agree with the TRIPOLI-4 calculation with a C/E value of 72.4 ± 39.0 % for the average of the four measured reactivity values. The gap in the reactivity value between detectors could be partially due to the oscillatory numerical behavior in the inverse kinetics method between time steps. Comparison of simulation and measurement of the reactivity profiles is shown in figure 5.4. Since the reactivity scale of the simulations and experiments are not identical, the numerical values are rescaled from 0 to -1 by the maximum difference from the same series of data. The rescaled values are consistent and shows that the reactivity profile has a pseudo-sin shape.

Table 5.2: Amplitude values of the calibrated reactivity profile using JEFF-3.3 data

Detector	Total amplitude(pcm)
1	8.88 ± 0.18
2	8.82 ± 0.16
3	9.04 ± 0.14
4	8.56 ± 0.14

The reactivity amplitude of the fundamental frequency of the modulation are given in table 5.3. They are estimated using the inverse kinetic method with the kinetic data of JEFF-3.3 and ENDF/B-VII.1 libraries respectively. This frequency is privileged for the experimental investigation of the continuous experiments, since it represents more than 95 % of the total power in the APSD of the reactivity. The measured results of different detectors are consistent between detectors within 1σ uncertainty.

The calibrated reactivity value within the PK formulation is dependent on the nuclear

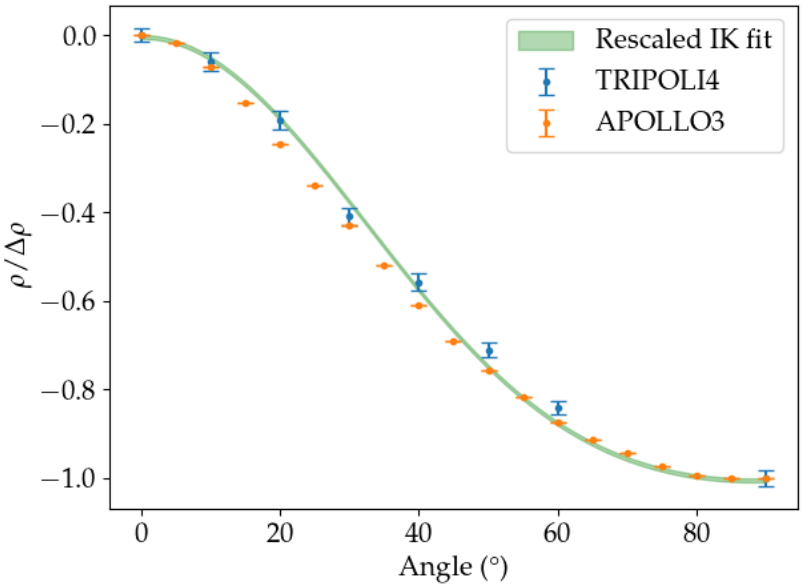

Figure 5.4: Rescaled IK fit and simulated data

Table 5.3: Calibrated reactivity amplitude of the fundamental frequency of the modulation using inverse kinetic method

Detector no.	Amplitude (pcm)	Library
1	4.42 ± 0.10	JEFF-3.3
2	4.39 ± 0.10	
3	4.46 ± 0.08	
4	4.34 ± 0.09	
1	3.97 ± 0.08	ENDF/B-VII.1
2	3.94 ± 0.08	
3	3.92 ± 0.07	
4	3.84 ± 0.08	

data library used to compute the kinetic parameters. Calculations are performed using kinetic parameters using TRIPOLI-4 with JEFF-3.3 and ENDF/B-VII.1 libraries. As shown in table 5.3, differences are observed in the calibration results. Separate analysis are therefore performed for comparison with calculations as it is not possible to calculate the APSD of the reactivity without taking into account the discrepancy in calibrated reactivity worth.

5.2 ZPTF amplitude and phase measurements

5.2.1 Spectral analysis parameters

The Bartlett's method with a Hamming window is used to compute the APSDs and CPSDs. We recall that the signals consist of 4 neutron detector signals $X(t)$ and 1 motion

signal $\gamma(t)$. Owing to the mechanical inertia of the device and the control system, the rotation frequency and the uncertainty is observed to be slightly different ($\sim$ 0.01 Hz) of the command value for high frequencies (above 40 Hz). Therefore, a systematic re-estimation of the rotation frequency is conducted before the peak finding procedure in order to measure the amplitude of the modulation, as discussed in appendix A.1.

For measurements of the continuous experiments, the APSDs of detector signals are calculated with a window size which corresponds to 100 periods of the modulation. This aims at reaching a spectral resolution of $\Delta f = 0.01 f_{\text{fundamental}}$ to accurately locate the peaks. Following this resolution criterion, at low frequencies of the perturbation (such as 0.25 Hz), the harmonics of the first, second, fourth and fifth order of the rotation frequency are identified from background noise, as shown on the left side of figure 5.5. Only in several experiments, the third harmonic is also present with a reduced amplitude as compared to the other 4 harmonics. The SNRs of the peak power are deteriorated with the increase of the modulation frequency, despite the increase of the number of windows in the FFT which reduces the variance of the spectral estimation. As the harmonics other than that of the fundamental of the modulation (second order of the rotation) have 2 to 3 orders of magnitudes lower than the second dominant harmonic, they become rapidly overwhelmed by the background noise with the increase of the modulation frequency. For measurements higher than 16 Hz, the asymptotic decrease of the ZPTF amplitude (i.e. -20 dB per decade) degrades the SNR due to higher relative power of the branching noise as compared to the peak power of the modulation. Thus, the window size is adjusted to accommodate about 10 s of data, a size tested to be a reasonable compromise between variance of the APSDs and peak power.

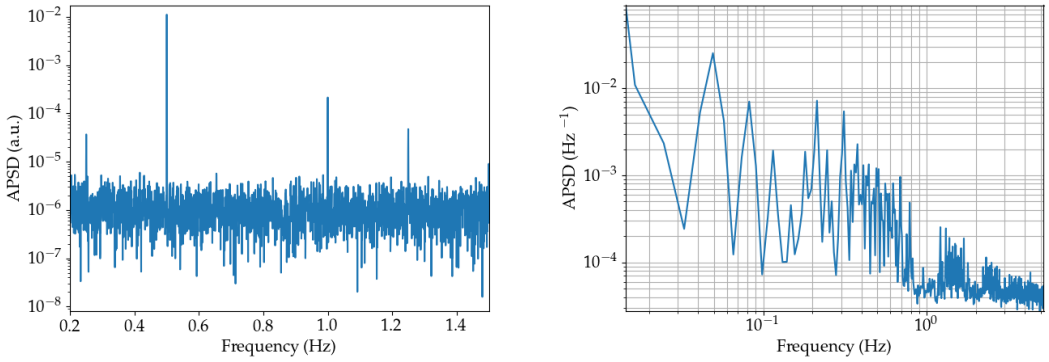

Figure 5.5: APSD of a 0.25 Hz continuous rotation experiment, with a frequency resolution of 0.0025 Hz (left) and APSD of neutron detector signal of a step-wise experiment (2 s unit step) with a frequency resolution of 0.82 mHz (right) measured using detector 1

A resolution of $\Delta f = 0.01 f_{\text{fundamental}}$ is impossible to obtain for step-wise modulation experiments due to limited duration of the experiments, as such a resolution requires a window size larger than 1.5 hour of acquisition data in the worst case. The obstacle in the analysis of the data is to obtain APSDs with the appropriate resolution in order to prevent peak-overlapping. Figure 5.5 (right) illustrates the APSDs calculated from detector signals of a step-wise experiment with a fundamental modulation frequency of 8.2 mHz. The peak at the fundamental frequency is hidden by the background noise, and it overlaps with the

boundary of the second harmonic due to the insufficient resolution. Each "spike" in the spectrum represents one single peak or a partially overlapped peak. The power estimation would therefore be overestimated with this insufficient resolution.

The peaks in the APSDs have a width of at least 5 bins, and it is necessary in the analysis to estimate the power of the background noise outside the peak region. A resolution of $\Delta f = 0.1 f_{\text{fundamental}}$ is selected for the determination of the window size to analyze the step-wise experiments, which corresponds to a window size of 10 cycles of the modulation (e.g., 1220 s for a for a step-wise modulation with unit time step of 2 s). The large window size leads to much smaller sample size (less than 10 windows for 1 hour of measurement) for the statistical estimation of the uncertainty in the analysis of the step-wise experiments as compared to the continuous ones.

5.2.2 Estimation of the peak power and phase difference

The spectral spread due to the windowing requires the summation of the power of multiple bins of the APSD to obtain an accurate estimate of the signal's harmonics. The peak power estimation consists in the identification of the frequency bins of local maximums and the associated boundaries, the summing of the power in the bins, and the estimation of the background noise for its subtraction and the estimation of the uncertainty as illustrated in figure 5.6.

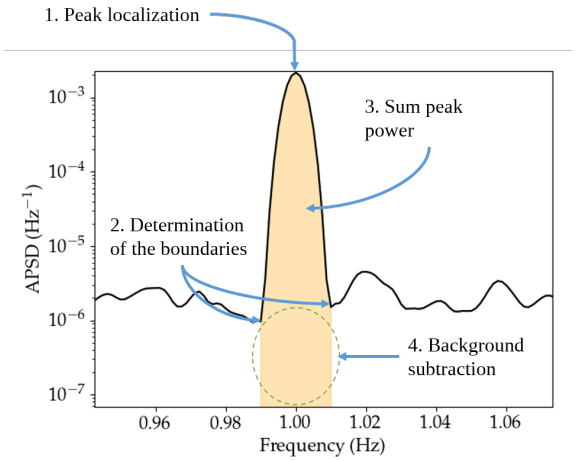

Figure 5.6: Illustration of steps in power calculation of the APSDs

For the localization of the peak and the boundary bins, the APSDs are smoothed by a Gaussian kernel to eliminate discontinuities caused by the presence of sidelobes. The boundaries are selected from the local minimums of the APSD at which the first derivative is positive and the closest to the peak.

As a result of the decrease of SNR of the detector signals at high frequencies, background removal is essential to the accurate estimation of the peak power. In the APSDs of the signals, the background around the peaks shows an asymptotic behavior that can be approximated by an exponential function of the distance in the number of bins, with respect to the peak's maximum amplitude. Therefore, the background in the APSDs is

determined by fitting it to a function in the form:

$$\log(P_k) = af_k + b \tag{5.2}$$

where P_k is the power at the bin k and f_k is the frequency of the bin.

The fit is applied respectively on the left and right side boundaries of the peak on two times the span of the peak width. The integrated value of the fit function within the peak range is subtracted from the peak power. If the fit fails due to uncommon noise behavior (fluctuations), the background would be estimated as the average power of the left and right boundaries.

An example of the fit results of the background noise in the APSDs of neutron detector and reactivity signal are shown in figure 5.7 (on the top) and figure 5.8. They correspond to the estimation of peak power at 32 Hz which is the frequency of the modulation. As shown by the figures, the noise amplitude is at least 2 orders of magnitude lower than the peak. However, the baseline of the background fit is still affected by the selected frequency range. The methodology of background determination should be investigated in future work for the optimization of the uncertainty due to background noise. It should also be noted that, harmonics higher than the 5^{th} order appear in the APSD of the reactivity signal. This suggests a potential bias in the reactivity reconstruction process.

The peak identification procedure of CPSDs is similar to that of the APSDs. In contrast, we are only interested in the local maximums of the peaks as the QOI are the phase differences. The phase differences are nothing but the arguments of the complex-valued CPSD at the local maximums. We may emphasize the importance of using an integer number of modulation periods as window length in the peak localization. Otherwise, the phase value would be biased if the modulation frequency falls between 2 bins.

5.2.3 Measured power in model-based reactivity worth

As discussed in section 5.1, the reactivity profile of PISTIL is approximated analytically by a function of the angular position, in the form of a sum of sine waves. The fit results are compared to that of the measured power of the APSD of reactivity signals to verify the Fourier decomposition of equation (5.1).

Figure 5.9 (left) shows the reconstructed reactivity signal profiles in the rotations at 0.5 Hz and 2 Hz, calculated with the measured position data and the reactivity calibration. Their APSDs are shown in Figure 5.9 on the right side. The calculated APSDs of these signals have much more spectral components than the expected 5 harmonics of the calibration, which is not the case for an ideal constant speed rotation shown in figure 5.3.

They are produced by the fluctuation of the speed of the rotation that has a non-zero mean due to the PID control mechanism of the NC.

Figure 5.10 corresponds to the error of the speed of rotation of PISTIL in time estimated using the first derivation of the motion signal. Despite an overall periodic motion, with in each cycle there is a variability of the speed which distorts the reactivity signals.

Additional information on the motion data can be found in appendix A.1. The extra harmonics in the APSD of reactivity signal are not analyzed: as they are not observed in the APSDs of detector signals, they are considered as artifacts. Nevertheless, it is worth verifying that the peak power of the fundamental in the APSD of reconstructed signals have consistent reactivity value between experiments of different frequencies.

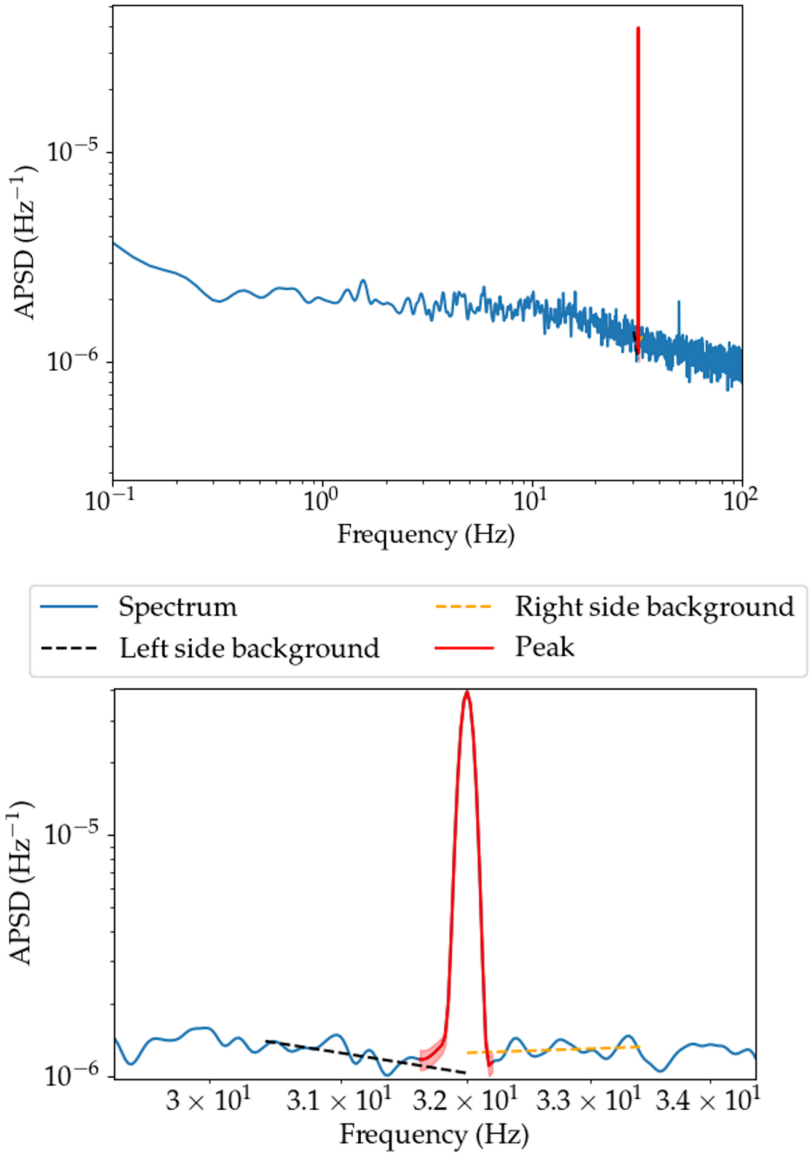

Figure 5.7: APSD of neutron detector signal in the case of a modulation with a fundamental frequency at 32 Hz on the top (sampled at 1 kHz, window size of 10000 samples for an acquisition of 40 minutes) and noise subtraction from the APSD peak power on the bottom

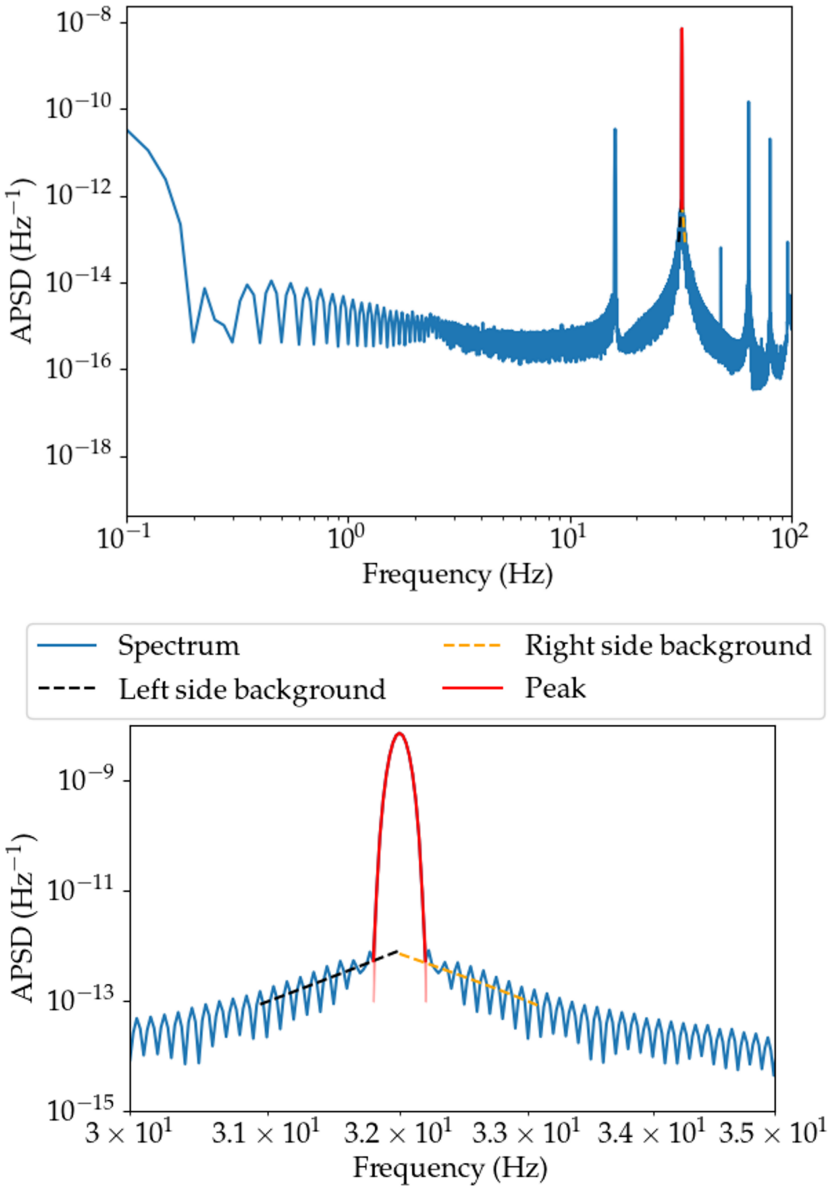

Figure 5.8: APSD of reactivity signal in the case of a modulation with a fundamental frequency at 32 Hz sampled at 1 kHz, window size of 10000 samples for an acquisition of 40 minutes

Figure 5.11 shows the estimated reactivity amplitude of the fundamental frequency of the modulation from the APSDs of the reactivity signal. The mean value of the measurements is indicated by the black line. Its value is consistent with the calibrated ones in table 5.2. The shaded area in figure 5.11 represents the dispersion of the data between measurements and detectors.

The majority of the measurements shows agreement with the dispersion of the peak

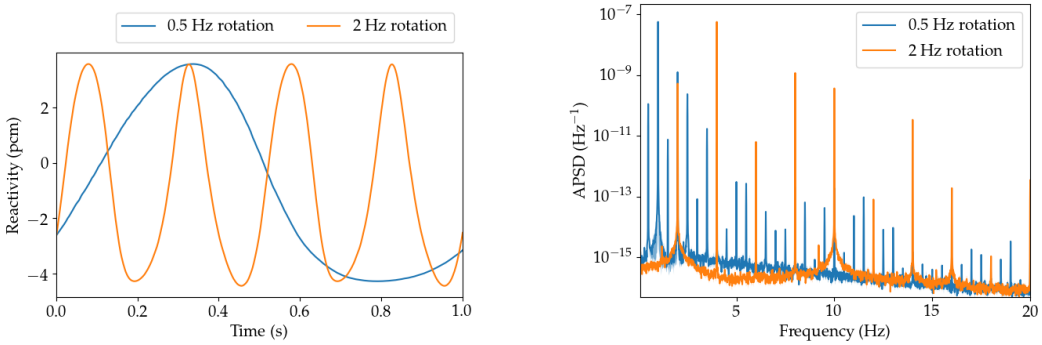

Figure 5.9: Reconstructed reactivity signals for 0.5 Hz and 2 Hz continuous modulation (left) and the corresponding APSDs (right)

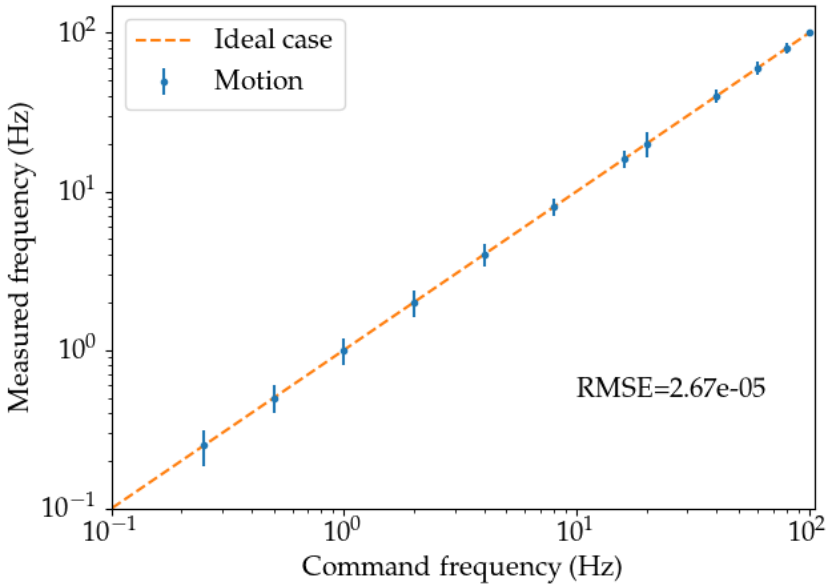

Figure 5.10: Comparison between command rotation frequency of PISTIL and measured frequency in continuous experiments

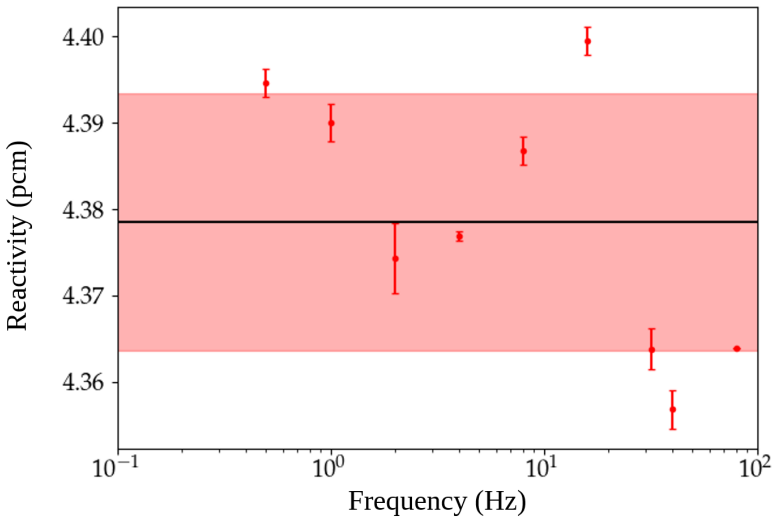

Figure 5.11: Reactivity obtained from the fundamental frequency of the modulation calculated using the reactivity signal APSDs, the shaded area represents the dispersion of the data between measurements and detectors.

power within 1σ. The dispersion of 0.15 pcm may arise from the motion pattern (linear profile in angular position) that is not reproduced exactly in the same manner by the motion control, thus distorting the reactivity profile from cycle to cycle.

5.2.4 Correction of anomalies

5.2.4.1 Noise in detection signals

In several experiments, an unexpected noise appeared in the raw voltage signal around 1 Hz which resulted in a broadened noise peak between 1×10^{-2} to 10 Hz in the APSD, as shown in figure 5.12. This noise appeared in the signal of the neutron detectors 3 and 4, and no similar noise is observed in the signals of detectors 1 and 2. Therefore, instability of the shared HV of the pre-amplifier of detectors 3 and 4 is suspected to be the cause of the noise. After verification of the data from each single experiment, this issue were occasionally observed starting from 2021 June 7^{th}. Consequently, 6 neutron detector signals affected by the noise frequency are rejected.

5.2.4.2 Desynchronization of the acquisition systems

The CRIO acquisition system was programmed to operate in RT (with a 400 MHz internal clock) to ensure the acquisition rate of the PC signals at 1 kHz. This was however not the case on PISTIL's side. Its nominal servo frequency was 1 kHz, but the real time operation was not supported. There is a possibility that the sampling rate of the two systems are distinct.

In consequence, after the initial synchronization to initiate the acquisition, a desynchronization between the internal clocks of the two systems occurs. The amount of data

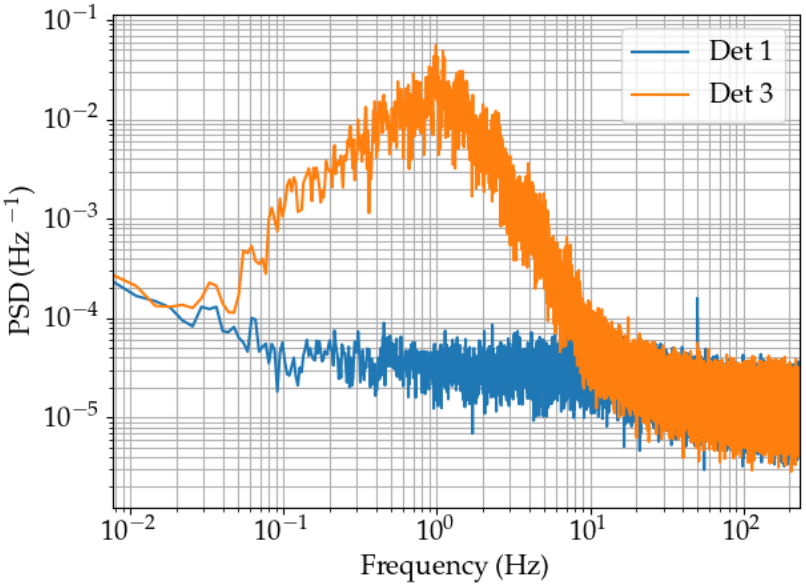

Figure 5.12: Comparison of APSD between detector 1 (without noise) and detector 3 (with noise) of the background noise measurement

acquired become unequal with the increase of the acquisition time. The desynchronization had an impact on the phase delay calculation using the CPSDs. A deviation of the phase delay is observed in the experimental data when analyzing the phase delay on successive portions of experimental data in chronological order. By calculation of the phase value of different segments separately, a quasi-linear increase of the phase value is identified, as shown in figure 5.13. With the information of the phase observed in each segment, it is possible to correct the bias of the calculation by an estimation of the phase evolution as compared to the initial value at the moment of the synchronization.

Assuming a constant difference in the sampling rates, we can estimate the difference of sampling rate $\frac{dN}{dt}(\text{samples.s}^{-1})$ as:

$$\frac{\text{Total difference of samples}}{\text{Samples per period of modulation}} = \frac{\Delta N}{f_{sampling}/f_k} \tag{5.3}$$

$$= \frac{\frac{dN}{dt} \cdot T}{f_{sampling}/f_k} \tag{5.4}$$

$$\tag{5.5}$$

This ratio is converted to the total phase deviation $\delta\phi$ by considering that it is equivalent

to a phase shift:

$$\delta\phi = 2\pi \cdot \frac{\frac{dN}{dt} \cdot T}{f_{sampling}/f_k} \tag{5.6}$$

$$\frac{1}{2\pi}\frac{\delta\phi}{T}\frac{f_{sampling}}{f_k} = \frac{dN}{dt} \tag{5.7}$$

$$\rightarrow \frac{dN}{dt} = \frac{f_{sampling}}{f_k}\frac{\tau}{2\pi} \tag{5.8}$$

where τ is the slope of the delay (rad.s^{-1}), T is the total duration of the acquisition, $f_{sampling}$ is the nominal sampling frequency (1 kHz) and f_k is the frequency of the modulation.

The sampling rate difference is estimated for the fundamental modulation frequency of continuous rotation experiments. It consists in calculating the slope of the phase delay from successive windows of the signals in chronological order. The phases are unwrapped to account for the modulo 2π value of the phase in the motion signal, which obscured the detection of the delay. The delay estimation is conducted for data from different experiments. The delay was evaluated to be between 0.030 and 0.035 samples. s^{-1}. As the CRIO functions in real-time, it is possible that the loop rate of the numerical control had a slight drift from its nominal value to about 1000.03 Hz. The value of the delay is then most accurately estimated with the data of modulations at 160 and 200 Hz thanks to the large number of windows for the fit of the slope of the delay. It is observed that the delay estimated with different experiments are not identical. As shown in figure 5.13, for two 200 Hz modulation measurements, the phase delays are different, which indicates that the exact value of the sampling rate difference varies from experiment to experiment. This led to applying a case-by-case correction factor to the calculated phase of the CPSDs.

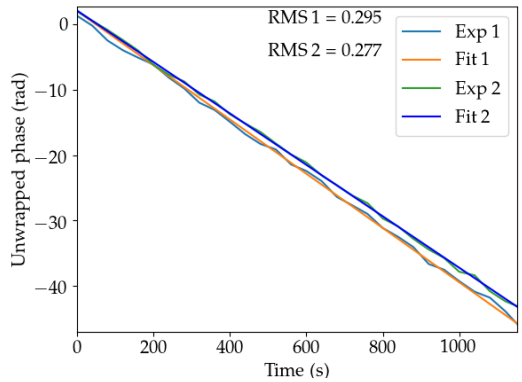

Figure 5.13: Unwrapped phase delay of neutron signal and motion signal in two 200 Hz continuous experiments and the fitted linear phase decrease

5.3 Results of the ZPTF in amplitude

In this section we discuss about the amplitude measurement results which are the ratio of APSD peak power of the neutron detector signal and the reactivity signal. For clarity,

results using JEFF-3.3 library based calibration are shown for discussion. The results using ENDF/B-VII.1 can be found in Appendix E.

5.3.1 Amplitude of continuous mode experiments

For each type of experiment and measured frequencies of the ZPTF, at least 2 repetitions of each experiments are conducted. The responses of each detector are analyzed separately for verification of data consistency and possible anomalies in the data. Figure 5.14 illustrates the peak power of 13 modulation experiments with fundamental frequencies ranging from 0.5 Hz to 200 Hz.

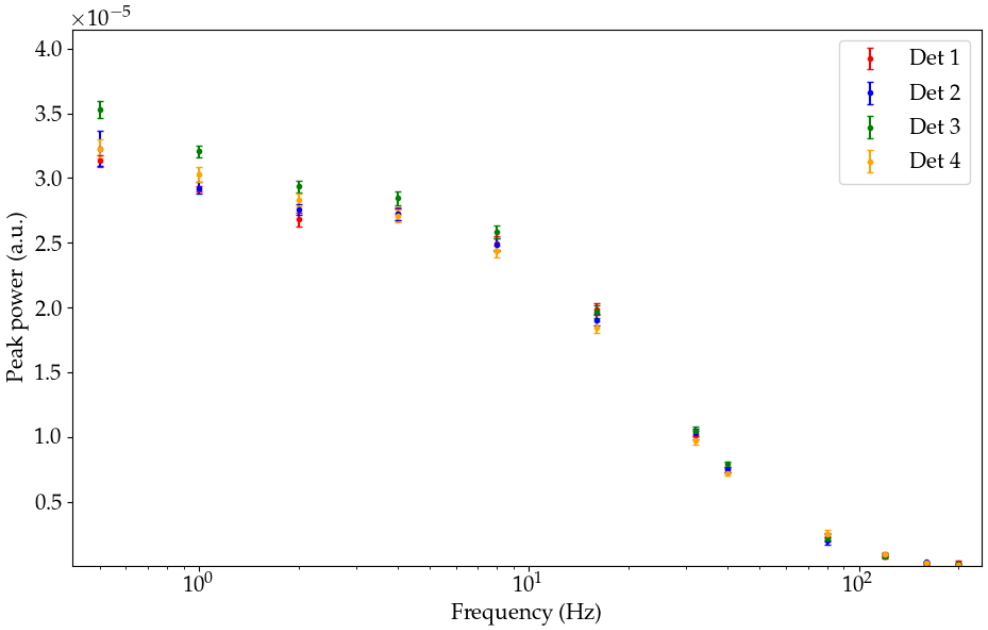

Figure 5.14: Peak power in the fundamental frequency peak measured in various continuous modulation experiments

There is a trend in the relative order of peak power between detectors in the results. The detector 3 gives peak powers 8-11 % higher than the others in the majority of the experiments. Figure 5.15 and figure 5.16 show a comparison between the measured peak power between the four neutron detector signals for different experiments and the mean value of the four measurements. The values in each row are at the same frequency and normalized to that of the mean value of the detector 1. The peak power for each detector shows that the measurements are repeatable, as the intra-class variance is compatible with the variance of every single measurement. The data at frequencies higher than 120 Hz had experimental uncertainties considerably higher than the other measurements due to the low peak power. As will be discussed in section 5.5.1, their values were not compatible with the calculated values using the theoretical formula of the ZPTF.

The mean value of the measurements by the 4 detectors and the propagated uncertainties are represented by the shaded area in figure 5.15 and figure 5.16. The values of

measured signal power are consistent as compared to the average values, which confirms the reproducibility of the experiments.

A possible explanation of the difference between detectors is the influence of spatial effect [109] in the ZPTF measurement. It remains to be verified in future works. Since there is no argument to privilege the results obtained with one detector, the estimation of the power are calculated as the mean of the power of detector signals for each experiment. The measured values in the 2-3 repetitions of experiments were then averaged and the uncertainty was estimated as the quadratic sum of the dispersion of the data and the uncertainty of each measurement to take into account the differences in the measurements.

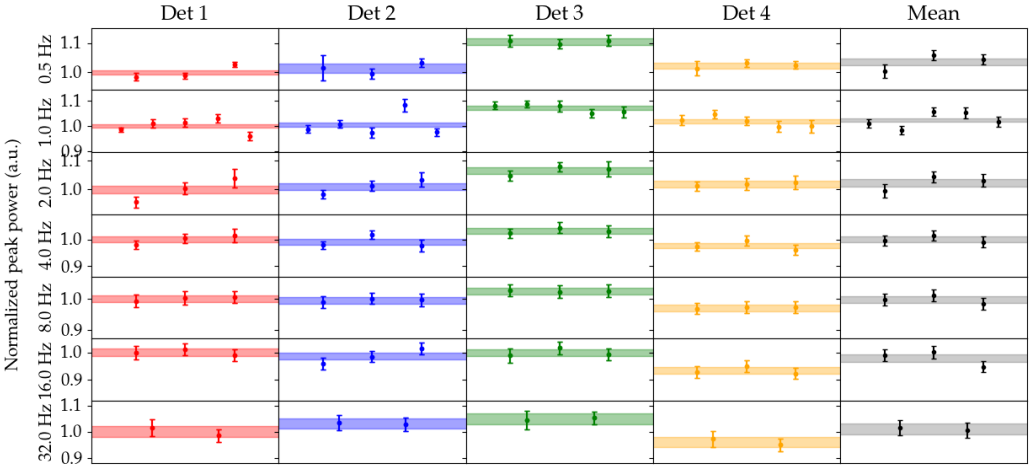

Figure 5.15: Uncertainty of the measured peak power at 2, 4, 8, 16 and 32 Hz for neutron detector signals

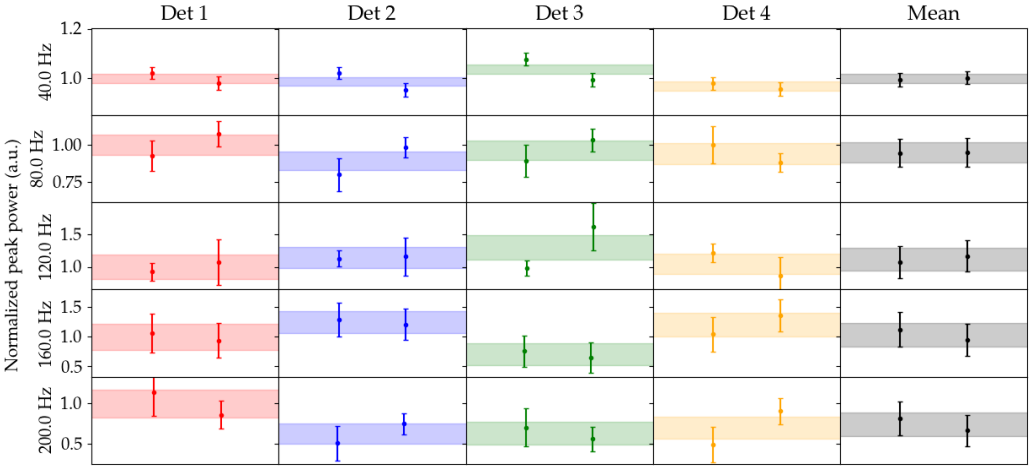

Figure 5.16: Uncertainty of the measured peak power at 40, 80, 120, 160 and 200 Hz for neutron detector signals

5.3.2 Amplitude of step-wise mode measurements

Before the presentation of the result, it should be noted that the prospected n-sequence with 5 bits has no even order harmonic components due to its anti-symmetrical shape. However, for the motion of PISTIL, the last step of the sequence is omitted in every period due to the implementation of the motion command. This modifies the total steps from 62 to 61 and the expected APSD shape. Figure 5.17 gives a comparison of the obtained APSDs and the theoretical predictions with the last step subtracted. As indicated in the figure, the peak powers are located at the expected frequency bin. It can also be seen that the even harmonics are present in the APSDs, although their amplitudes are low as compared to that of the odd ones.

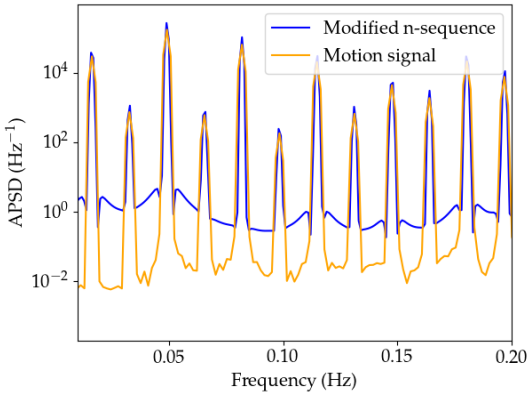

Figure 5.17: APSD of measured step-wise reactivity signal and theoretical predictions

Figure 5.18 presents the overall peak power variation of neutron detector signals as a function of the harmonic order for the three sequences, that differ only in the unit step size: 1 s, 2 s and 10 s.

For each one of them, the powers are normalized respectively by the power of the fundamental frequency. As shown by the figure, the harmonics' behavior is consistent between the 3 series, independently of the base step duration. The order of magnitude of the powers share a similar trend as a function of the harmonic number. The 17$^{\text{th}}$ harmonic shows large discrepancy in value as compared to its neighbor frequencies and an important uncertainty, which is also consistent for the 3 series. This confirms that the implementation of the step-wise motion induces identical reactivity modulation with a difference of frequency. The uncertainty also increases to an excessive level (nearly 100%) for harmonics higher than the 50$^{\text{th}}$. This behavior is related to the inherent mathematical property of the n-sequence: it has a drastic power decrease near the multiple of the sequence length, which is the harmonic of order 61 in the current study.

5.3.3 Analysis

As the position signal of PISTIL presents little fluctuations, the uncertainty associated to the estimation of reactivity peak power in the continuous rotation is as low as 0.001 % in the spectral analysis. The peak power estimation is conducted at the fundamental for continuous experiments.

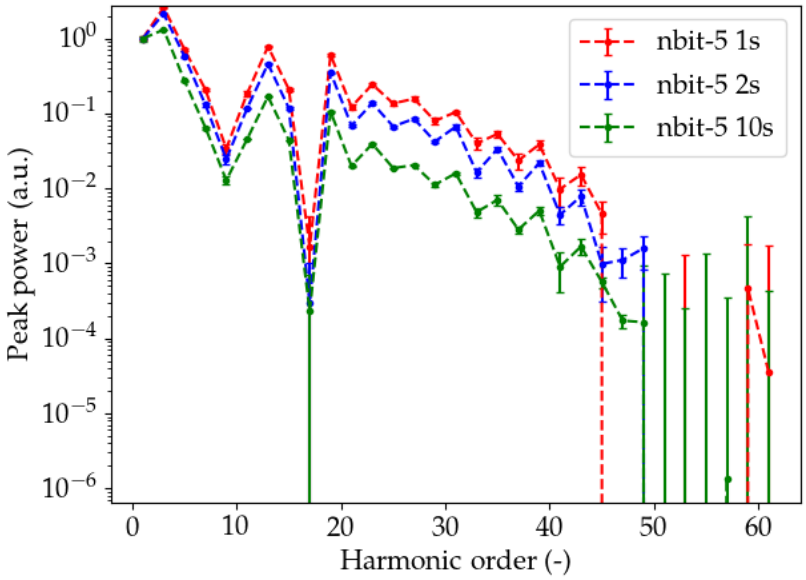

Figure 5.18: Peak power of detector signals in the harmonics of step-wise experiments with 1, 2 and 10 s unit step, the powers are normalized using the one at the fundamental frequencies

As shown in table 5.4, with the increase of the modulation frequency, the uncertainty is reduced with the increase of the number of windows and the consequent variance reduction.

The first 50 harmonics are estimated in the step-wise case and the data of other harmonics are discarded for the analysis. This consideration is made because the peak power of the 50 $^{\text{th}}$ harmonic is approximately 1% of the power of the fundamental, which leads to low SNR and relative uncertainties of 30 - 40 %. Typical values of the estimated peak power distribution of the aforementioned harmonics can be found in table E.12. Due to lower modulation amplitude in each harmonics as compared to the fundamental in the continuous cases, the relative uncertainty of the peak power in neutron detector signals is significantly higher. Additionally, there are difficulties in the determination of the boundaries of the peaks due to the frequency resolution.

With the increase in step duration, the minimum of the measured fundamental modulation frequency is 1.64×10^{-3} Hz. As discussed in section 5.2.1, the width of a peak is at least 5 frequency bins. Therefore, the minimum window size of the FFT is 5 integral periods of the modulation, which corresponds to the experimental data of 3050 s acquisition. The duration of acquisitions is approximately 7200 s for this kind of experiments, with the first 10 minutes of the acquisition considered as a transitional period of delayed neutron kinetics. This leads to the averaging of two PSDs in the Bartlett's method. The variance reduction is thus limited and the uncertainty estimation methodology is surely biased. The lack of frequency resolution makes the peak at the fundamental frequency more complicated to be distinguished from background noise, as compared to other harmonics. As shown in table E.13, the uncertainty of the fundamental peak power of the detector response is considerably higher than the 3$^{\text{rd}}$ and 5$^{\text{th}}$ harmonics.

Table 5.4: Example cases of peak power estimation at the fundamental frequency for continuous rotation experiments

	Reactivity (JEFF-3.3)		Neutron detector	
Frequency (Hz)	Power (-)	σ (-)	Power (-)	σ (-)
0.5	1.93×10^{-9}	6.00×10^{-13}	3.28×10^{-5}	8.84×10^{-7}
1	1.93×10^{-9}	1.27×10^{-12}	3.02×10^{-5}	4.53×10^{-7}
2	1.91×10^{-9}	1.84×10^{-12}	2.80×10^{-5}	4.84×10^{-7}
4	1.91×10^{-9}	1.74×10^{-13}	2.75×10^{-5}	4.67×10^{-7}
8	1.92×10^{-9}	1.01×10^{-13}	2.50×10^{-5}	4.80×10^{-7}
16	1.93×10^{-9}	7.98×10^{-12}	1.92×10^{-5}	4.79×10^{-7}
32	1.91×10^{-9}	2.97×10^{-12}	1.02×10^{-5}	3.21×10^{-7}
40	1.90×10^{-9}	7.42×10^{-13}	7.51×10^{-6}	1.86×10^{-7}
80	1.90×10^{-9}	1.40×10^{-13}	2.25×10^{-6}	2.79×10^{-7}
120	1.87×10^{-9}	6.07×10^{-14}	8.65×10^{-7}	1.07×10^{-7}
160	1.87×10^{-9}	6.31×10^{-14}	2.70×10^{-7}	7.64×10^{-8}
200	1.94×10^{-9}	5.10×10^{-14}	2.05×10^{-7}	7.10×10^{-8}

The results of all the ZPTF amplitude measurements are shown in figure 5.19. The numerical values are estimated as the mean of the measurements. A total of 38 experiments are included for the estimation. The uncertainties are estimated as the RMS value of the dispersion between detectors and experiments. In the experimental design, it was desired to have overlaid harmonic frequencies of different experiments as a cross-check of the repeatability of the experiments. The amplitude values in the frequency range between 8 mHz and 1 Hz, where there are the overlaid harmonic frequencies are shown in the zoomed part of figure 5.19. The measurements are consistent between continuous and step-wise data: for instance, the difference in two amplitudes measured at 0.508 Hz and 0.5 Hz is 6.16 ± 5.21.

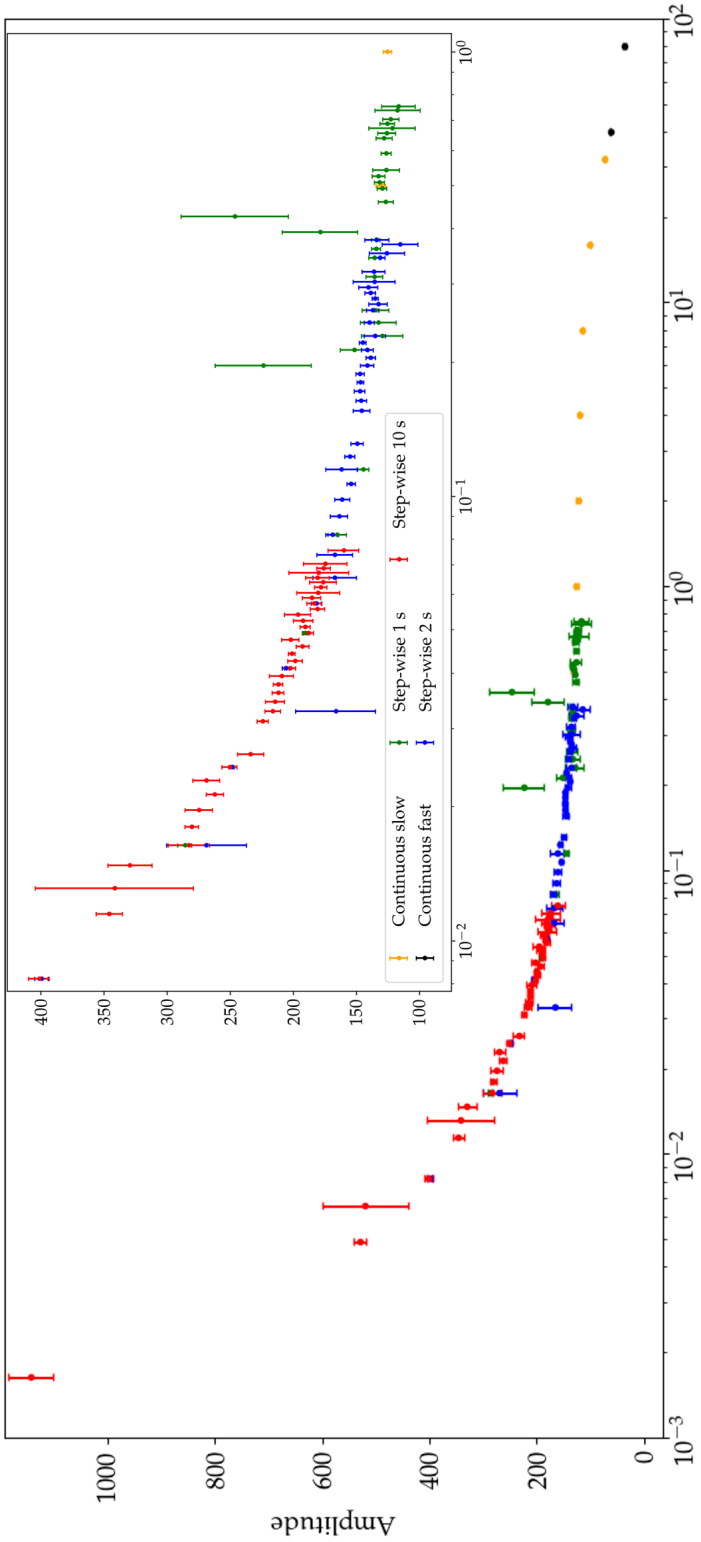

Figure 5.19: Results of the measurement of ZPTF amplitude of CROCUS in continuous and step-wise experiments and zoom on the low frequency range between 0.01 and 1 Hz

5.4 Results of the ZPTF in phase

5.4.1 Equivalence between motion and reactivity signals

Figure 5.20 shows a superposition of the frequency domain distribution of the CPSDs between neutron detectors. As expected the CPSD peaks coincide with the frequency bin of the APSD peaks. The phase information in the CPSDs is determined at the same frequencies as in the peaks of APSDs.

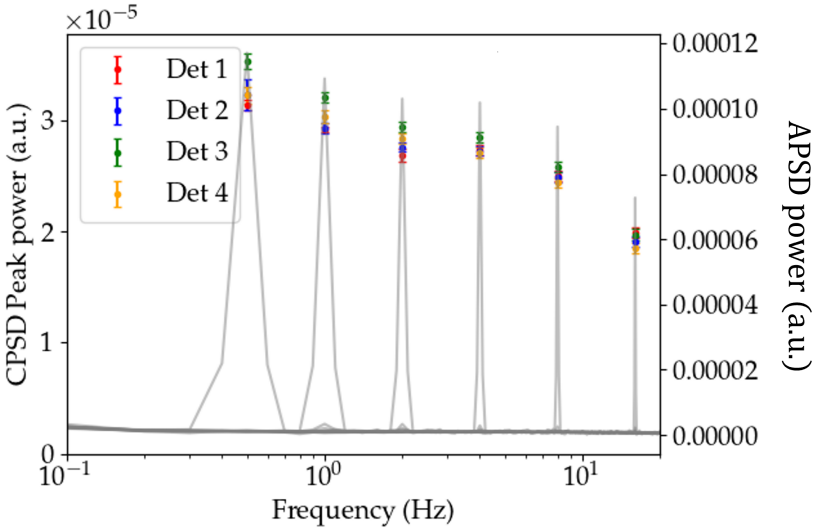

Figure 5.20: Measured CPSD peak power between detector 1 and detector 2 (in grey) and APSDs peak powers of all detectors

Difficulties arise in the estimation of the phase delay between the reactivity signal and the detector signals. Figure 5.21 consists in a measured phase delay of a step-wise experiment of 1 s unit time interval. For the sake of clarity, the shown values are at frequencies where the CPSD amplitude was at least two times the background.

As indicated by the values in figure 5.21, the phase measurement is much more susceptible to noise and distortion than the peak power calculation due to the fact that the phase is random everywhere but at the harmonics of the modulation.

The reactivity signal is reconstructed and the four reactivity calibrations do not have the same phase values. However, within the PK approximation, the reactivity signal measured with the neutron detectors should be synchronized. This could be caused by numerical issues or the presence of spatial effects which are difficult to be confirmed due to the precision of the measurements. Therefore, the reactivity signals are not used for the phase estimation.

For the continuous rotation, the motion signal consists of a succession of rising ramps. When the rotation frequency varies, the phase difference between these reactivities and the motion signal is constant as the correspondence between the angular position and the reactivity worth does not vary. Instead of using the reactivity signal, the CPSD of the motion signal and detector signals are computed. Nevertheless, this would introduce a

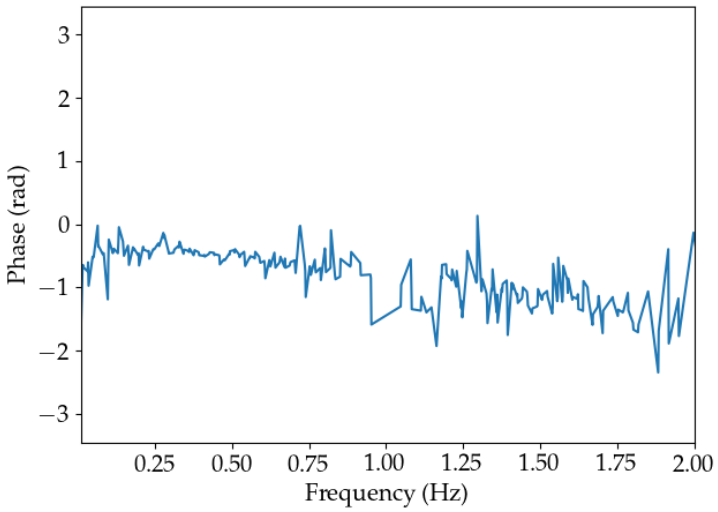

Figure 5.21: Phase of the CPSD of the motion signal and the neutron detector (det 1) signal of a 1 s unit time step-wise experiment; the signal is sampled at 1 kHz during 60 minutes, analyzed with a window size of 3.05×10^5 samples

constant shift in the measured phase values and the results can only be interpreted as a relative difference profile.

The reactivity signal of the step-wise experiments is almost equivalent to the motion signal. The CPSDs are also computed using the motion signal for the same consideration as the continuous case. The measured phase values in the step-wise case exhibits an oscillatory behavior. The phase of the low order harmonics has relatively consistent values as compared to the theoretical predictions, while several of the harmonics had positive values or large uncertainties. Similar to the considerations adopted for the amplitude measurements (described in section 5.3.2), the estimation was made on the first 50 $^{\text{th}}$ harmonic. A criterion to discard the analysis of a certain harmonic is the uncertainty in the CPSD peak amplitude: peaks with large uncertainty has inconsistent phase value as compared to those of the neighbor harmonics ("jumps"). It is on the contrary of a continuous evolution trend as described by the ZPTF mode.

5.4.2 Phase of the step-wise mode measurements

Figure 5.22 shows the results of the ZPTF phase measured by the step-wise experiments. The measured frequencies range from 1.64×10^{-3} Hz to 0.8 Hz, which are respectively the fundamental frequency of a 5 bit n-sequence with a unit step of 10 s and the 50 $^{\text{th}}$ harmonic of a 5 bit n-sequence with a unit step of 1 s. The phase values at neighboring frequencies of the modulation show compatible values. This is potentially because there is limited impact of the acquisition issues on low frequencies: using the current correction method, a delay of 0.03 samples. s^{-1} would require a phase correction of less than 0.002 rad at the fundamental frequencies for an acquisition of 3600 s.

Compared to the amplitude measurements, the number of rejected harmonics is lower. Despite the low peak power of the even harmonics, the measured phase did not show oscil-

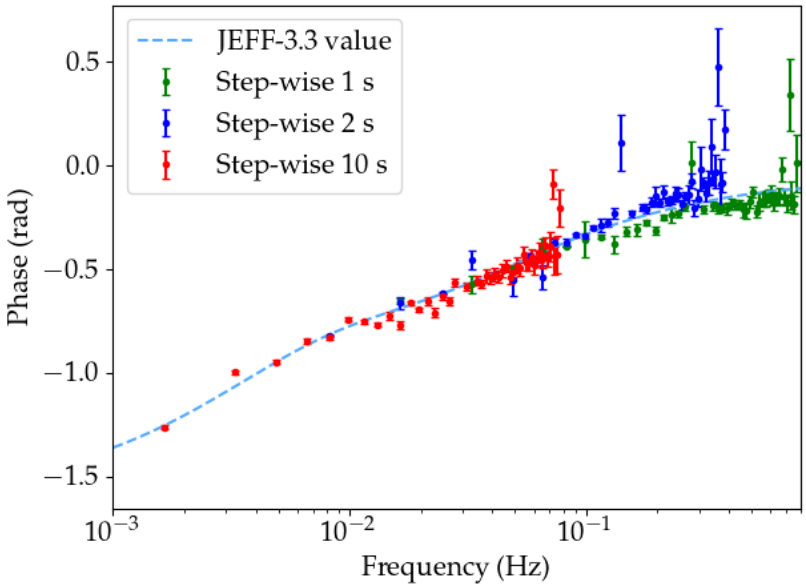

Figure 5.22: Measured phase delay in the case of step-wise experiments between motion and neutron detector signals

lation in the value as compared to the neighboring odd harmonics with the exception of 4 to 5 above the harmonic order of 25) as opposed to the case of the peak powers. The possibility of using different analysis approach in the signal processing might be investigated, as the power and phase show different spectral behavior. Alternative windowing methods as well as autoregressive-moving-average model should be considered for background noise reduction. The bootstrapping technique applied to modulation, as detailed in [95], can be used for such investigation.

5.4.3 Phase of the continuous mode measurements

As the neutron detector signals are in phase, the difference of the value between the measurements of the four detectors are low, as well as the uncertainty in each measurement of the detector. For continuous experiments, the phase value average per experiment is given in Figure 5.23. However, the discrepancies between experimental data at the same frequency are not covered by the 3σ uncertainty and are dispersed. A maximum dispersion of 1.06 rad is observed at 120 Hz. The poor repeatability of the measured phases may be attributed to the limits in the phase correction model. The calculated phase for each window of the signal had oscillations that caused the linear fit in order to have increased uncertainty and insufficient correction.

The theoretical predictions of the ZPTF phase using the kinetic parameters computed with JEFF-3.3 data are given as an indication. It is expected that the phase measurements have discrepancies with the calculation (of relatively stable value) due to the use of the motion signal in the CPSD computation. However the measured phase values do not show a regular trend between measurements for all adjacent frequencies. Strong oscillations are observed in the values, such as the measurements at 80 and 120 Hz. The agreement of the

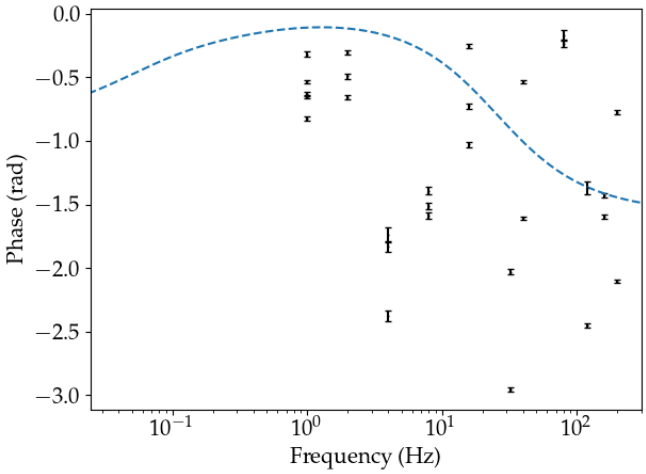

Figure 5.23: Measured phase delay in the case of continuous rotation motion experiments and neutron detector signals, the calculated value using JEFF-3.3 data is given as an indication (in blue)

measured phase with the theoretical values and the aberrant behavior of almost half of the measurements make it difficult to consider the phase delay estimation as valid results.

5.5 Comparison of measurements with theoretical predictions

5.5.1 Direct comparison

The measured amplitude and phase values of the ZPTF are compared to the predictions with kinetic parameters using JEFF-3.3 and ENDF/B-VII.1 libraries. The comparison results are given in figure 5.24 and figure 5.25 respectively. There is an increasing discrepancy with the rise in frequency as compared to theoretical predictions of both libraries. Due to the high uncertainty, measurements above 100 Hz are not considered in the comparison.

The measured amplitude from the step-wise modulation experiments show good agreement with the models. Most of the measurements of the even harmonics of the modulation of the step-wise experiments are discarded for that the relative uncertainty is higher than 20%. The Root-Mean-Square Error (RMSE) of the amplitude and the phase of step-wise and continuous data as compared to calculations, are indicated in figure 5.24 and figure 5.25. ENDF/B-VII.1 data has lower RMSE value in the range above 0.5 Hz, which suggests privileging the computation of the prompt decay constant (i.e. the ratio between the delayed neutron fraction and the prompt neutron generation time). On the other hand, JEFF-3.3 library is more consistent with the measurement in the frequency range of interest for delayed neutrons (inferior to 0.1 Hz). This is also shown in the RMSE of phase values.

The estimated uncertainties of the phase in the step-wise experiments are an order of magnitude lower than the discrepancies with the theoretical predictions. Therefore, the

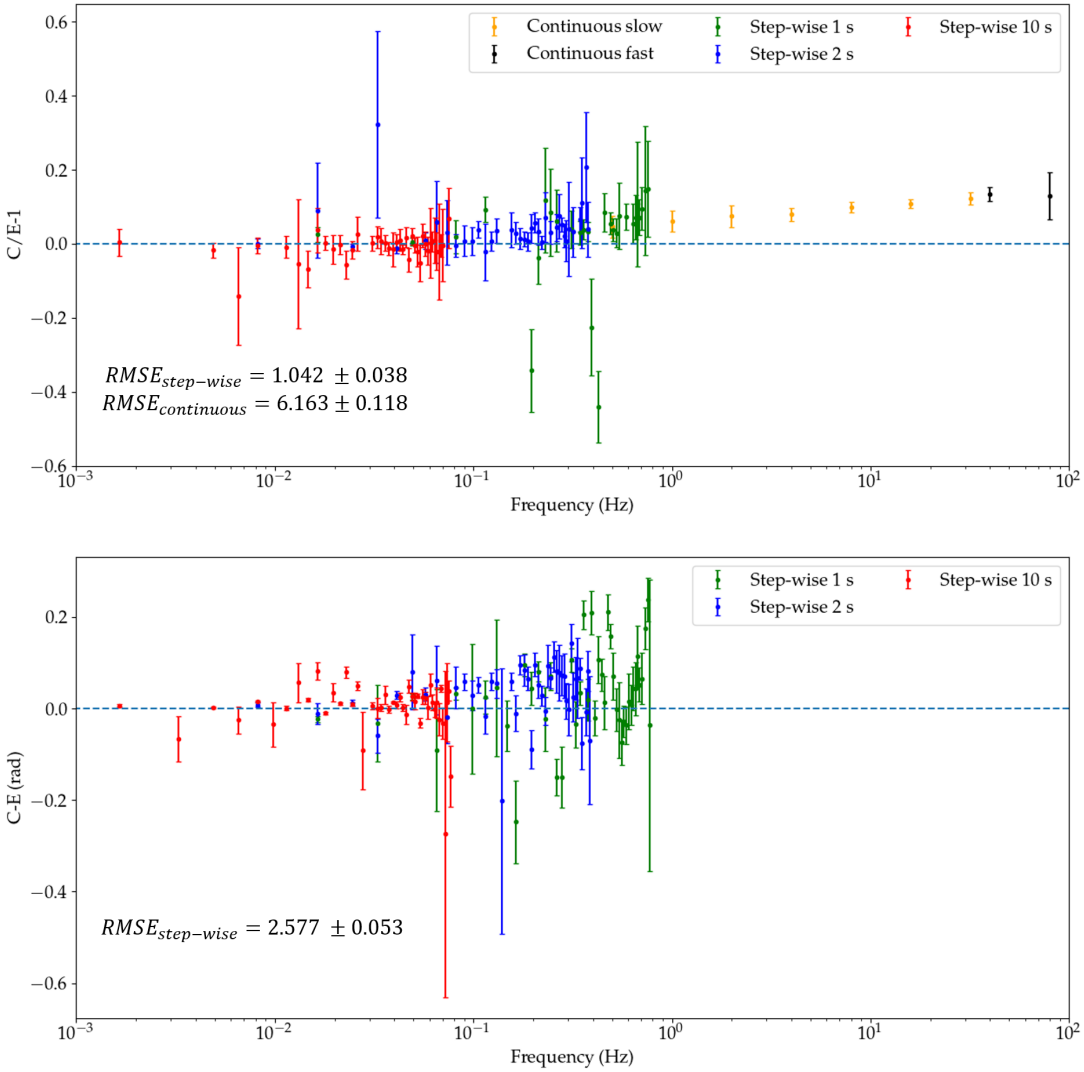

Figure 5.24: Comparison of the measured ZPTF amplitude (top) and phase (bottom) with JEFF-3.3 based calculations

RMSEs are significantly higher than the amplitudes for the low frequency range. The underestimation of the uncertainty can be explained by the limited duration of the acquisition (1-2 hours) and consequently the insufficient number of windows in the statistical estimation. Nevertheless, since the phase measurement is independent of the reactivity calibration, it can be used for the validation of the calibration results in future works.

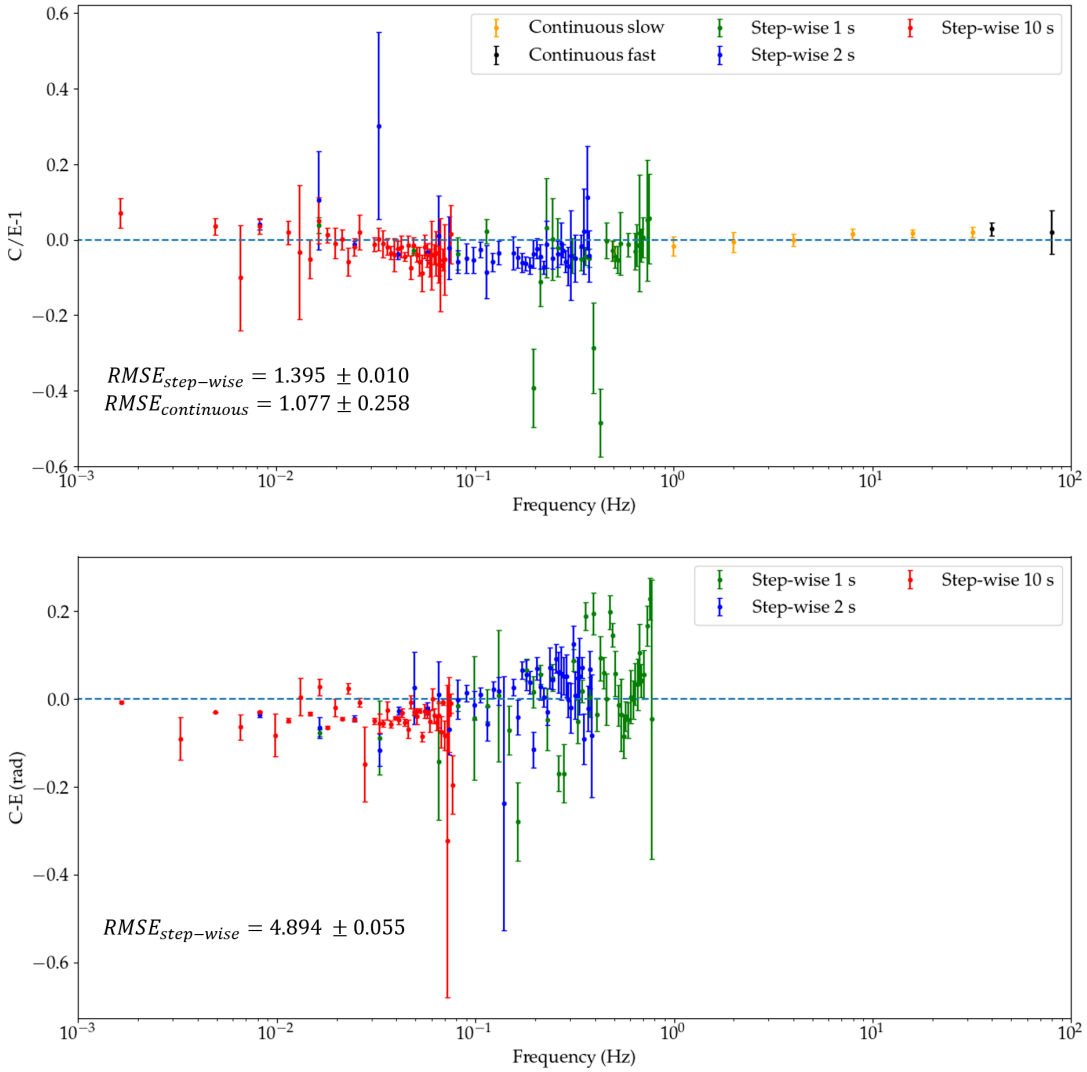

Figure 5.25: Comparison of the measured ZPTF amplitude (top) and phase (bottom) with ENDF/B-VII.1 based calculations

5.5.2 Reactor kinetic parameters

Through a fitting procedure, the measured ZPTF amplitudes and phases are used as input data to estimate the effective kinetic parameters. The non-linear least square fit model aims at minimizing the weighted sum of the square of the residuals with all the amplitude and phase data. Its general form is defined as:

$$R^2 = R_1^2 + R_2^2 = \sum_{i=1}^{N_1} \frac{1}{w_{1,i}} [||\ G\ ||_{exp,i} - M_1(f_i)]^2 + \sum_{i=1}^{N_2} \frac{1}{w_{2,i}} (arg[G]_{exp,i} - M_2(f_i))^2 \quad (5.9)$$

where R_1 and R_2 are respectively the sum of the weighted residual of amplitude and phase data. $w_{1,i}$ and $w_{2,i}$ are the weights corresponding to the variance of the measurement.

M_1 and M_2 are the ZPTF amplitude and phase model corresponding to equation (2.19) and equation (2.20):

$$M_1(f) = ||\ G(j2\pi f, \Lambda, \beta_{eff,1}, \beta_{eff,2}, ..., \beta_{eff,n}, \lambda_1, \lambda_2, ..., \lambda_n)\ || \quad (5.10)$$

$$M_2(f) = arg[G(j2\pi f, \Lambda, \beta_{eff,1}, \beta_{eff,2}, ..., \beta_{eff,n}, \lambda_1, \lambda_2, ..., \lambda_n)] \quad (5.11)$$

5.5.2.1 Constraints

The number of variables in the fit is library dependent. For ENDF/B-VII.1, as the decay constants of delayed groups are not fixed, the number of variable is 13 (Λ, λ_i and $\beta_{\text{eff,i}}$). With the delayed group formulation of JEFF-3.3, the number of parameters is reduced to 9 as the λ_i are fixed by definition.

It should be noted that the majority of the amplitude data and all the phase data are in the low frequency range, which is insensitive to the parameter Λ. It is necessary, with the present experimental dataset, to apply a constraint on $\alpha = \beta_{eff}/\Lambda$ for the fitting algorithm to converge. The constraint is set to $\alpha = \alpha_0$ where α_0 is the value estimated with TRIPOLI-4 calculation.

Difficulties also arise in fitting the λ_i and β_i simultaneously. This could be attributed to the non-linear term $\beta_{eff}/(\lambda_i^2 + \omega^2)$ in both the real and imaginary part of the ZPTF given by equation (2.17) and equation (2.18). It is decided to fix the λ_i in the ENDF-based ZPTF model to the values corresponding to those of CROCUS in TRIPOLI-4 calculation. The initial guess of the fit variables are selected randomly within a 50 % - 150 % range of the calculated values.

The comparison between ZPTF fit results and calculated values (the model curve in blue) are shown in figure 5.26 for the amplitude and figure 5.27 for the phase. The residuals of the fits are also given in the corresponding figure.

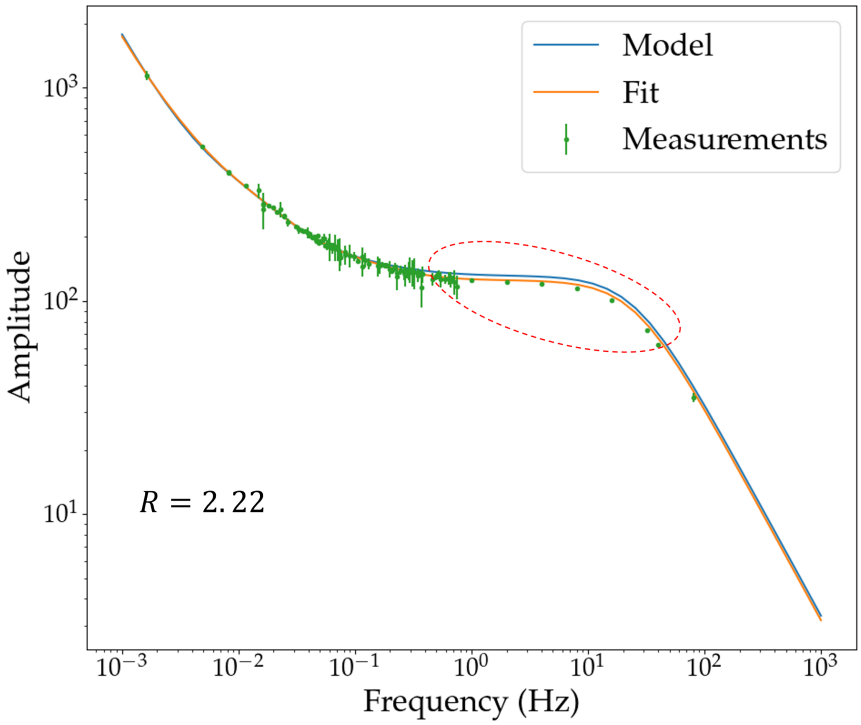

(a) JEFF-3.3

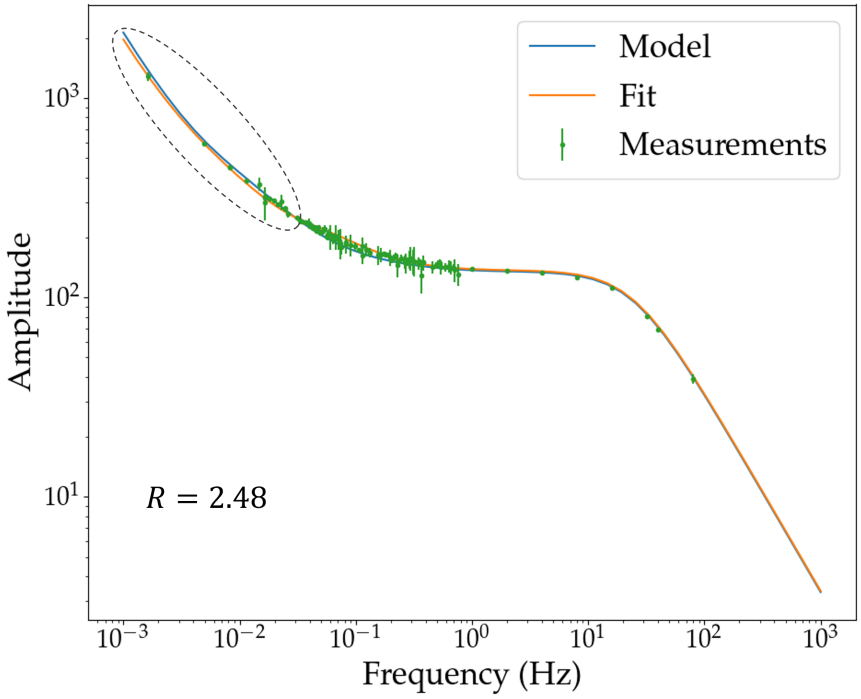

(b) ENDF/B-VII.1

Figure 5.26: Comparison between fitted ZPTF amplitude and calculated values using JEFF-3.3 (top) and ENDF/B.VII-1 (bottom)

5.5.2.2 Fitted ZPTF amplitude

As the value of α is constrained, the cut-off frequency of the fit is in agreement with the model for both libraries. No clear conclusion can be drawn from the profile above this frequency, as the amplitude values decrease asymptotically towards $2\pi f\Lambda$. In the intermediate frequency range (outlined in red in figure 5.26a), there is a much higher model-fit discrepancy in the JEFF-3.3 case as compared to the ENDF/B-VII.1 case. The fit curve is systematically below the model prediction. This is consistent with the C/E-1 values in figure 5.24, which indicates that the amplitude results in continuous experiments are lower than the JEFF-3.3 based calculations. In the low frequency range outlined in black in figure 5.26b, the deviation of calculated value from the fit curve is higher for ENDF/B-VII.1 case as compared to that of JEFF-3.3. This deviation is essentially caused by the discrepancy between calculated and measured amplitude in step-wise 10 s measurements as indicated in figure 5.25.

5.5.2.3 Fitted ZPTF phase

Similar to the amplitude case, the constraint on the prompt decay constant leads the fit curve to converge towards the model at high frequency. It can be seen that in the low frequency range (outlined in red), the aggregated phase delay of different groups is more consistent between calculation and measurement using JEFF-3.3 as compared to ENDF/B-VII.1. A large discrepancy is observed in the intermediate frequency range outlined in blue, due to the large uncertainty of the measurements and the lack of measurements at frequencies of continuous experiments. Complementary measurements in this frequency range could improve the fit quality.

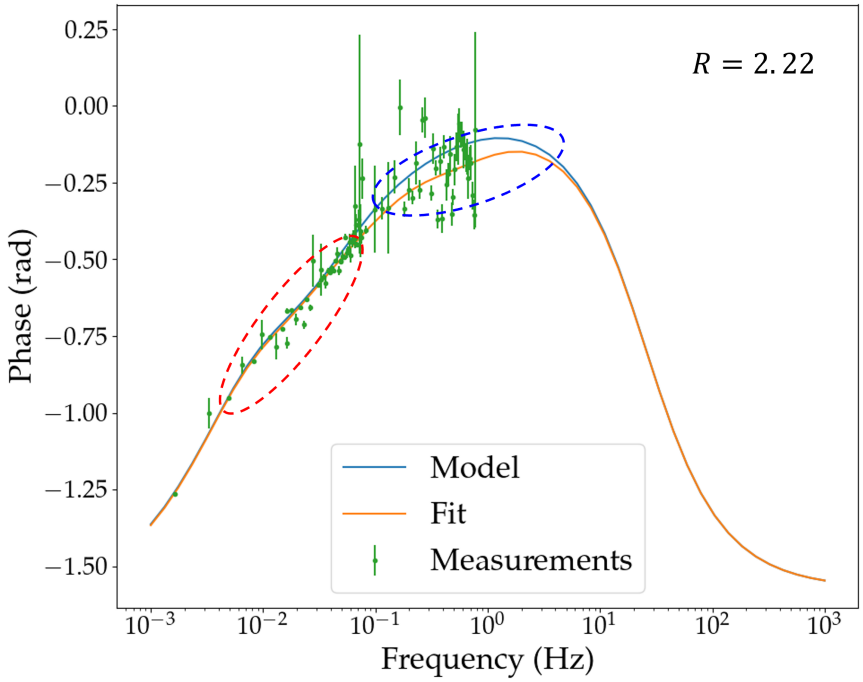

(a) JEFF-3.3

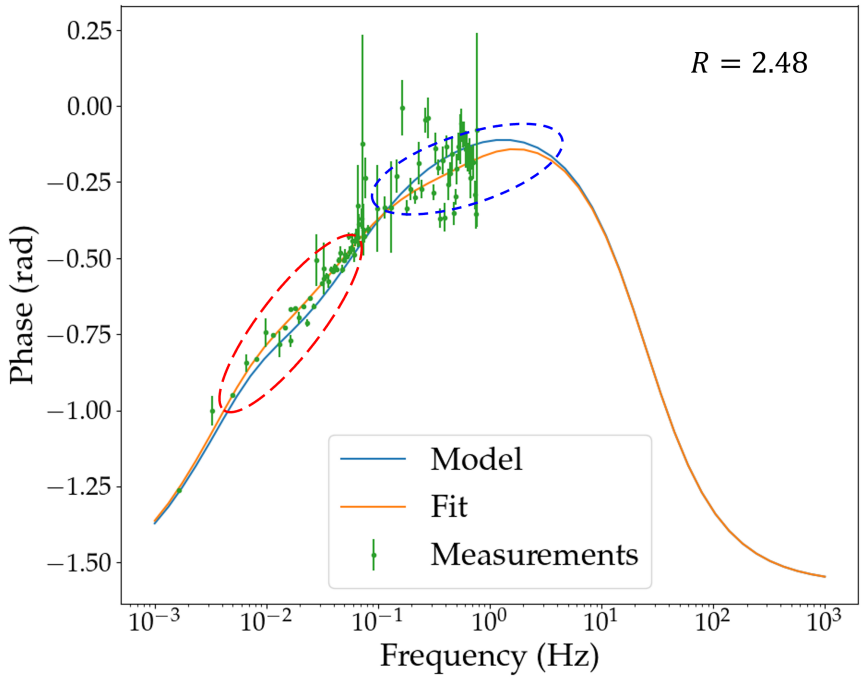

(b) ENDF/B-VII.1

Figure 5.27: Comparison between fitted ZPTF phase and calculated values using JEFF-3.3 (top) and ENDF/B-VII.1 (bottom)

5.5.2.4 Kinetic parameters

The effective delayed neutron fractions are obtained as variables of the fit. This results in a compensation effect between groups having their decay constants of same order of magnitude, which is illustrated in table 5.5 and table 5.6. They show the comparison between relative fractions of groups in computation and in measurement. The uncertainty of the fits which are of the order of 10^{-4} % are not given in the tables for the sake of clarity. The exceedingly small uncertainty indicates a potential numerical issue which should be investigated in future work.

The most notable compensation effect is shown by the 8^{th} group in table 5.5. This group is practically absent in the measurement, which caused by its low fraction (*a priori*) and large decay constant: its contribution is probably attributed to the 7^{th} group by the fitting algorithm.

Table 5.5: Calculated and measured relative fractions of effective delayed neutron groups using JEFF-3.3 based data (uncertainties of fitted fractions, of the order of 10^{-4}, % are not provided.)

Groupe	Decay constant (s^{-1})	Calculated fraction (%)	Fitted fraction (%)
1	0.01247	3.01 ± 0.03	5.54
2	0.02829	14.46 ± 0.07	3.36
3	0.04252	8.57 ± 0.05	17.51
4	0.13304	18.68 ± 0.08	14.57
5	0.29247	32.52 ± 0.11	33.45
6	0.66649	10.64 ± 0.06	5.92
7	1.63478	8.73 ± 0.05	19.73
8	3.5546	3.29 ± 0.03	$9.02\ 10^{-10}$

Table 5.6: Calculated and measured relative fractions of effective delayed neutron groups using ENDF/B-VII.1 based data (uncertainties of measured fractions, of the order of 10^{-4}, % are not provided.)

Groupe	Decay constant (s^{-1})	Calculated fraction (%)	Measured fraction (%)
1	0.01338	3.23 ± 0.02	4.31
2	0.03252	17.15 ± 0.07	17.02
3	0.12118	16.77 ± 0.06	20.40
4	0.30603	38.55 ± 0.08	29.01
5	0.85826	17.13 ± 0.06	14.39
6	2.88337	7.12 ± 0.05	14.87

The compensation effect indicates the insufficient number of experimental data for a non-linear least square fit. Additionally, the fit uncertainties of delayed group fractions are practically negligible due to high correlation between fit parameters. Alternative fit method, for instance the Bayesian fit, would allow to attribute more consistent uncertainties by taking into account the prior knowledge on kinetic parameters.

The value of integral observables corresponding to the fit results are shown in table 5.7.

The mean half-life of delayed neutron precursors, the $T_{1/2}$, is calculated as:

$$T_{1/2} = \ln(2) \sum_{i=1}^{N} \frac{\beta_{\text{eff,i}}}{\beta_{\text{eff}} \lambda_i} \tag{5.12}$$

The effective delayed neutron fraction β_{eff} is mainly determined by the mean value of the ZPTF amplitude in the intermediate frequency range: the "plateau" value is approximately $1/\beta_{\text{eff}}$. As the JEFF-3.3 based amplitude measurements are systematically smaller than the model prediction, there is a 5 % discrepancy between calculation and experimental results. The measured β_{eff} using ENDF/B-VII.1 based reactivity calibration, on the other hand, agrees with the calculation within the 1σ uncertainty of 0.75 %.

The $T_{1/2}$ reflects the mean contribution of delayed neutrons on the time constant of reactor kinetics. In this aspect, the JEFF-3.3 prediction is compatible with the value determined experimentally. This suggests that the 8-group formulation with the proposed decay constants is representative of kinetic characteristics of CROCUS. The agreement between calculation and measurement is less satisfactory for the ENDF/B-VII.1 case. There is a 6.8 % difference between calculation and measurements, which is expected as the amplitude and phase curve of the fit show some deviation from the model. It should be noted that the decay constants are fixed for the fit to converge. This could affect the validity of the 6-group model, as the original formulation does not define the decay constants but let them to vary freely in the fit. From a mathematical point of view, a fit with 12 parameters requires much more data than that with 8 parameters to reach the same convergence. A larger number of experimental data could improve the fit convergence when reasonable constraints are applied to decay constants. The generalization of the above statements for Uranium fueled light water reactor should be studied in future work.

Table 5.7: Calculated and measured integral observables using JEFF-3.3 and ENDF/B-VII.1 libraries

	ENDF/B-VII.1			JEFF-3.3		
	Calculated	Measured	C/E-1	Calculated	Measured	C/E-1
Λ (s)	47.502 ± 0.001	47.838 ± 0.280	-0.29 ± 0.58%	47.703 ± 0.001	50.037 ± 0.337	-4.75 ± 0.64%
β_{eff} (pcm)	737.2 ± 3.6	739.4 ± 4.2	-0.29 ± 0.75%	758.7 ± 3.7	796.5 ± 5.3	-4.75 ± 0.78%
$T_{1/2}$ (s)	7.31 ± 0.06	7.84 ± 0.14	-6.76 ± 1.84%	8.52 ± 0.05	8.45 ± 0.09	-0.81 ± 1.21%

5.6 Chapter summary

5.6.1 Experimental results

The continuous rotation and n-sequence like step-wise motion induced modulation allowed to measure the ZPTF of CROCUS between 1.6 mHz and 200 Hz. A reactivity calibration was carried out to provide normalization of the detectors' responses for the absolute measurement of the amplitude. This required a model to convert the motion signal to a reactivity signal. The calibrated maximum reactivity worth for the four detectors are slightly different, in the order of 0.4 pcm. Independent normalization was performed for

amplitude results of each detector, and the dispersion in values is taken into account in the uncertainty propagation.

The measured amplitudes in step-wise and continuous experiments show a good agreement within 1σ uncertainty, which is the goal of overlapping the modulation frequency of experiments. This overlapped range corresponds to frequencies sensitive to delayed neutron behavior.

The phase measurements in the step-wise experiments show good consistency between experiments and should provide a first base for further analysis. However, the measurements of the continuous experiments were discarded due to the lack of repeatability. The origin is identified as a quasi-linear bias of the measured phase. Its cause remains to be confirmed in future works.

The experimental data are used in a non-linear least-square fit to estimate the kinetic parameters. The measurements and the straight-forward fit does not give an estimation of delayed neutron group fractions with a reliable uncertainty estimate. Nevertheless, the resulting total delayed fractions as well as the mean precursor half-lives are consistent with simulation based values. Thus, the outcome of the current work support the application of the developed experimental methodology and the study of reactor kinetics using integral observables.

5.6.2 Recommendation for future work

5.6.2.1 Modulation profile

The step-wise motion profile used in the current study was a modified n-sequence, which actually increased the difficulty of the analysis due to the presence of all harmonic frequencies. Therefore, PSD peak identification required a high resolution to avoid peak overlap. There also exist other types of PRBS generator than the n-sequence. They could allow to obtain signals with equally distributed power and fewer harmonics (i.e, with lower requirements in resolution) to preserve a reasonable number of windows for the uncertainty estimation.

5.6.2.2 Synchronization of acquisition systems

The investigation and resolution of the source of the phase drift is necessary for measuring the phase delay in continuous experiments. It can be attributed to the fact that the numerical control of the motor is not real-time, or to its acquisition timing scheme, or possibly to a lag caused by the over-consumption of resources: parallel data communication, writing to file, UI commands. The data transmission was accomplished via User Datagram Protocole (UDP), which was the only option to avoid data loss. Using UDP, we are limited in the verification of the actual acquisition frequency. For synchronization of PISTIL with other systems, it would be ideal to use a RT numerical control. This would however require to use a different numerical control and to reprogram the motion control of the motor. An independent acquisition of the angular position (e.g. optical sensor, follower integrated to the motor) is a more viable option, which would allow the verification of the position given by the current numerical control.

5.6.3 Neutron instrumentation

The neutron detectors involved in the current work were installed as close as possible to the fuel zone within the water reflector. It was assumed that the PK approximation remains valid as seems the case in this first investigation, where no clear evidence of spatial effect induced phenomena is observed. It should also be noted that the four used neutron detectors are CFUL01 operated in current mode. Comparing different types of detector behavior in the same experiment may give different observation than the current case. A first approach could be the comparison of detector response with respect to several chosen positions and electronics.

It is envisaged to investigate the spatial dependence of the ZPTF with a detector system that maps the core, such as the SAFFRON array developed with a recent thesis for such purpose [110]. There is also the option to install PISTIL in other positions of the reactor, which makes the localized reactivity modulation asymmetric with respect to the core configuration and the detectors. This would allow to compare the measurements and check for possible discrepancies between the cases.

Chapter 6

Conclusion and perspectives

6.1 Summary of the Ph.D work

The knowledge of the kinetic parameters of nuclear reactors is of paramount importance for reactor operation. In this Ph.D work, we investigated the methodology to estimate the kinetic parameters through ZPTF measurements by modulating the reactivity of a reactor core. A new experimental device called PISTIL was designed, manufactured and tested in the CROCUS reactor within the framework of a collaboration between CEA and EPFL.

The design study of PISTIL is achieved with the combination of deterministic and stochastic simulations using the APOLLO3 and TRIPOLI-4 codes. This approach allows to converge rapidly towards a technical solution including materials and dimensions of the device.

PISTIL is able to generate a reactivity modulation through rotation. This allows the device to be placed within compact fuel lattices of nuclear reactors. The modulation is induced by a variable Cd(n, γ) reaction rate during the rotation. The measured modulation amplitude of PISTIL is 4.415 $\pm$ 0.003 pcm using JEFF-3.3 library, and 3.920 $\pm$ 0.003 pcm using ENDF/B-VII.1. These values confirm the accuracy of the estimation using Monte Carlo simulations.

Experimentally, the modulation is realized in two different manners with two types of motion commands of PISTIL to measure the ZPTF from 1.6 mHz to 200 Hz in a efficient manner: a rotation at constant angular speed, and a step-wise motion following successively predefined positions. The measurements are complementary as they serve as low and high frequency ZPTF measurements, respectively. The Bartlett's method is used for the computation of the PSDs for signals acquired in 42 experiments. The obtained spectra are analyzed at the fundamental frequency of the continuous experiments and the first 50 harmonics of the step-wise experiments. The uncertainty estimation is based on the standard deviation of the PSD calculated at each window. The uncertainty of the step-wise measurements could be underestimated as a result of a limited number of windows in the analysis. Nevertheless, the step-wise approach is shown to be particularly powerful and attractive for low frequency measurements. A more sophisticated design of the step-wise motion would allow to further improve the effectiveness of the approach.

The determination of the ZPTF phase requires an *a posteriori* correction due to an unexpected desynchronization of the acquisition system in sampling rate. Its impact in step-wise experiments is low, and the data after correction agrees with the theoretical prediction. For continuous experiments, despite the correction, phase values were considered invalid due to the lack of consistency between measurements. The RMSEs of the phase values of step-wise experiments, compared respectively to JEFF-3.3 and ENDF/B-VII.1 are 2.577 $\pm$ 0.053 and 4.894 $\pm$ 0.055. These values are much higher than the RMSEs of

the amplitude , which suggest that the uncertainty of the phase could be underestimated, again as a result of a limited number of windows in the analysis.

In the experimental design, it was desired that a maximum number of harmonics could be analyzed for the continuous rotation experiments. However, due to the low SNR of the harmonics, only the measurements at the fundamental frequency of the modulation were analyzed. For step-wise experiments, the first 50 harmonics with a reasonably high SNR were taken into account, as expected with a PRBS sequence of 5 bits. The overlaid harmonic frequencies in the two types of experiments showed amplitude results with excellent consistency.

The RMSE of the measured ZPTF amplitude as compared to calculated values using JEFF-3.3 and ENDF/B-VII.1 are respectively 1.042 ± 0.038 and 1.395 ± 0.010 for the step-wise measurements, which indicates that JEFF-3.3 would predict the kinetics of the delayed neutron precursors more accurately. For the continuous experiment, the RMSEs are 6.163 ± 0.118 (JEFF-3.3) and 1.077 ± 0.258 (ENDF/B-VII.1). Therefore, it is probable that ENDF/B-VII.1 based calculation is in better agreement for the computation of the prompt neutron generation time or its decay constant. The compatibility of prompt neutron and delayed neutron data of these two libraries are also confirmed by the calculation of the effective delayed generation time, the total delayed neutron fraction and the mean half-life of precursors. With ZPTF measurements, the JEFF-3.3 formulation is more consistent to study the relative abundances of delayed neutron groups while ENDF/B-VII.1 gives a better agreement with simulation-based estimation of total delayed neutron fraction.

6.2 Perspectives

For the determination of the amplitude of the ZPTF, the temporal variation of the reactivity should be known. However, the reactivity cannot be measured directly. It is estimated through the measurement of the angular position of PISTIL, and the corresponding reactivity worth was calculated using calibrations. It was observed that the reconstructed reactivity signals from the position presented a large number of harmonics that were not in the signals of the neutron detectors. The discrepancy between the number of harmonics in the modulation and the reactivity signal implies potential shortcomings of the approach, such as insufficient precision of the reactivity worth or resolution with respect to the precision. Additionally, step-wise experiments were observed to produce more consistent results as compared to the continuous experiments, probably due to the fact that the analysis was much less dependent on the calibration. For future experimental campaigns, complementary calibration studies could improve the reconstruction of the reactivity signal. Multiple factors could contribute to the improvement of inverse kinetics calibrations, such as longer duration, complementary measurements at multiple frequencies or different time resolution in acquisition.

The developed methodology in the design of the modulator and analyses of the experimental data could be complemented by new experiments. It was observed that the statistical dispersion of the amplitude results at frequencies higher than 120 Hz was higher than 20% . Measurements having a duration longer than 30 minutes would help to increase the SNR and improve the quality of the measurement. For the experiments, it

is also recommended to conduct sensitivity studies on the SNR concerning the shape of the modulation, the position of PISTIL and its distance from the detectors. For future experimental campaigns, a modified SNR criterion could be considered as the metrics to determine the measurement time to overcome the issue.

The step-wise mode is currently tested with an n-sequence generator for the pseudo-random signals. The possibility to use other pseudo-random generators could also be investigated to obtain a reduced number of harmonics with reasonable SNR. This would provide the possibility to resolve the harmonic peaks of the PSD with a reasonable window size and duration of the experiments.

The Bartlett's method used in the presented work allowed the variance reduction of the PSD estimation. The drawback was that the uncertainty of the measurement was estimated empirically, and the resolution requirement at low frequency modulation led to an insufficient statistical sample size for the uncertainty quantification. An alternative approach for the uncertainty estimation is to apply a bootstrap method to the PSD estimation. A methodology of bootstrap analysis for modulation experiments was developed and tested in the European project CORTEX [95]. By randomly resampling the signals with replacement, it allows to obtain a statistical distribution of the PSD estimates. The bootstrap also preserves the resolution that is equal to that of the calculated periodogram, i.e. the full length signal, which is of high interest for the low frequencies.

PISTIL was designed with a focus on the ZPTF measurements within the PK approximation. Nevertheless, PISTIL also has the potential to be used to study spatial effects related to reactor kinetics. No clear indication of spatial effects were observed with the large CFUL01 fission chambers operated in current mode in the water reflector of the CROCUS core, contrary to COLIBRI experiments in CROCUS, which can be explained by the relative symmetry of the experimental setup. There are also other positions where PISTIL can be installed, for instance control rod positions of CROCUS. This variation in the experimental configuration allows studying potential spatial effects related to localized modulation. Alternatively, neutron detector instrumentation at various in-core positions could also be investigated.

With a reprogramming of PISTIL's NC (eventually a replacement of the NC by a real-time system), the synchronization between acquisition systems would be ensured so that phase measurement could be extended to frequencies higher than 1 Hz. Measurement of the ZPTF phase in this range is particularly interesting for spatial kinetic studies and comparison with simulations.

Another experimental outlook is to conduct experiments in other ZPRs, as each research reactor presents different features. We may cite for instance the VENUS -F reactor in Belgium with a fast neutron spectrum. Modification of the active components of PISTIL is probably required to generate reactivity modulation of the same order of magnitude as in the current work.

Bibliography

[1] U. Kasemeyer, R. Früh, J. M. Paratte, *et al.*, *Benchmark on Kinetic Parameters in the CROCUS Reactor: International Reactor Physics Experiments Handbook (IRPhE) 4440*. 2007, p. 94.

[2] E. Fermi, "The Development of the First Chain Reacting Pile," in *Symposium on Atomic Energy and Its Implications*, American Philosophical Society, 1946, pp. 20–24.

[3] R. Robert, R. Meyer, L. Hafstad, *et al.*, "The delayed neutron emission which accompanies fission of uranium and thorium," *Physical Review*, vol. 55, no. 664,

[4] M. C. Brady, "Evaluation and application of delayed neutron precursor data," Ph.D. dissertation, Los Alamos National Laboratory, 1989.

[5] S. Brewer, "The first reactor," U.S. department of energy, Tech. Rep., 1982.

[6] Office of Nuclear Energy, *The history of nuclear energy*. Washinton D.C., 1984, pp. 1–19.

[7] D. L. Hetrick, *Dynamics of nuclear reactors*. The University of Chicago Press, 1971, p. 542.

[8] J. M. Harrer, R. E. Boyar, and D. Krucoff, "Transfer function of Argonne CP2 reactor," *Nucleonics*, 1952.

[9] J. A. DeShong, "Power Transfer Functions of the EBWR Obtained Using Sinusodidal Reactivity Driving Function," Argonne National Laboratory, Tech. Rep., 1958.

[10] M. B. Chadwick, M. Herman, P. Oblozinsky, *et al.*, "ENDF/B-VII.1 nuclear data for science and technology: Cross sections, covariances, fission product yields and decay data," *Nuclear Data Sheets*, vol. 112, no. 12, pp. 2887–2996, 2011.

[11] O. Cabellos, F. Alvarez-Velarde, M. Angelone, *et al.*, "Benchmarking and validation activities within JEFF project," *EPJ Web of Conferences*, vol. 146, pp. 4–9, 2017.

[12] K. Shibata, O. Iwamoto, T. Nakagawa, *et al.*, "JENDL-4.0: A new library for nuclear science and engineering," *Journal of Nuclear Science and Technology*, vol. 48, no. 1, pp. 1–30, 2011.

[13] D. G. Cacuci, *Handbook of nuclear engineering*. Springer, 2010. arXiv: `arXiv:1011.1669v3`.

[14] G. R. Keepin, T. F. Wimett, and R. K. Zeigler, "Delayed neutrons from fissionable isotopes of uranium, plutonium, and thorium," *Physical Review*, vol. 107, no. 4, pp. 1044–1049, 1957.

[15] G. D. Spriggs and J. M. Campbell, "A summary of measured delayed neutron group parameters," *Progress in Nuclear Energy*, vol. 41, no. 1, pp. 145–201, 2002.

[16] B. L. Sjenitzer and J. E. Hoogenboom, "A Monte Carlo Method for Calculation of the Dynamic Behaviour of Nuclear Reactors," *Progress in Nuclear Science and Technology*, vol. 2, no. 0, pp. 716–721, 2011.

[17] D Schneider, F Dolci, F Gabriel, *et al.*, "APOLLO3®: CEA/DEN deterministic multi-purpose code for reactor physics analysis," in *Proceedings of PHYSOR 2016*, Idaho, 2016.

[18] A. Gammichia, "Neutron kinetics equations for APOLLO3 code and application to noise problems," Ph.D. dissertation, Polytechnic University of Turin, 2018.

[19] C. J. Werner, J. S. Bull, C. J. Solomon, *et al.*, "MCNP6.2 Release Notes," *Report LA-UR-18-20808*, pp. 1–39, 2018.

[20] M. Aufiero, M. Brovchenko, A. Cammi, *et al.*, "Calculating the effective delayed neutron fraction in the Molten Salt Fast Reactor: Analytical, deterministic and Monte Carlo approaches," *Annals of Nuclear Energy*, vol. 65, pp. 78–90, 2014.

[21] E. Brun, F. Damian, C. M. Diop, *et al.*, "TRIPOLI-4®, CEA, EDF and AREVA reference Monte Carlo code," *Annals of Nuclear Energy*, vol. 82, pp. 151–160, 2015.

[22] A. Zoia, C. Jouanne, P. Siréta, *et al.*, "Analysis of dynamic reactivity by Monte Carlo methods: The impact of nuclear data," *Annals of Nuclear Energy*, vol. 110, pp. 11–24, 2017.

[23] G. Valocchi, P. Archier, and J. Tommasi, "Beta effective sensitivity to nuclear data within the APOLLO3® neutronic platform," *International Conference on Physics of Reactors: Transition to a Scalable Nuclear Future, PHYSOR 2020*, vol. 2020-March, pp. 2475–2482, 2020.

[24] D. Foligno, "New evaluation of delayed-neutron data and associated covariances," Ph.D. dissertation, Aix-Marseille University, 2019.

[25] O Pakari, V Lamirand, G Perret, *et al.*, "Current Mode Neutron Noise Measurements in the Zero Power Reactor CROCUS," *EPJ Web Conf.*, vol. 170, pp. 4–8, 2018.

[26] P. Dimitriou, I. Dillmann, B. Singh, *et al.*, "Development of a Reference Database for Beta-Delayed Neutron Emission," *Nuclear Data Sheets*, vol. 173, pp. 144–238, 2021.

[27] A. dos Santos, R. Diniz, R. Jerez, *et al.*, "The application of the multiple transient technique for the experimental determination of the relative abundances and decay constants of delayed neutrons of the IPEN/MB-01 reactor," *Annals of Nuclear Energy*, vol. 33, no. 10, pp. 917–923, 2006.

[28] B. Geslot, C. Jammes, and B. Gall, "Influence of the delayed neutron group parameters on reactivity estimation by rod drop analysis," *Annals of Nuclear Energy*, vol. 34, no. 8, pp. 652–660, 2007.

[29] G. Perret, "Amélioration et développement des méthodes de détermination de la réactivité - Maîtrise des incertitudes associées," Ph.D. dissertation, Université Joseph Fourier de Grenoble, 2003.

[30] M. Williams, *Random Processes in Nuclear Reactors*. Pergamon, 1974, p. 243.

[31] O. V. Pakari, "Experimental and numerical study of stochastic branching noise in nuclear reactors," Ph.D. dissertation, Ecole Polytechnique Fédérale de Lausanne, 2020, p. 205.

[32] J. A. DeShong, "Conference on Transfer Function Measurements and Reactor Stability Analysis," Argonne National Laboratory, Argonne, USA, Tech. Rep., 1960.

[33] D. Foligno and P. Leconte, "Uncertainty and covariances of the newly derived 8-groups delayed-neutrons abundances set," *EPJ Nuclear Sciences & Technologies*, vol. 4, p. 31, 2018.

[34] D. Foligno and P. Leconte, "Energy Dependence of Delayed-Neutron Data," *EPJ Web of Conferences*, vol. 211, pp. 1–7, 2019.

[35] D. Foligno, P. Leconte, O. Serot, *et al.*, " Measurement of the delayed-neutron multiplicity and time constants in the thermal neutron induced fission of U235 at ILL," *EPJ Web of Conferences*, vol. 239, 2020.

[36] B. Geslot, A. Sardet, P. Casoli, *et al.*, " Measuring the delayed neutrons multiplicity and kinetic parameters for the thermal induced fission of 235 U, 239 Pu and 233 U," in *Proceedings of ANIMMA 2021*, Prague, Czech Republic, 2021.

[37] E. Gilad, O. Rivin, H. Ettedgui, *et al.*, "Experimental estimation of the delayed neutron fraction β eff of the MAESTRO core in the MINERVE zero power reactor," *Journal of Nuclear Science and Technology*, vol. 52, no. 7-8, pp. 1026–1033, 2015.

[38] O. Pakari, V. Lamirand, G. Perret, *et al.*, "Investigation of spatial effects on neutron noise measurements in the zero power reactor CROCUS," in *Proceedings of PHYSOR 2018*, 2018, p. 12.

[39] V. Lamirand, G. De Izarra, A. Krása, *et al.*, "Intercomparison of neutron noise measurement systems in the CROCUS reactor," in *Proceedings of PHYSOR2018*, Caucun, Mexico, 2018, pp. 3709–3719.

[40] K. Ambrožič, V. P. Lamirand, S. Hübner, *et al.*, "Analysis of the first colibri fuel rods oscillation campaign in the crocus reactor for the european projectcortex," vol. 1, Cambridge, UK, 2020, pp. 1–8.

[41] G. D. Spriggs, J. M. Campbell, and V. M. Piksaikin, "An 8-group delayed neutron model based on a consistent set of half-lives," *Progress in Nuclear Energy*, vol. 41, no. 1-4 SPEC ISS, pp. 223–251, 2002.

[42] K. O. Ott and R. J. Neuhold, *Introductory nuclear reactor dynamics*. American Nuclear Society, 1985.

[43] J. Dorning, "Nuclear Reactor Kinetics: 1934–1999 and Beyond," in *Nuclear computational science: A century in review*, March 2015, Y. Azmy and E. Sartori, Eds., 2010, ch. 8, pp. 375–458.

[44] J. P. Franz, "Pile transfer functions," United States Atomic Energy Commission, Tech. Rep., 1949.

[45] H. B. Smets, "The Describing Function of Nuclear Reactors," *IRE Transactions on Nuclear Science*, vol. 6, no. 4, pp. 8–12, 1959.

[46] A. A. Wasserman, "Contributions to two problems in space-independent, nuclear reactor dynamics," Ph.D. dissertation, Massachusetts Institute of Technology, 1962.

[47] D. V. Widder, *Laplace transform*. Princeton university press, 2015.

[48] C. Cohn, "Determination of reactor zero power kinetics parameters by flux noise analysis," in *Conference on transfer function measurements and reactor stability analysis*, Argonne, USA, 1960.

[49] J. Wright and I. Pázsit, "Neutron kinetics in subcritical cores with application to the source modulation method," *Annals of Nuclear Energy*, vol. 33, no. 2, pp. 149–158, 2006.

[50] L. G. Kemeny, "Fundamental aspects of stochastic processes and fluctuation phenomena in fission reactors," in *Neutron noise,waves,and pulse propagation*, 1967.

[51] I. Pázsit, "On the kinetic response of a reactor with delayed neutrons," *Annals of Nuclear Energy*, vol. 23, no. 4-5, pp. 407–412, 1996.

[52] J. M. Harrer and J. G. Beckerley, *Nuclear Power Reactor Instrumentation Systems Handbook*. Office of Information Services, 1973, p. 318.

[53] A. Jebb, "Kinetic Studies on the University of London Nuclear Reactor," Ph.D. dissertation, Imperial College of Science and Technology, 1973.

[54] T. Sanda, M. Makido, H. Otani, *et al.*, "Transfer Function Measurements in JOYO by Pile Oscillator Method," *Journal of Nuclear Science and Technology*, vol. 20, no. 3, pp. 199–212, 1983.

[55] W. C. Lipinski, "EBWR stability analysis," in *Conference on transfer function measurements and reactor stability analysis*, 1960.

[56] M. Hara, H. Usui, Y. Fujii, *et al.*, "Application of the Pseudo Random Binary Signals to JRR-3 High Power Dynamics Measurements," *Journal of Nuclear Science and Technology*, vol. 5, no. 2, pp. 79–85, 1968.

[57] M. Buckner, "Optimum binary signals for frequency response testing," Ph.D. dissertation, University of Tennessee, 1970.

[58] B. E. Prince, S. J. Ball, J. R. Engel, *et al.*, "Zero-power physics experiments on the Molten-salt reactor experiment," U.S. Atomic Energy Commission, Tech. Rep., 1968.

[59] H. Hinds, F. McDonnell, and D. Walker, "Kinetics experiments on coupled cores in the ZED-2 reactor," Atomic Energy of Canada Limited, Ontario, Canada, Tech. Rep., 1972.

[60] W. Rhodes and H. Larson, "Frequency response testing at experimental breeder reactor II using discrete-level periodic signals," in *International fast reactor safety meeting*, American Nuclear Society, 1990, p. 93.

[61] A. Klickman, R. Horne, and H. Wilber, "Oscillator tests in the Enrico Fermi reactor," Atomic power development associates, INC., Tech. Rep., 1967.

[62] A. Baker, "Oscillator tests in British fast reactors," in *Conference on transfer function measurements and reactor stability analysis*, 1960.

[63] C. Griffin and J. J. Lundholm, "Measurement of the SRE and KEWB prompt neutron lifetime using random noise and reactor oscillation techniques," North American Aviation, Tech. Rep., 1959.

[64] G. Keeping and W. Stratton, "Instrumentation for pulsed neutron work at los alamos," in *Proceedings of the second symposium on the application of pulsed neutron source techniques*, Berkeley, California, 1958.

[65] V. Raievski, "Etude du transport des neutrons par la méthode de modulation," Ph.D. dissertation, Université de Paris, 1959.

[66] E. Cohen and R. Cordy, "Measurement and analysis of the KEWB transfer function by reactor modulation techniques," in *Conference on transfer function measurements and reactor stability analysis*, 1960.

[67] Y. Lee, "Measurement of the zero power transfer function of the Kansas state university TRIGA MARK II nuclear reactor," Ph.D. dissertation, Kansas state university, 1964.

[68] M. Petrovic, V. Markovic, D. Obradovic, *et al.*, "Pile oscillator ROB-1," Boris Kidric Institute of nuclear sciences, Tech. Rep., 1965.

[69] E. Walker, "A Neutron Oscillator to Study Reactor Kinetics Phenomena in the O.S.U. Nuclear Reactor," M.S. thesis, The Ohio State University, 1967.

[70] C. L. Cowan, "Measurement of the Livermore pool-type reactor (LPTR) transfer function using reactor oscillation techniques," University of California, Berkeley, Tech. Rep., 1965, pp. 1–5.

[71] P. T. Hansson and L. R. Foulke, "Investigations in Spatial Reactor Kinetics," *Nuclear Science and Engineering*, vol. 17, no. 4, pp. 528–533, 1963.

[72] R. J. Johnson, "Investigation of the space-dependent zero-power reactor source transfer function," Ph.D. dissertation, Georgia Institute of Technology, 1966.

[73] G. Saji, "Excitation of higher space modes in reactor transfer function measurement (Part 1)," *Nuclear Science and Engineering*, vol. 32, pp. 93–100, 1968.

[74] D. N. Bridges, "An investigation of the spatially dependent reactor source transfer function with temperature feedback," Ph.D. dissertation, Georgia Instituts of Technology, 1970.

[75] P. Reuss, *Précis de neutronique*. EDP Sciences, 2003.

[76] S. Michálek, S. Tevo, G. Farkas, *et al.*, "Determination of the effective delayed neutron fraction for training reactor VR-1," *Progress in Nuclear Energy*, vol. 52, no. 8, pp. 735–742, 2010.

[77] L. Li, M. Zeller, J. Chow, *et al.*, "Dynamic Parameter Fitting of the Zed-2 Reactor Core Using a Neutron Flux Perturbation Experiment," *CNL Nuclear Review*, pp. 1–10, 2016.

[78] Y. Yedvab, I. Reiss, M. Bettan, *et al.*, "Determination of delayed neutrons source in the frequency domain based on in-pile oscillation measurements," in *Proceeding of PHYSOR-2006*, Vancouver,Canada, 2006, pp. 1–9.

[79] P. Leconte, P. Archier, C. De Saint Jean, *et al.*, "New delayed neutron group constants and covariances for LWR core applications, combining summation calculations and integral experiments," *Annals of Nuclear Energy*, vol. 139, 2020.

[80] S Hübner, C Lange, W Lippmann, *et al.*, "Generation of high precise data for the verification of computational tools for reactor signal analysis," in *KompOst doctoral seminars Zittau*, 2018.

[81] Lamirand, Vincent, Frajtag, Pavel, Godat, Daniel, *et al.*, "The colibri experimental program in the crocus reactor: Characterization of the fuel rods oscillator," *EPJ Web Conf.*, vol. 225, 2020.

[82] D. Babala, "Measurement of Δ h in a water moderated reactor by an oscillating moderator-level technique," in *The Symposium on exponential and critical experiments*, 1964.

[83] C. Demazière and O. Glöckler, "On-line determination of the prompt fraction of in-core neutron detectors in CANDU reactors," in *Proceedings of PHYSOR 2004*, Chicage, IL USA, 2004.

[84] S. Zivi and R. Wright, "Power-void transfer function measurements in a simulated SPERT IA moderator coolant channel," in *Conference on transfer function measurements and reactor stability analysis*, 1960.

[85] V. V. Orlov and Y. Kazachenkov, "The influence of a magnetic field on neutron diffusion, and the possibility of magnetic control of reactors," *Soviet atomic energy*, vol. 33, p. 155, 1972.

[86] V. Romanov, "Effects of reactivity in nuclear reactor control by a magnetic field acting on a ferromagnet," *Atomnaya Energiya*, vol. 68, no. 4, 1990.

[87] W. L. Whittemore, "A continuously pulsed TRIGA reactor: an intense source for neutron scattering experiment," in *IGORR-IV: Proceedings of the fourth meeting of the International Group On Research Reactors*, Gatlinburg TN, USA, 1996, pp. 140–156.

[88] J. G. Lundholm, E. R. Meise, and C. W Griffin, "Measurement of zero power frequency response of the SRE," Atomics International, Tech. Rep., 1960.

[89] A. Zoia, Y. Nauchi, E. Brun, *et al.*, "Monte Carlo analysis of the CROCUS benchmark on kinetics parameters calculation," *Annals of Nuclear Energy*, vol. 96, pp. 377–388, 2016.

[90] O. Pakari, V. Lamirand, G. Perret, *et al.*, "Kinetic Parameter Measurements in the CROCUS Reactor Using Current Mode Instrumentation," *IEEE transactions on nuclear science*, vol. 65, no. 9, pp. 2456–2460, 2018.

[91] S. Hübner, A. Knospe, M. Viebach, *et al.*, "Experimental determination of the zero power transfer function of the AKR-2," in *International Conference on Physics of Reactors: Transition to a Scalable Nuclear Future, PHYSOR 2020*, 2020, pp. 2955–2962.

[92] M. Faucher, D. Mancusi, and A. Zoia, "New kinetic simulation capabilities for TRIPOLI-4®: Methods and applications," *Annals of Nuclear Energy*, vol. 120, no. 2018, pp. 74–88, 2018.

[93] G. Valocchi, "Neutronic modeling of complex cores in multidimentional kinetics: Application to the low void worth core ASTRID and to the preparation of a validation experiment," Ph.D. dissertation, Aix-Marseile Université, 2020.

[94] P. Archier, J.-M. Palau, J.-F. Vidal, *et al.*, "Validation of the Newly Implemented 3D TDT-MOC Solver of APOLLO3 Code on a Whole 3D SFR Heterogeneous Assembly," in *Proceedings of PHYSOR 2016*, Sun Valley, USA, 2016.

[95] K. Ambrožič, V. P. Lamirand, S. Hübner, *et al.*, "Noise analysis techniques of in-core modulation experiments of the European CORTEX project," vol. 2, 2020, pp. 1–8.

[96] Trio Motion Technology, *Motion coordinator 4xx range - software reference manual*, English, version 7, 2014.

[97] G. Truchet, P. Leconte, A. Santamarina, *et al.*, "Computing adjoint-weighted kinetics parameters in Tripoli-4 by the Iterated Fission Probability method," 2020.

[98] L. Petzoldl, "Automatic selection of methods for solving stiff and nonstiff systems of ordinary differential equations," *SIAM Journal on Scientific and Statistical Computing*, vol. 4, no. 1, pp. 136–148, 1983.

[99] B. Diven, H. Martin, R. Taschek, *et al.*, "Multiplicities of fission neutrons," *Physical Review*, vol. 101, no. 3, 1956.

[100] G. Perret, B. Geslot, A. Gruel, *et al.*, "Kinetic Parameter Measurements in the MINERVE Reactor," *IEEE Transactions on Nuclear Science*, vol. 64, no. 1, pp. 724–734, 2017.

[101] J. W. Cooley and J. W. Tukey, "An Algorithm for the Machine Calculation of Complex Fourier Series," *Mathematics of Computation*, vol. 19, no. 90, p. 297, 1965.

[102] F. J. Harris, "On the use of windows for harmonic analysis with the discrete fourier transform," *Proceedings of the IEEE*, vol. 66, no. 1, pp. 51–83, 1978.

[103] P. Brémaud, *Mathematical Principles of Signal Processing*. Springer, 2001.

[104] Y. Zhang, A. B. Baggeroer, and J. G. Bellingham, "The total variance of a periodogram-based spectral estimate of a stochastic process with spectral uncertainty and its application to classifier design," *IEEE Transactions on Signal Processing*, vol. 53, no. 12, pp. 4556–4567, 2005.

[105] P. D. Welch, "The Use of Fast Fourier Transform for the Estimation of Power Spectra," *IEEE Transactions on audio and electroacoustics*, no. 2, pp. 70–73, 1976.

[106] D. D. Rife and J. Vanderkooy, "Transfer-function measurement with maximum-length sequences," *Journal of the audio engineering society*, vol. 37, no. 6, pp. 419–444, 1989.

[107] K. O. Ott and R. J. Neuhold, "Introductory nuclear reactor dynamics," in American Nuclear Society, 1985, ch. 9.

[108] P. Virtanen, R. Gommers, T. E. Oliphant, *et al.*, "SciPy 1.0: Fundamental Algorithms for Scientific Computing in Python," *Nature Methods*, vol. 17, pp. 261–272, 2020.

[109] C. Demazière and G. Andhill, "Identification and localization of absorbers of variable strength in nuclear reactors," *Annals of Nuclear Energy*, vol. 32, no. 8, pp. 812–842, 2005.

[110] F. Vitullo, V. Lamirand, K. Ambrožič, *et al.*, "Design of a 150-miniature detectors 3D core-mapping system for the CROCUS reactor," in *Proceedings of ANIMMA 2021*, Prague, Czech Republic, 2021.

Appendix A

In-core Tests of PISTIL

A.1 Motion tests

Although the motion configured by the user on the PC software described in section 3.3.4.1 is well produced by PISTIL, the identification of the actual modulation frequency was systematically conducted by signal analysis. In the experimental campaign, constant speed rotations were performed at various speed and each of these motion profiles was measured during at least 30 minutes. The acquisitions were performed at 1 kHz. Figure A.1 shows a typical motion signal, which was acquired between 0° and 360°.

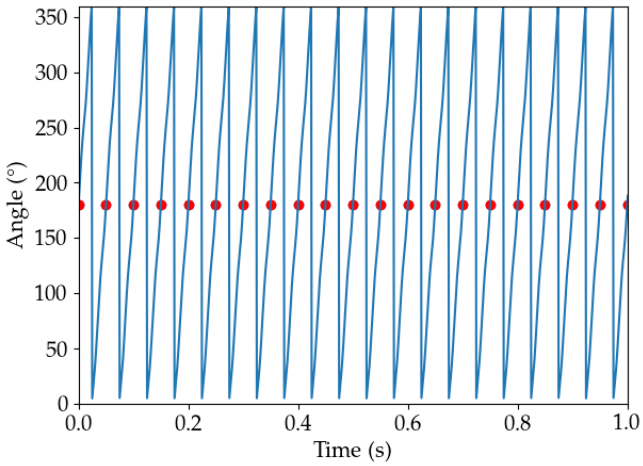

Figure A.1: Position measurement of a PISTIL rotation configured at 7200 °.s^{-1} (20 Hz rotation)

The frequency of the motion was estimated by using the positive-crossing rate, which was the average rate of the signal to change from a position below a certain value to a position above it, with a tolerance of 0.1°. As the angular position of PISTIL wraps 360°, the 180°was chosen as the crossing angle to avoid the misdetection, as the unit cycle index shown in figure A.1.

Table A.1 presents the estimated motion frequency and associated uncertainty. The motion control showed in general a regular behavior, but discrepancy in the cycle length were observed to be high for 40 and 60 Hz. This might be attributed to the gain setting of the proportional–integral–derivative control that were tuned to be less precise in this region. This resulted in the modulation frequency to differ from the command value in continuous rotation experiment, an estimation of the moduation frequency were thus

conducted using the motion signal.

Table A.1: Constant speed rotation tests and the obtained mean rotation frequency and associated uncertainty

Command (°/s)	Main frequency (Hz)	Uncertainty (Hz)
180	0.500	0.001
360	1.000	0.001
720	2.000	0.001
1440	4.000	0.001
2880	8.000	0.009
5760	16.000	0.013
7200	20.000	0.023
14400	40.000	1.13
21600	59.99	1.79
28800	79.99	0.08
36000	100.00	0.04

Figure A.2 is the APSD of the motion signal acquired for a $360°.s^{-1}$ rotation. As the motion signal has a triangular shape, the peak power of the harmonics decrease following $1/n^2$ where n is the harmonic order.

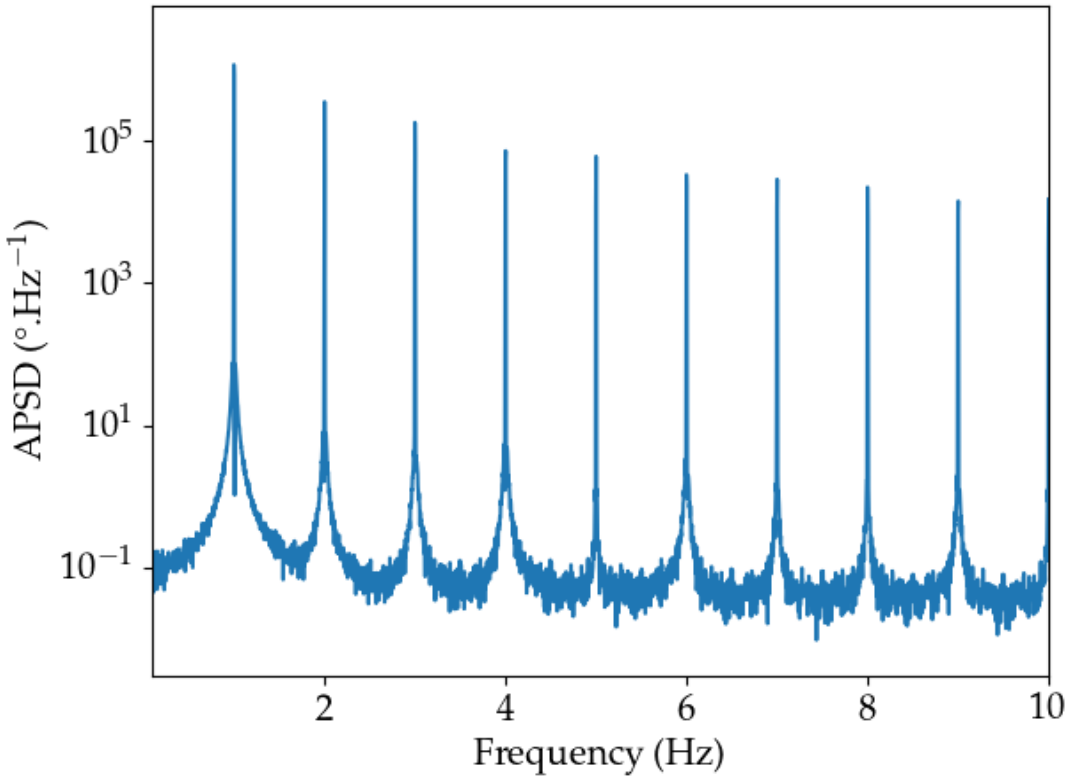

Figure A.2: APSD of the motion signal of a $360°.s^{-1}$ rotation measured during 50 minutes at 1 kHz

A.2 Background noise measurement

Strong acoustic noise was observed during some first in-pile tests. It appeared near the motor for rotation frequencies above 15 Hz, which could be caused to the mechanical vibration of PISTIL.

A series of background noise measurement were conducted. The aim was to verify the absence of neutronic effect caused by mechanical vibration. The rotor and stator cadmium element were respectively centered at 750 and 760 mm. In this configuration, the modulation effect is considered negligible as the rotor and stator are completely uncovered. Rotations were performed at 1, 20 and 100 Hz, and the signals of the four CFUL01 detectors were acquired during 30 minutes. Appendix A.2 shows the APSD and CPSD of neutron detector signals. The calculated APSDs and CPSDs of the signals confirmed that there is no identifiable harmonics of the frequency of the mechanical rotation. Therefore, it was considered there is no vibration induced neutronic perturbation. The peak located at 50 Hz was a known issue of the HV power supplies. The APSDs present a noise in the same order of magnitude of other modulation experiments.8

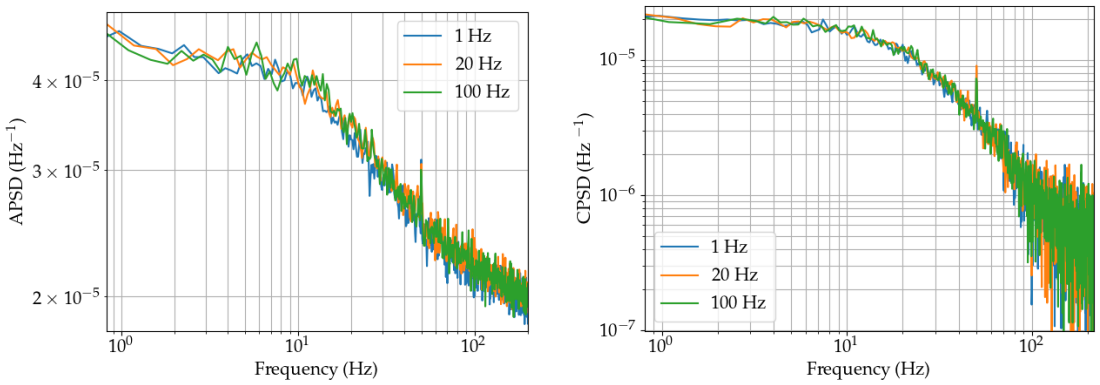

Figure A.3: Measured PSD of detector 1 (left) and CPSD between detectors 1 and 2 (right) in the background noise measurement during 30 minutes at 1 kHz sampling rate, the frequency resolution is 5.6 mHz

Appendix B

Computed Effective Kinetic Parameters of CROCUS

The effective kinetic parameters of CROCUS were computed using TRIPOLI-4.11 with JEFF-3.3 and ENDF/B-VII.1libraries. The computed values are adjoint-weighted kinetic parameters estimated by the Iterated Fission Probability (IFP) method [97].

Table B.1: Computed adjoint-weighted kinetic parameters of CROCUS using JEFF-3.3 library

Generation time $\Lambda = 47.703 \pm 0.001$ μs		
Group	Decay constant (s^{-1})	Abundance (pcm)
1	0.012 47	22.87 ± 0.24
2	0.028 29	109.92 ± 0.53
3	0.042 52	64.99 ± 0.41
4	0.133 04	142.22 ± 0.60
5	0.292 47	246.89 ± 0.80
6	0.666 49	80.52 ± 0.46
7	1.634 78	66.26 ± 0.41
8	3.554 60	25.00 ± 0.25
	Sum	758.67 ± 1.40

Table B.2: Computed adjoint-weighted kinetic parameters of CROCUS using ENDF-B.VII.1 library

Generation time $\Lambda = 47.502 \pm 0.001$ μs		
Group	Decay constant (s^{-1})	Abundance (pcm)
1	0.013 38	23.78 ± 0.18
2	0.032 52	126.50 ± 0.50
3	0.121 18	123.64 ± 0.45
4	0.306 03	284.42 ± 0.60
5	0.858 26	126.41 ± 0.43
6	2.883 37	52.47 ± 0.39
	Sum	737.23 ± 1.09

Appendix C

List of Modulation Experiments

The summary of the accomplished experiments in 2021 May and June are summarized in table C.1. The experiments are listed in chronological order of the acquisition performed on each day. The item indicated in red consists in an experiment discarded in the analysis due to an important core water level modification by the operator, which caused the drift in the detector signals too important to be corrected. The items in orange are measurements at frequencies impacted by the abnormal electronic noise in the detector signal. Some of the first harmonics in these measurements were not affected and considered valid.

Table C.1: Summary of experiments conducted during the first experimental campaign of PISTIL in CROCUS

Date	Type	fundamental period of the modulation (s)	Duration (min)
2021-05-31	Continuous	1/0.5 1 1/2 1/4 1/8 1/16 1/32	30
2021-06-01	Continuous	1	30
	Step-wise	1/61 1/122	60
2021-06-02	Continuous	1	30
	Step-wise	1/610	120
	Continuous	1/0.5 1/2 1/4 1/8 1/16	30
2021-06-07	Step-wise	1/61 1/122	60
		1/610	120
2021-06-09	Continuous	1/0.5 1 1/2 1/4 1/8 1/16 1/32	30
2021-06-10	Continuous	1/40 1/80 1/120 1/160 1/200	30
2021-06-14	Step-wise	1/61 1/122	60
		1/610	120
2021-06-15	Continuous	1/40 1/80 1/120 1/160 1/200 1/32	30

Appendix D

Reactivity Calibration Results with Inverse Point Kinetics Analysis

In this section are given the calibrated function of reactivity with respect to the angular position. The function was obtained using a non-linear least square fit of the function:

$$\rho(\gamma(t)) = C_0 + \sum_{i=1}^{n}[A_i \sin(\frac{2\pi}{360} i\gamma(t)) + B_i \cos(\frac{2\pi}{360} i\gamma(t))] \tag{D.1}$$

where $\gamma(t)$ is the angular position in degree, A_i, B_i and C_0 are the fitted coefficients.

D.1 JEFF-3.3 based results

Table D.1: Fit coefficients of the reactivity calibration using JEFF-3.3 based kinetic parameters

A_1	A_2	A_3	A_4	A_5	B_1	B_2	B_3	B_4	B_5	C_0
8.3E-07	4.0E-05	1.1E-07	-3.5E-06	2.6E-07	7.0E-07	-1.5E-05	4.4E-07	-4.0E-06	-1.5E-07	1.9E-06

Table D.2: Covariance matrix of the fit coefficients of the reactivity calibration using JEFF-3.3 based kinetic parameters

A_1	A_2	A_3	A_4	A_5	B_1	B_2	B_3	B_4	B_5	C_0
1.8E-11	-3.7E-14	8.6E-14	-1.8E-14	6.0E-14	-8.3E-14	-4.1E-14	7.0E-14	1.3E-13	4.1E-14	-2.8E-14
-3.7E-14	1.9E-11	-5.6E-14	1.5E-13	-3.4E-15	-9.7E-14	-1.2E-14	9.2E-14	1.1E-13	7.7E-14	-8.3E-14
8.6E-14	-5.6E-14	1.9E-11	-4.1E-14	3.7E-14	-9.5E-14	3.7E-14	2.8E-14	3.5E-14	5.3E-14	-6.9E-14
-1.8E-14	1.5E-13	-4.1E-14	1.9E-11	-1.0E-13	-4.7E-15	-5.4E-14	-2.0E-14	-3.0E-14	5.4E-14	-1.2E-14
6.0E-14	-3.4E-15	3.7E-14	-1.0E-13	1.9E-11	1.5E-14	-6.2E-14	-1.1E-13	-1.7E-15	4.7E-14	6.5E-14
-8.3E-14	-9.7E-14	-9.5E-14	-4.7E-15	1.5E-14	1.9E-11	-9.5E-15	1.3E-13	4.7E-14	-1.4E-14	-2.4E-14
-4.1E-14	-1.2E-14	3.7E-14	-5.4E-14	-6.2E-14	-9.5E-15	1.9E-11	1.0E-14	7.2E-14	3.2E-14	1.1E-13
7.0E-14	9.2E-14	2.8E-14	-2.0E-14	-1.1E-13	1.3E-13	1.0E-14	1.9E-11	-6.1E-15	1.8E-13	1.4E-14
1.3E-13	1.1E-13	3.5E-14	-3.0E-14	-1.7E-15	4.7E-14	7.2E-14	-6.1E-15	1.9E-11	5.8E-14	2.3E-14
4.1E-14	7.7E-14	5.3E-14	5.4E-14	4.7E-14	-1.4E-14	3.2E-14	1.8E-13	5.8E-14	1.9E-11	3.3E-14
-2.8E-14	-8.3E-14	-6.9E-14	-1.2E-14	6.5E-14	-2.4E-14	1.1E-13	1.4E-14	2.3E-14	3.3E-14	9.3E-12

D.2 ENDF/B-VII.1 based results

Table D.3: Fit coefficients of the reactivity calibration using ENDF/B-VII.1 based kinetic parameters

A_1	A_2	A_3	A_4	A_5	B_1	B_2	B_3	B_4	B_5	C_0
2.1E-07	3.5E-05	-2.7E-07	-3.1E-06	1.1E-07	1.5E-07	-1.1E-05	2.3E-07	-3.9E-06	-1.2E-07	1.3E-06

Table D.4: Covariance matrix of the fit coefficients of the reactivity calibration using ENDF/B-VII.1 based kinetic parameters

A_1	A_2	A_3	A_4	A_5	B_1	B_2	B_3	B_4	B_5	C_0
8.4E-11	-2.6E-14	4.9E-13	-1.8E-13	1.3E-13	-4.6E-13	-1.6E-13	4.5E-13	3.1E-13	4.1E-14	4.8E-14
-2.6E-14	8.4E-11	-2.1E-13	6.2E-13	-7.4E-14	-6.6E-14	-6.0E-15	1.5E-13	4.9E-13	2.3E-13	-4.6E-13
4.9E-13	-2.1E-13	8.4E-11	-1.0E-13	4.3E-13	-4.7E-13	2.5E-13	3.4E-14	6.5E-14	5.8E-13	-1.1E-13
-1.8E-13	6.2E-13	-1.0E-13	8.4E-11	-3.2E-15	8.0E-14	-4.3E-13	1.5E-13	1.2E-13	9.0E-14	-9.1E-15
1.3E-13	-7.4E-14	4.3E-13	-3.2E-15	8.4E-11	2.2E-14	-8.6E-15	-3.4E-13	2.0E-13	2.0E-13	2.0E-13
-4.6E-13	-6.6E-14	-4.7E-13	8.0E-14	2.2E-14	8.5E-11	-7.7E-14	4.8E-13	1.4E-13	-1.3E-13	-5.4E-14
-1.6E-13	-6.0E-15	2.5E-13	-4.3E-13	-8.6E-15	-7.7E-14	8.4E-11	1.1E-13	3.5E-13	2.7E-14	4.8E-13
4.5E-13	1.5E-13	3.4E-14	1.5E-13	-3.4E-13	4.8E-13	1.1E-13	8.4E-11	-1.4E-15	5.3E-13	-2.6E-14
3.1E-13	4.9E-13	6.5E-14	1.2E-13	2.0E-13	1.4E-13	3.5E-13	-1.4E-15	8.4E-11	-9.4E-14	4.3E-16
4.1E-14	2.3E-13	5.8E-13	9.0E-14	2.0E-13	-1.3E-13	2.7E-14	5.3E-13	-9.4E-14	8.4E-11	1.6E-13
4.8E-14	-4.6E-13	-1.1E-13	-9.1E-15	2.0E-13	-5.4E-14	4.8E-13	-2.6E-14	4.3E-16	1.6E-13	4.2E-11

Appendix E

Measured ZPTF Amplitude and Phase

The measured amplitude and phase values are shown in this section. The values are separated into different tables for the 3 step-wise experiments of different unit step duration. The amplitude values are given with the normalization of reactivity amplitude using calculations based on kinetic parameters estimated using JEFF-3.3 and ENDF/B-VII.1 libraries.

Table E.1: Measured ZPTF amplitude for continuous rotation experiments using ENDF/B-VII.1 based calibration

Frequency (Hz)	Amplitude	Uncertainty
0.5	145.14	1.42
1	139.35	1.29
2	136.06	1.49
4	133.81	1.28
8	126.81	1.25
16	111.50	1.29
32	80.95	1.15
40	69.01	0.91
80	39.09	1.98
120	24.60	2.65
160	13.31	1.86
200	11.10	1.74

Table E.2: Measured ZPTF amplitude for step-wise experiments of 2 s unit step using ENDF/B-VII.1 based calibration

Frequency (Hz)	Amplitude	Uncertainty
0.0164	320.27	9.37
0.0492	213.59	3.46
0.0820	185.07	18.87
0.1148	162.20	15.78
0.2295	145.24	19.64
0.2623	150.94	11.45
0.3115	152.04	21.64
0.3443	152.17	7.27
0.3607	150.49	4.96
0.3770	150.81	3.40
0.4590	141.90	10.22
0.4918	145.32	5.50
0.5082	147.37	5.54
0.5246	148.41	7.38
0.5410	141.78	11.77
0.5902	141.54	6.97
0.6393	143.40	9.75
0.6557	141.08	11.41
0.6885	140.79	5.97
0.7049	137.61	17.87
0.7541	130.87	16.95

Table E.3: Measured ZPTF amplitude for step-wise experiments of 10 s unit step using ENDF/B-VII.1 based calibration

Frequency (Hz)	Amplitude	Uncertainty
0.0016	1280.67	58.76
0.0049	593.35	1.14
0.0082	449.76	2.54
0.0115	387.50	5.39
0.0148	369.07	28.17
0.0164	316.67	30.48
0.0180	314.11	1.43
0.0197	307.97	6.09
0.0213	293.71	0.70
0.0230	301.44	26.16
0.0246	280.68	2.58
0.0262	262.05	10.76
0.0311	251.16	0.78
0.0328	242.27	9.98
0.0344	240.44	2.86
0.0361	237.57	2.09
0.0377	237.44	2.03
0.0393	234.51	13.70
0.0410	226.93	4.11
0.0426	222.52	1.90
0.0443	225.43	2.07
0.0459	215.78	7.57
0.0475	226.66	4.07
0.0492	210.50	2.67
0.0508	213.48	4.61
0.0525	215.28	9.87
0.0541	220.22	9.93
0.0557	202.60	5.00
0.0574	205.43	11.38
0.0590	207.80	12.23
0.0607	201.92	28.93
0.0623	199.70	6.16
0.0639	197.74	11.70
0.0656	202.58	6.39
0.0672	201.40	28.41
0.0689	197.11	3.17
0.0705	195.70	22.68
0.0754	179.49	16.14

Table E.4: Measured ZPTF amplitude for step-wise experiments of 2 s unit step using ENDF/B-VII.1 based calibration

Frequency (Hz)	Amplitude	Uncertainty
0.0082	447.44	7.67
0.0164	301.10	58.02
0.0246	278.52	2.06
0.0410	230.51	3.61
0.0574	203.55	8.72
0.0738	187.18	32.26
0.0820	189.39	14.52
0.0902	183.48	22.93
0.0984	180.68	9.10
0.1066	172.71	5.17
0.1148	181.20	19.33
0.1230	173.97	13.52
0.1311	167.61	9.31
0.1557	163.29	18.25
0.1639	163.85	13.79
0.1721	165.15	5.08
0.1803	164.50	4.37
0.1885	164.75	3.60
0.1967	158.41	14.19
0.2049	155.32	5.92
0.2131	158.29	5.18
0.2213	162.32	6.20
0.2295	151.59	10.54
0.2459	156.51	7.87
0.2623	153.62	9.53
0.2705	148.81	17.36
0.2787	151.46	8.06
0.2869	155.60	15.62
0.2951	157.42	20.87
0.3197	152.77	25.42
0.3443	146.99	9.89
0.3689	129.29	24.81
0.3770	149.84	13.25

Table E.5: Measured ZPTF amplitude for continuous rotation experiments using JEFF-3.3 based calibration

Frequency (Hz)	Amplitude	Uncertainty
0.5	130.62	1.27
1	125.42	1.16
2	122.45	1.34
4	120.43	1.16
8	114.13	1.13
16	100.35	1.16
32	72.85	1.04
40	62.11	0.82
80	35.18	1.78
120	22.14	2.38
160	11.98	1.67
200	9.99	1.57

Table E.6: Measured ZPTF amplitude for step-wise experiments of 1 s unit step using JEFF-3.3 based calibration

Frequency (Hz)	Amplitude	Uncertainty
0.0164	285.95	8.37
0.0492	190.71	3.09
0.0820	165.24	16.85
0.1148	144.82	14.09
0.2295	129.68	17.53
0.2623	134.77	10.22
0.3115	135.75	19.32
0.3443	135.87	6.49
0.3607	134.37	4.43
0.3770	134.65	3.03
0.4590	126.70	9.12
0.4918	129.75	4.91
0.5082	131.58	4.94
0.5246	132.51	6.59
0.5410	126.59	10.51
0.5902	126.38	6.22
0.6393	128.03	8.71
0.6557	125.97	10.19
0.6885	125.70	5.33
0.7049	122.87	15.96
0.7541	116.85	15.13

Table E.7: Measured ZPTF amplitude for step-wise experiments of 2 s unit step using JEFF-3.3 based calibration

Frequency (Hz)	Amplitude	Uncertainty
0.0082	399.50	6.85
0.0164	268.84	51.80
0.0246	248.67	1.84
0.0410	205.81	3.22
0.0574	181.74	7.79
0.0738	167.12	28.81
0.0820	169.10	12.97
0.0902	163.82	20.48
0.0984	161.33	8.12
0.1066	154.20	4.61
0.1148	161.79	17.26
0.1230	155.33	12.07
0.1311	149.65	8.31
0.1557	145.79	16.29
0.1639	146.29	12.31
0.1721	147.46	4.53
0.1803	146.87	3.90
0.1885	147.10	3.21
0.1967	141.44	12.67
0.2049	138.68	5.29
0.2131	141.33	4.63
0.2213	144.93	5.54
0.2295	135.35	9.41
0.2459	139.74	7.03
0.2623	137.16	8.51
0.2705	132.87	15.50
0.2787	135.23	7.20
0.2869	138.93	13.95
0.2951	140.55	18.63
0.3197	136.40	22.69
0.3443	131.24	8.83
0.3689	115.43	22.15
0.3770	133.79	11.83

Table E.8: Measured ZPTF amplitude for step-wise experiments of 10 s unit step using JEFF-3.3 based calibration

Frequency (Hz)	Amplitude	Uncertainty
0.0016	1143.45	52.46
0.0049	529.78	1.02
0.0082	401.57	2.27
0.0115	345.98	4.81
0.0148	329.52	25.15
0.0164	282.74	27.22
0.0180	280.45	1.28
0.0197	274.97	5.44
0.0213	262.24	0.63
0.0230	269.14	23.36
0.0246	250.61	2.30
0.0262	233.97	9.61
0.0311	224.25	0.70
0.0328	216.31	8.91
0.0344	214.68	2.55
0.0361	212.12	1.87
0.0377	212.00	1.81
0.0393	209.39	12.24
0.0410	202.61	3.67
0.0426	198.68	1.70
0.0443	201.28	1.85
0.0459	192.66	6.76
0.0475	202.38	3.63
0.0492	187.94	2.38
0.0508	190.60	4.12
0.0525	192.21	8.81
0.0541	196.62	8.87
0.0557	180.90	4.47
0.0574	183.42	10.16
0.0590	185.54	10.92
0.0607	180.29	25.83
0.0623	178.30	5.50
0.0639	176.56	10.44
0.0656	180.88	5.71
0.0672	179.82	25.36
0.0689	176.00	2.83
0.0705	174.74	20.25
0.0754	160.26	14.41

Table E.9: Measured ZPTF phase for step-wise experiments of 1 s step duration

Frequency (Hz)	Phase (rad)	Uncertainty (rad)
0.0164	−0.534	0.090
0.0328	−0.506	0.007
0.0492	−0.327	0.087
0.0656	−0.404	0.024
0.0820	−0.337	0.141
0.0984	−0.335	0.057
0.1148	−0.332	0.114
0.1311	−0.232	0.079
0.1475	−0.006	0.076
0.1639	−0.336	0.052
0.1803	−0.273	0.097
0.1967	−0.300	0.033
0.2131	−0.187	0.113
0.2295	−0.273	0.062
0.2459	−0.047	0.097
0.2623	−0.039	0.126
0.2787	−0.239	0.078
0.3115	−0.139	0.103
0.3279	−0.202	0.061
0.3443	−0.369	0.049
0.3607	−0.179	0.085
0.3770	−0.367	0.102
0.3934	−0.133	0.086
0.4098	−0.258	0.105
0.4262	−0.221	0.081
0.4426	−0.158	0.091
0.4590	−0.353	0.066
0.4754	−0.298	0.055
0.4918	−0.208	0.121
0.5082	−0.133	0.074
0.5246	−0.109	0.103
0.5410	−0.058	0.108
0.5574	−0.102	0.107
0.5738	−0.092	0.105
0.5902	−0.142	0.124
0.6066	−0.134	0.115
0.6230	−0.168	0.104
0.6393	−0.166	0.113
0.6557	−0.236	0.109
0.6721	−0.172	0.098
0.6885	−0.185	0.122
0.7049	0.123	0.167
0.7213	−0.293	0.104
0.7377	−0.355	0.129
0.7541	−0.079	0.160

Table E.10: Measured ZPTF phase for step-wise experiments of 2 s step duration

Frequency (Hz)	Phase (rad)	Uncertainty (rad)
0.0082	−0.679	0.028
0.0164	−0.633	0.005
0.0246	−0.506	0.063
0.0328	−0.549	0.005
0.0410	−0.560	0.086
0.0492	−0.478	0.009
0.0574	−0.480	0.079
0.0656	−0.374	0.064
0.0738	−0.419	0.047
0.0820	−0.412	0.030
0.0902	−0.366	0.040
0.0984	−0.374	0.010
0.1066	−0.293	0.048
0.1148	−0.358	0.025
0.1230	−0.342	0.030
0.1311	−0.076	0.128
0.1393	−0.368	0.038
0.1557	−0.243	0.070
0.1639	−0.343	0.032
0.1721	−0.325	0.025
0.1803	−0.301	0.036
0.1885	−0.140	0.074
0.1967	−0.320	0.035
0.2049	−0.272	0.061
0.2131	−0.243	0.043
0.2213	−0.205	0.066
0.2295	−0.300	0.068
0.2377	−0.269	0.051
0.2459	−0.312	0.030
0.2541	−0.277	0.059
0.2623	−0.271	0.092
0.2705	−0.262	0.073
0.2787	−0.258	0.085
0.2869	−0.200	0.073
0.2951	−0.178	0.106
0.3033	−0.321	0.071
0.3115	−0.201	0.077
0.3197	−0.239	0.062
0.3279	−0.238	0.096
0.3361	−0.256	0.052
0.3443	−0.092	0.096
0.3525	0.209	0.178
0.3607	−0.156	0.099
0.3689	−0.243	0.078
0.3770	−0.090	0.136

Table E.11: Measured ZPTF phase for step-wise experiments of 10 s step duration

Frequency (Hz)	Phase (rad)	Uncertainty (rad)
0.0016	−1.000	0.008
0.0033	−0.950	0.029
0.0049	−0.844	0.015
0.0066	−0.832	0.006
0.0082	−0.744	0.024
0.0098	−0.751	0.008
0.0115	−0.784	0.000
0.0131	−0.727	−0.003
0.0148	−0.772	−0.003
0.0164	−0.665	0.021
0.0180	−0.695	0.054
0.0197	−0.657	0.015
0.0213	−0.713	0.037
0.0230	−0.631	0.004
0.0246	−0.658	0.011
0.0262	−0.505	0.044
0.0279	−0.612	0.020
0.0311	−0.567	0.009
0.0328	−0.557	0.018
0.0344	−0.576	0.027
0.0361	−0.536	0.003
0.0377	−0.542	0.016
0.0393	−0.527	0.001
0.0410	−0.536	0.056
0.0426	−0.506	0.012
0.0443	−0.482	0.029
0.0459	−0.536	0.068
0.0475	−0.506	0.002
0.0492	−0.489	0.050
0.0508	−0.494	0.020
0.0525	−0.428	0.031
0.0541	−0.478	0.050
0.0557	−0.470	0.034
0.0574	−0.443	0.023
0.0590	−0.487	0.041
0.0607	−0.443	0.004
0.0623	−0.421	0.025
0.0639	−0.431	0.084
0.0656	−0.389	0.044
0.0672	−0.451	0.034
0.0689	−0.371	0.038
0.0705	−0.124	0.053
0.0721	−0.407	0.071
0.0738	−0.428	0.057
0.0754	−0.237	0.100

Table E.12: Sample peak power estimation of selected harmonics with limited uncertainty in a step-wise modulation of 1 s step duration

Date	Frequency (Hz)	Reactivity (JEFF-3.3) Energy (-)	Reactivity (JEFF-3.3) σ (-)	Neutron signal Power (-)	Neutron signal σ (-)
2021/06/01	0.0164	1.09×10^{-10}	3.32×10^{-14}	8.50×10^{-6}	3.69×10^{-7}
	0.0492	6.34×10^{-10}	3.48×10^{-13}	2.37×10^{-5}	3.98×10^{-7}
	0.0820	2.35×10^{-10}	2.22×10^{-13}	6.71×10^{-6}	1.82×10^{-7}
	0.1148	7.50×10^{-11}	1.05×10^{-13}	1.75×10^{-6}	9.93×10^{-8}
	0.1475	1.61×10^{-11}	2.94×10^{-14}	3.19×10^{-7}	4.86×10^{-8}
	0.1803	7.86×10^{-11}	1.76×10^{-13}	1.67×10^{-6}	8.87×10^{-8}
	0.2131	3.38×10^{-10}	8.39×10^{-13}	6.88×10^{-6}	1.86×10^{-7}
	0.2459	9.41×10^{-11}	2.89×10^{-13}	1.77×10^{-6}	7.34×10^{-8}
	0.3115	2.87×10^{-10}	1.05×10^{-12}	5.36×10^{-6}	1.49×10^{-7}
	0.3443	5.84×10^{-11}	2.65×10^{-13}	1.07×10^{-6}	9.23×10^{-8}
	0.3770	1.17×10^{-10}	5.44×10^{-13}	2.19×10^{-6}	8.73×10^{-8}
	0.4098	6.65×10^{-11}	3.44×10^{-13}	1.23×10^{-6}	5.92×10^{-8}
	0.4426	7.15×10^{-11}	3.96×10^{-13}	1.29×10^{-6}	6.49×10^{-8}
	0.4754	3.75×10^{-11}	2.32×10^{-13}	6.81×10^{-7}	5.22×10^{-8}
	0.5082	6.19×10^{-11}	3.86×10^{-13}	1.11×10^{-6}	8.37×10^{-8}
	0.6393	2.21×10^{-11}	1.88×10^{-13}	3.73×10^{-7}	5.20×10^{-8}

Table E.13: Sample peak power estimation of selected harmonics with limited uncertainty in a step-wise modulation of 10 s step duration

Date	Frequency (Hz)	Reactivity (JEFF-3.3) Power (-)	Reactivity (JEFF-3.3) σ (-)	Neutron signal Power (-)	Neutron signal σ (-)
2021/06/07	0.0016	1.09×10^{-10}	2.63×10^{-17}	1.37×10^{-4}	1.40×10^{-5}
	0.0049	6.35×10^{-10}	1.47×10^{-16}	1.79×10^{-4}	7.97×10^{-7}
	0.0082	2.36×10^{-10}	1.39×10^{-16}	3.77×10^{-5}	3.42×10^{-7}
	0.0115	7.49×10^{-11}	1.14×10^{-16}	9.08×10^{-6}	3.20×10^{-7}
	0.0148	1.63×10^{-11}	1.15×10^{-16}	1.72×10^{-6}	3.37×10^{-7}
	0.0180	7.85×10^{-11}	3.92×10^{-16}	6.14×10^{-6}	6.75×10^{-8}
	0.0213	3.38×10^{-10}	2.06×10^{-15}	2.34×10^{-5}	7.41×10^{-8}
	0.0246	9.44×10^{-11}	3.54×10^{-16}	6.12×10^{-6}	9.25×10^{-8}
	0.0311	2.88×10^{-10}	3.57×10^{-15}	1.46×10^{-5}	1.08×10^{-7}
	0.0344	5.80×10^{-11}	1.29×10^{-15}	2.63×10^{-6}	3.28×10^{-8}
	0.0377	1.18×10^{-10}	3.20×10^{-15}	5.32×10^{-6}	9.12×10^{-8}
	0.0410	6.60×10^{-11}	1.90×10^{-15}	2.564×10^{-6}	4.66×10^{-8}
	0.0443	7.12×10^{-11}	2.36×10^{-15}	2.84×10^{-6}	4.96×10^{-8}
	0.0475	3.78×10^{-11}	6.99×10^{-16}	1.49×10^{-6}	5.62×10^{-8}
	0.0508	6.17×10^{-11}	2.90×10^{-15}	2.24×10^{-6}	1.06×10^{-7}
	0.0541	1.67×10^{-11}	7.07×10^{-16}	6.76×10^{-7}	5.96×10^{-8}
	0.0574	3.16×10^{-11}	2.06×10^{-15}	1.01×10^{-6}	1.49×10^{-7}
	0.0607	1.14×10^{-11}	2.02×10^{-15}	3.85×10^{-7}	3.17×10^{-8}
	0.0639	2.19×10^{-11}	3.11×10^{-15}	7.33×10^{-7}	1.11×10^{-7}
	0.0672	4.40×10^{-12}	2.05×10^{-15}	1.41×10^{-7}	4.93×10^{-8}
	0.0705	9.00×10^{-12}	2.81×10^{-15}	2.64×10^{-7}	4.45×10^{-8}
	0.0738	2.99×10^{-12}	5.18×10^{-16}	6.84×10^{-8}	2.21×10^{-8}

Appendix F

Correlation between Experimental Data

In the experimental design it was considered that the independent measurements do not provide correlated experimental data, as well as the data of one single experimental run with multiple harmonics. The absence of correlation between measurements were verified for continuous modulation measurements. The correlation coefficient, is defined as:

$$r(f_j, f_k) = \frac{\sum_{i=1}^{n}((x_{ij} - x_j)(x_{ik} - x_k))}{\sigma_j \sigma_k} \tag{F.1}$$

where f is the frequency bin, x is either the APSDs or the phase angle of the CPSDs calculated with the i-th time window of the spectral calculation for the estimation of the average value. Figure F.1 shows the calculated correlation matrix of one measurement of a 20 Hz continuous modulation. No clear correlation was observed at the frequency of the harmonics, other than those corresponding to those ones included in the same peak bins. The alike analysis was complicated to be applied to the step-wise modulation

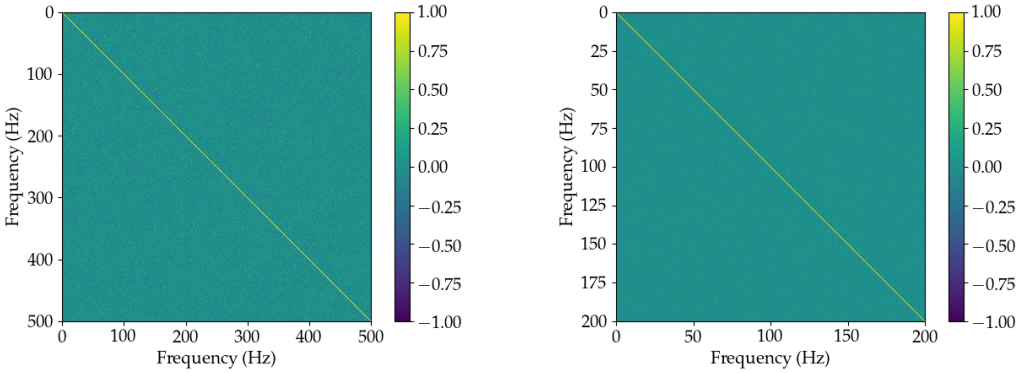

Figure F.1: Correlation matrix of APSD peak powers (left) and phase angle (right) measurements for a 20 Hz continuous modulation

measurements, due to the lack of sufficient number of time windows and consequently statistically significant results were not obtained to conclude through experimental data, as indicated in figure F.2. The justification that the measurements were not correlated is that the signal acquired in experiments can be decomposed by Fourier analysis as a sum of a number of uncorrelated sinusoidal modes. As in the continuous case no correlation was observed for the peaks, the same conclusion should apply to the decomposed step-wise signal.

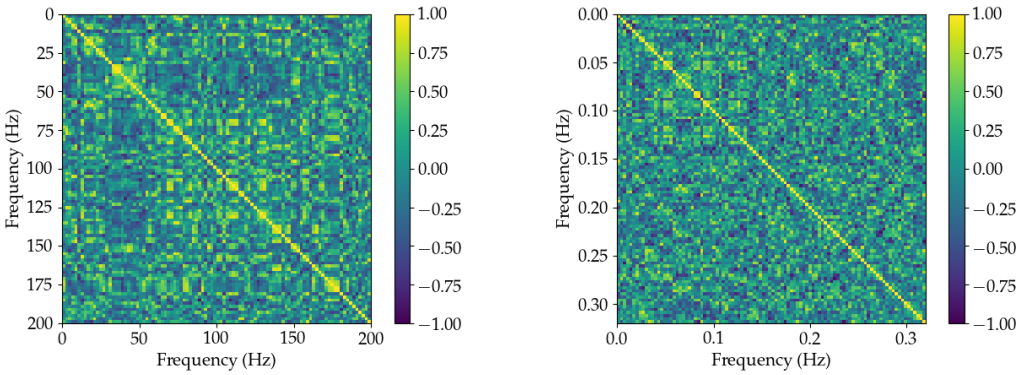

Figure F.2: Correlation matrix of APSD peak powers (left) and phase angle (right) measurements for a 61 s period step-wise modulation

Figure F.3 and figure F.4 presents the probability density distribution of the APSD and CPSD phase angle for the aforementioned signals, without taking into account the diagonal elements. Statistically, in the continuous case the correlation coefficients follow a Gaussian distribution with zero-mean and has no significant correlation between different frequencies.

For the step-wise case, due to the lack of the data available for statistical analysis, the standard deviation of the distributions were significantly higher. Nevertheless, there was little deviation from a Gaussian distribution. The calculation allowed therefore to make the hypothesis of the randomness of the correlation matrix and the possibility to propagate the uncertainty of the amplitude and phase individually, without giving a covariance matrix for each experiment.

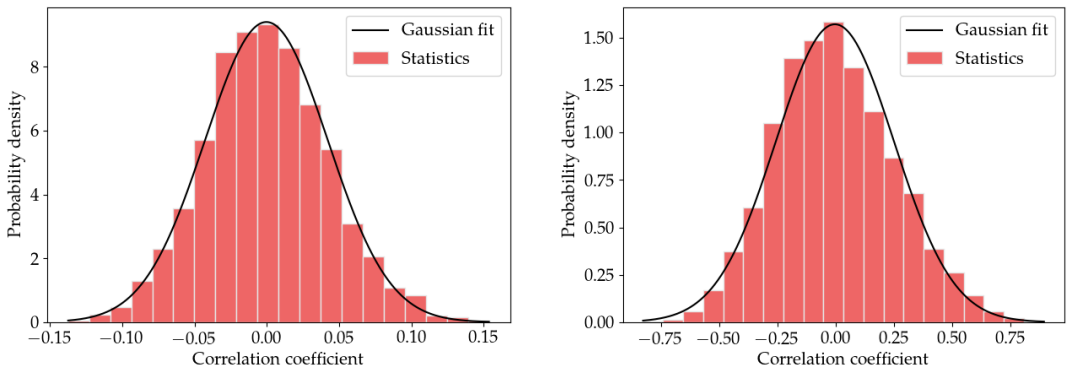

Figure F.3: Probability density distribution of the correlation matrix of APSD peak powers of 20 Hz modulation and 61 s period step-wise modulation

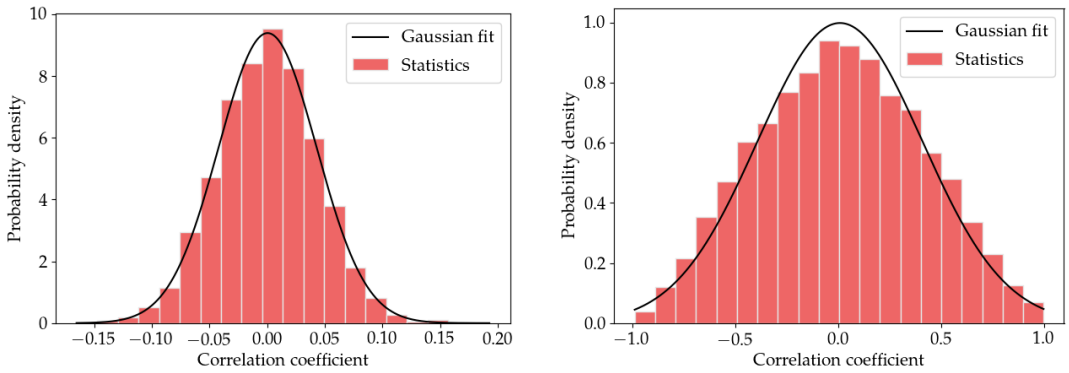

Figure F.4: Probability density distribution of the correlation matrix of CPSD phase angle powers of 20 Hz modulation and 61 s period step-wise modulation

Appendix G

Technical drawings of PISTIL's rotor and stator

Drawing 1: Rotor assembly Drawing 2: Stator assembly

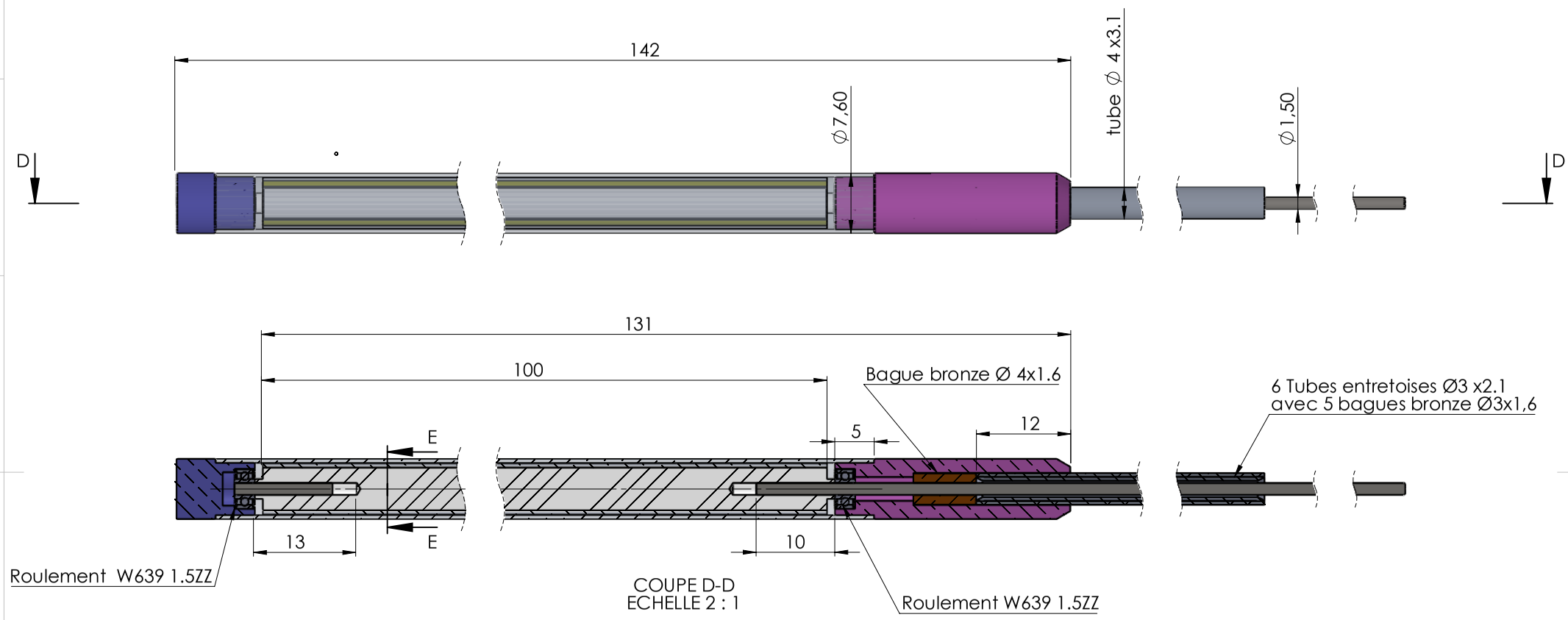

COUPE D-D
ECHELLE 2 : 1

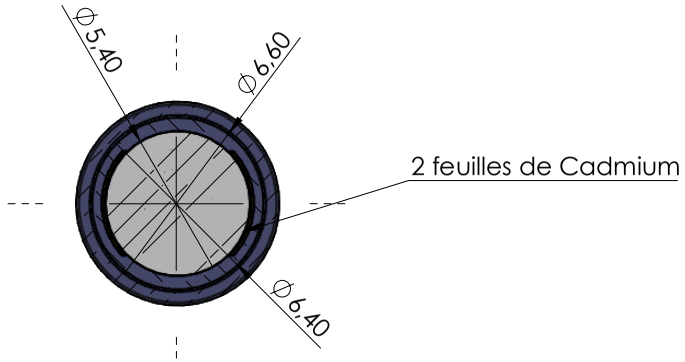

COUPE E-E
ECHELLE 5 : 1

Nota: Assemblage des éléments avec colle Acrylique PENLOC GTI

Ind.	Détail des modifications.	Dessiné par	DATE	Vérifié par	DATE
C	Version TQC	LECOMTE M	16/10/2020	HAZARD M	16/10/2020
B	Mise à jour BPE suite FAD DO 64 du 15/07/20	LECOMTE M.	16/07/2020	HAZARD.M	16/07/2020
A	Version initiale.	LECOMTE M.	26/06/2020	HAZARD.M	26/06/2020

Ft	Qté	Rep	REFERENCE	MASSE DE LA PIECE (g)	DIMENSIONS	MATIERE
A3	1	-	-	52.2	-	Alu 2017

TOLERANCE G.LE	ETAT DE SURFACE G.LE	PROTECTION	MARQUAGE
+/-0.2	3.2 SAUF INDICATION CONTRAIRE	-	-

TQC

REALISE PAR :

E.I.C

2 chemin de la Roquevinière
30330 St Laurent La Vernede
- Tél : 06.76.88.96.33

ENSEMBLE: **MODULATEUR DE REACTIVITE PISTIL**

SOUS ENSEMBLE: **Sous ensemble ROTOR**

ECHELLE	REF. FICHIER	REF. CLIENT	REFERENCE PLAN	INDICE	PLANCHE
3:1	ELC-153	CEA Cadarache	ELC- 153 DP 138	C	1/1

AUCUNE ARETE VIVE (CH 0.2 x 45°) SAUF CONTRE-INDICATION

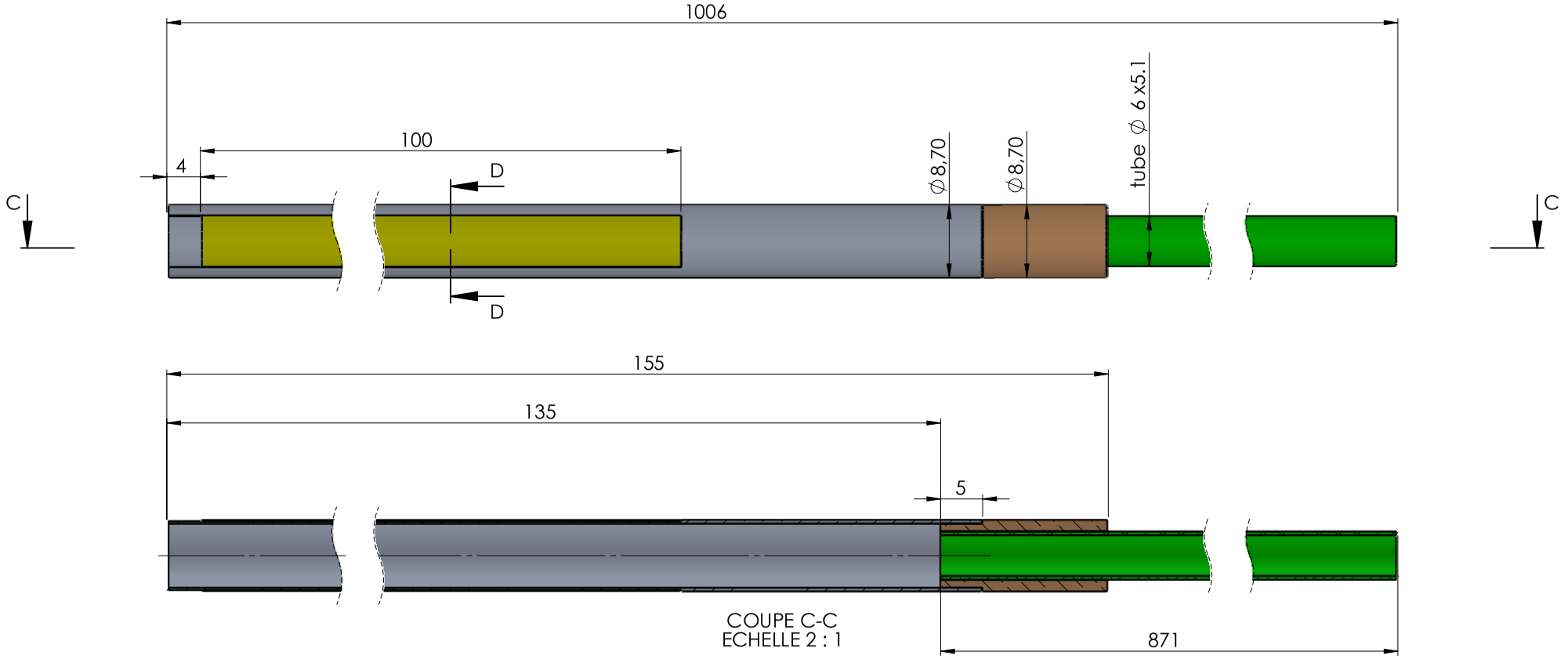

COUPE C-C
ECHELLE 2 : 1

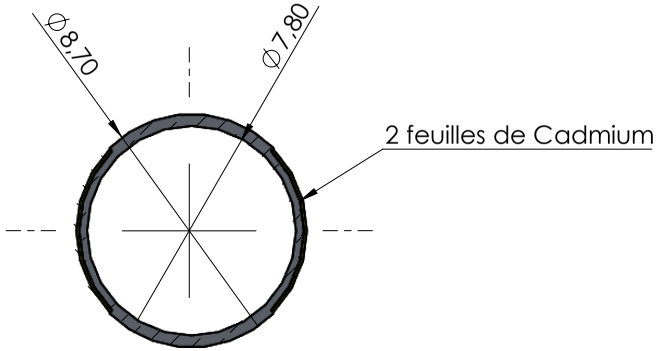

COUPE D-D
ECHELLE 5 : 1

Nota: Assemblage des éléments avec colle Acrylique PENLOC GTI

TQC

AUCUNE ARETE VIVE (CH 0.2 x 45°) SAUF CONTRE-INDICATION

Ind.	Détail des modifications.	Dessiné par	DATE	Vérifié par	DATE
C	Version TQC	LECOMTE M.	16/10/2020	HAZARD.M	16/10/2020
B	Mise à jour BPE suite FAD DO 64 du 15/07/20	LECOMTE M.	16/07/2020	HAZARD.M	16/07/2020
A	Version initiale.	LECOMTE M.	26/06/2020	HAZARD.M	26/06/2020

Ft	Qté	Rep	REFERENCE	MASSE DE LA PIECE (g)	DIMENSIONS	MATIERE
A3	1	-	-	-	-	-

TOLERANCE G.LE: +/-1
ETAT DE SURFACE G.LE: 3.2 SAUF INDICATION CONTRAIRE
PROTECTION: -
MARQUAGE: -

REALISE PAR :
E.I.C
2 chemin de la Roquevinière
30330 St Laurent La Vernede
- Tél : 06.76.88.96.33

ENSEMBLE: MODULATEUR DE REACTIVITE PISTIL
SOUS ENSEMBLE: SOUS ENSEMBLE STATOR

ECHELLE	REF. FICHIER	REF. CLIENT	REFERENCE PLAN	INDICE	PLANCHE
2:1	ELC-153	CEA Cadarache	ELC- 153 DP 139	C	1/1